Version – 1/Mar/2007

Rethinking the N(H_2)/I(CO) Conversion Factor

W. F. Wall

Instituto Nacional de Astrofísica, Óptica, y Electrónica, Apdo. Postal 51 y 216, Puebla, Pue., México

wwall@inaoep.mx

ABSTRACT

An improved formulation for the N(H_2)/I(CO) conversion factor or X-factor is proposed. The statement that the velocity-integrated radiation temperature of the ^{12}CO J = 1 → 0 line, $I(^{12}\mathrm{CO})$, "counts" optically thick clumps is quantified using the formalism of Martin et al. (1984) for line emission in a clumpy cloud. Adopting the simplifying assumptions of thermalized ^{12}CO J = 1 → 0 line emission and isothermal gas, an effective optical depth, τ_{ef}, is defined as the product of the clump filling factor within each velocity interval and the clump effective optical depth as a function of the optical depth on the clump's central sightline, τ_0. The clump effective optical depth is well approximated as a power law in τ_0 with power-law index, ϵ, referred to here as the clump "fluffiness," and has values between zero and unity. While the ^{12}CO J = 1 → 0 line is optically thick within each clump (i.e., high τ_0), it is optically thin "to the clumps" (i.e., low τ_{ef}). Thus the dependence of $I(CO)$ on τ_{ef} is linear, resulting in an X-factor that depends only on clump properties and *not* directly on the entire cloud. Assuming virialization of the clumps yields an expression for the X-factor whose dependence on physical parameters like density and temperature is "softened" by power-law indices of less than unity that depend on the fluffiness parameter, ϵ. The X-factor provides estimates of gas column density because each sightline within the beam has optically thin gas within certain narrow velocity ranges. Determining column density from the optically thin gas is straightforward and parameters like ϵ then allow extrapolation of the column density of the optically thin gas to that of all the gas. Implicit in this formulation is the assumption that fluffiness is, on average, constant from one beam to the next. This is also required to some extent for density and temperature, but the dependence of the X-factor, X_f, on these may be weaker.

One important suggestion of this formulation is that *virialization of entire clouds is* ir*relevant.* The densities required to give reasonable values of X_f are consistent with those found in cloud clumps (i.e. $\sim 10^3\, H_2\, \mathrm{cm}^{-3}$). Thus virialization of clumps, rather than of entire clouds, is consistent with the observed values of X_f. And even virialization of clumps is not strictly required; only a relationship between clump velocity width and column density similar to that of virialization can still yield reasonable values of the X-factor. The underlying physics is now at the scale of cloud clumps, implying that the X-factor can probe sub-cloud structure.

The proposed formulation makes specific predictions of the dependence of X_f on the CO abundance and of the interpretation of line ratios. In particular, the ^{13}CO J $= 1 \rightarrow 0/^{12}$CO J $= 1 \rightarrow 0$ line ratio values observed in the Orion clouds suggest that $\epsilon \simeq 0.3 \pm 0.1$. If the majority of the ^{12}CO J $= 1 \rightarrow 0$ emission originates in structures with an r^{-2} density variation, then the constraints on ϵ also constrain the ratio of the outer-to-inner radii of the r^{-2} region within the clumps. Specifically, this ratio for spherical clumps must be 2 to 9 and for cylindrical clumps it must be 4 to 42. This is apparently consistent with observations, but higher spatial resolution is necessary to ensure that the observed ratios are not just lower limits. This formulation also ties the narrow range of the observed values of the ^{13}CO J $= 1 \rightarrow 0/^{12}$CO J $= 1 \rightarrow 0$ line ratio to the relative constancy of the X-factor.

The properties of real clumps in real molecular clouds can be used to estimate the X-factor within these clouds and then be compared with the observationally determined X-factor. This yields X-factor values that are within a factor of 2 of the observed values. This is acceptable for the first attempt, but reducing this discrepancy will require improving the formulation. While this formulation improves upon that of Dickman et al. (1986), it has shortcomings of its own. These include uncertainties as to why ϵ seems to be constant from cloud to cloud, uncertainties in defining the average clump density and neglecting certain complications, such as non-LTE effects, magnetic fields, turbulence, etc.

Despite these shortcomings, the proposed formulation represents the first major improvement in understanding the X-factor because it is the first formulation to include radiative transfer.

Subject headings: ISM: molecules and dust — Orion

1. Introduction

One of the most basic questions that can be asked in any field of research is about the quantity of the material under investigation. In studies of the interstellar medium (ISM), for instance, the amount of gas and dust bears on questions of the physical mechanisms that effect and control the ISM and, consequently, how that ISM evolves and can affect the evolution of an entire galaxy. In particular, the amount of molecular gas in a cloud, cloud complex, spiral arm, or galaxy constrains the number of stars that form and the way that they form. The workhorse molecule for estimating molecular gas masses has been, and still is, CO (e.g., see IAU Symp. #170, 1997, and references therein). Specifically, observations of the J = 1 → 0 rotational line of the isotopologue, $^{12}C^{16}O$ (just CO for short), permit simple, but crude, estimates of the mass of molecular hydrogen in an astronomical source. The velocity-integrated radiation temperature, I(CO), often called the *integrated intensity*, is multiplied by a standard conversion factor, $N(H_2)/I(CO)$, to yield the molecular hydrogen column density, $N(H_2)$, which gives the H_2 mass of the source after integrating over the source's projected area. The most current value of this conversion factor is about $2 \times 10^{20}\, H_2\, cm^{-2} \cdot (K \cdot km \cdot s^{-1})^{-1}$ for the molecular gas in the disk of our Galaxy (Dame et al. 2001).

Why the CO J = 1 → 0 line should yield an estimate of column density is far from clear. Even if this line were optically thin, the conversion factor would depend in a simple way on the physical conditions in the molecular gas. Given that CO has many rotational levels and that the spacings of these levels (in temperature units) are comparable to the temperatures found in molecular gas, the $N(H_2)/I(CO)$ conversion factor would depend, at the very least, on the gas kinetic temperature. Given that the densities inferred with molecular clouds (of at least $\sim 10^3\, H_2\, cm^{-3}$) are comparable to, and not much higher than, the critical densities of the observed rotational transitions, then it is obvious that $N(H_2)/I(CO)$ should also have at least a weak dependence on molecular gas density. Another obvious dependence would be on the abundance of CO relative to H_2, X(CO). If these physical conditions were known, then the molecular hydrogen column density could be recovered easily (see Appendix A of Wall 2006). Even if these conditions are not known exactly, observations of molecular clouds on galactic scales would yield reasonable estimates of molecular gas column densities, because reasonable values for the relevant physical parameters are well known and are relatively constant from source to source. For example, estimating the mass of the molecular medium of an entire galaxy using an optically thin molecular line would be, on average, more reliable than estimating the mass of a molecular cloud core *of unknown physical conditions,* because the physical conditions in the molecular gas averaged over the scale of a galaxy are less extreme and vary much less from galaxy to galaxy than they do from cloud core to cloud core. In any event, the conversion from integrated intensity to column density is very straightforward

and relatively simple in the optically thin case. However, as is well known (e.g., see Evans 1980; Kutner 1984; Evans 1999), the CO J = 1 → 0 line is optically thick, obfuscating any simple explanation as to why it should probe molecular gas column densities.

Other tracers of molecular gas mass exist, tracers that do not possess the potentially serious uncertainties posed by CO J = 1 → 0. The rotational lines of the isotopologues $^{13}C^{16}O$ and $^{12}C^{18}O$ (just ^{13}CO and $C^{18}O$ in short form), for example, can be optically thin and, consequently, their integrated intensities have a straightforward relationship with the molecular gas column density (provided the physical conditions are known). While potentially simpler to use for determining column densities, these optically thin lines are normally factors of about 3 to 50 weaker than the CO J = 1 → 0 line (e.g., Kutner 1984; Langer & Penzias 1990; Nagahama et al. 1998; Maddalena et al. 1986); the ^{12}CO lines are better for mapping large areas of molecular gas or for detecting weak sources, such as high-redshift galaxies (e.g., Brown & Vanden Bout 1992; Barvainis et al. 1997, 1998; Alloin et al. 2000; Carilli et al. 2002,a). This makes the J = 1 → 0 line of CO, and the $N(H_2)/I(CO)$ factor, more useful or even essential in estimating the total molecular gas mass in some sources, resulting in a strong incentive for understanding the $N(H_2)/I(CO)$ factor's behavior.

The usual attempts at accounting for why the $N(H_2)/I(CO)$ factor, or X-factor (or X_f), is relatively constant on multi-parsec scales are variations of the explanation given by Dickman et al. (1986), hereafter DSS86 (e.g., Sakamoto 1996). A summary of the DSS86 explanation follows. If T_R is the peak radiation temperature of the CO J = 1 → 0 line and Δv is the appropriately defined velocity width of this line, then $I(CO) = T_R \Delta v$. If the molecular gas under observation is virialized, then the observed velocity width is related to the mass of this gas and, therefore, the gas column density averaged over the solid angle subtended by the observed gas. It was then easy to show that $N(H_2)/I(CO) \propto n^{0.5}/T_R$. The n was the gas density *averaged over the virialized volume of gas.* DSS86 found that n had to be $\sim few \times 10^2\, H_2\, cm^{-3}$ to give the observed value of $N(H_2)/I(CO)$; therefore it was assumed that this volume included entire clouds. Because the CO J = 1 → 0 line is optically thick, relatively easily thermalized (compared to higher rotational lines of CO), and may almost fill the radio telescope's beam at the line peak, it has been assumed that $T_R \simeq T_K$, where T_K is the gas kinetic temperature, T_K (e.g., Kutner & Leung 1985; Weiss et al. 2001). Even if the gas does not fill the beam (a point to which we will return later), we would have T_R roughly proportional to T_K and we would still have $N(H_2)/I(CO) \propto n^{0.5}/T_K$. The basic argument is that the quantity $n^{0.5}/T_K$ does not strongly vary on multi-parsec scales, especially due to the weak dependence on density, resulting in a fairly stable value of X. Observational evidence does indeed seem to support a roughly constant value of the X-factor to within a factor of about 2 for the disk of our Galaxy, where $X \simeq 2 \times 10^{20}\, cm^{-2} \cdot (K \cdot km \cdot s^{-1})^{-1}$ (see, e.g., Dame et al. 2001; Strong et al. 1988, and references therein), although

the observations of Sodroski et al. (1994) and Strong et al. (2004) suggest a higher value of X_f in the outer disk (a claim that is at odds with Carpenter et al. 1990). The values of the X-factor that apply to the disks of other spiral galaxies are often within factors of about 3 of that of the Galactic disk X-factor (e.g., Young & Scoville 1982; Adler et al. 1992; Guélin et al. 1995; Nakai & Kuno 1995; Brouillet et al. 1998; Rand et al. 1999; Meier et al. 2000, 2001; Boselli et al. 2002; Rosolowski et al. 2003).

Nonetheless, there is good observational evidence that the usual value of the X-factor does *not always* apply. In the centers of external galaxies, the X-factor is factors of about 5 or more lower than the standard value (e.g., Rickard & Blitz 1985; Israel 1988; Wall et al. 1993; Regan 2000; Paglione et al. 2001), as well as in the central region of our own Galaxy (Sodroski et al. 1995; Dahmen et al. 1997, 1998). In contrast, clouds in the central region of the galaxy M 31 have an X-factor that is an order of magnitude larger than that for the disk of our Galaxy (Sofue & Yoshida 1993; Loinard & Allen 1998). The high-latitude translucent clouds in our Galaxy show X-factor variations with a total range of an order of magnitude (see Magnani et al. 1998). In some infrared luminous galaxies there is evidence that the X-factor can be roughly an order of magnitude lower than the standard value (Yao et al. 2003). In irregular galaxies, the X-factor can be more than an order of magnitude higher than the standard value (e.g., Israel 1988; Dettmar & Heithausen 1989; Israel 1997,a; Madden et al. 1997; Fukui et al. 1999). A detailed discussion of the shortcomings of the X-factor can be found in Maloney & Black (1988)(also see Israel 1988; Kutner & Leung 1985).

Hence, any complete explanation or theory of the X-factor must allow for and account for inferred variations of X_f in some cases and, at the same time, relative stability of X_f in other cases. This is a difficult balancing act, but achieving such a theory is important for the very basic reason that scientific tools must be thoroughly understood. While there are a few articles that explore the underlying physics of X_f (e.g., DSS86 Maloney & Black 1988; Israel 1988; Kutner & Leung 1985), there are literally *hundreds* of articles in the literature that use or mention the X-factor without a *detailed* examination of its physical properties (including even Wall et al. 1996). This is in stark contrast to the situation with supernovae type Ia (SNe Ia), for example. SNe Ia can be used as standard candles (Phillips 1993; Reiss et al. 1995, 1996; Hamuy et al. 1996,a) and can constrain cosmological models (Reiss et al. 1998; Perlmutter et al. 1999). While these supernovae are often used as standard candles, there is also much theoretical and observational work to understand SNe Ia (e.g. Sauer et al. 2006; Wang 2007; Reiss & Livio 2006; Garg et al. 2007; James et al. 2006; Neill et al. 2006; Borkowski et al. 2006). Such work will elucidate why SNe Ia are standard candles, or why they might not be in some cases (see Howell et al. 2006). In a sense, the X-factor is *almost* a standard candle that relates surface brightness to surface density (i.e., $I(CO)$ to $N(H_2)$). And yet there is comparatively little effort to shed light on the physics underpinning the

X-factor.

Furthermore, there are a number of more specific reasons for understanding X_f:

Reliable molecular gas mass estimates. Among other things, this can refine our understanding of star formation yields (i.e., what fraction of the gas goes into star formation).

Improved knowledge of molecular cloud structure and physics. Better comprehension of the X-factor can constrain estimates of molecular cloud physical parameters and can supply new insights into star formation processes.

Improved radiative transfer theory. While it is unlikely that there would be fundamental improvements of radiative transfer theory, such improvements are still possible, benefiting astrophysical theory in general.

These represent possible long-term goals of research into the physics underlying the X-factor.

The goals of the current paper are considerably more modest: addressing the deficiencies of the DSS86 explanation of the X-factor, improving upon this explanation, and examining a few consequences of the formulation proposed here. Improvements are necessary because DSS86 has the following problems:

1. *No treatment of radiative transfer.* This is a fundamental problem with DSS86. At first glance, it might seem superfluous to treat radiative transfer in the optically thick case. However, if we consider a clumpy medium, where the clumps can have optically thin edges and optically thin frequencies in their line profiles, then treating radiative transfer is essential for understanding the X-factor. In particular, *the optically thin limit of CO $J = 1 \rightarrow 0$ must also be included.* Any *complete* treatment must include the optically thin case, whether this case is observed in nature or not. This case cannot be included easily in the DSS86 explanation because it includes the virial theorem with*out* including radiative transfer — virialization by itself says nothing about the optical depth of the emission.

2. *Sensitivity to T_K and n(H_2).* As discussed in Wall (2006), I(CO) and the X-factor estimate the molecular hydrogen column densities to within factors of about 2 of the values determined from optically thin tracers for the majority of positions in the Orion clouds. And yet we know from Wall (2006) (looking at two-component model temperatures), the range of gas kinetic temperatures can be an order of magnitude. In general, we know that molecular cloud kinetic temperatures and densities have a full range of an order of magnitude on multi-parsec scales (cf. Sanders et al. 1985; Sakamoto et al. 1994; Helfer & Blitzer 1997; Plume et al. 2000). Since the X-factor supposedly varies

as $n^{0.5}/\mathrm{T_K}$, the temperature and density variations can *each* change X_f by factors of 3 to 10 (unless $n^{0.5}$ were to vary like $\mathrm{T_K}$, but this is unlikely to be true in general, especially if there is pressure equilibrium). Thus the X_f of DSS86 is too sensitive to the density and kinetic temperature. Having a weaker dependence of X_f on n and $\mathrm{T_K}$, like X $\propto(n/\mathrm{T_K})^{0.3}$, would resolve this sensitivity problem; variations of an order of magnitude in either n or $\mathrm{T_K}$ would allow X to vary by less than a factor of 2.

3. *Virialization of entire clouds.* DSS86 require low densities (i.e. $\mathrm{n(H_2)} \sim few \times 10^2\,\mathrm{cm^{-3}}$) to obtain the observed value of the X-factor. Given that the critical density of the CO J = 1 → 0 transition is $\sim 3 \times 10^3\,H_2\,\mathrm{cm^{-3}}$, the densities of the CO-emitting structures are about an order of magnitude higher (also see the average densities of the filaments found by Nagahama et al. 1998). The low density required by DSS86 may represent the density averaged over an entire cloud. For the Orion A and B clouds, this volume-averaged density is between about 200 and $600\,H_2\,\mathrm{cm^{-3}}$, depending on the precise assumptions used. Therefore, DSS86 are assuming that entire clouds are stable and virialized. Some evidence suggests that larger molecular clouds are indeed virialized (i.e. for masses $\gtrsim 10^4\,\mathrm{M_\odot}$, e.g., see Heyer et al. 2001; Simon et al. 2001), while other evidence suggests that many molecular clouds may not be (Pringle et al. 2001; Clark & Bonnell 2004; Vazquez-Semadeni et al. 2007(@), especially in extragalactic systems (e.g., see Israel 2000). Also, the X-factor seems to yield reasonable column density estimates for gas on scales smaller than entire clouds (e.g., Wall 2006).

4. *Stronger dependence of peak T_R on N(H_2) than of Δv on N(H_2) is not explained.* DSS86 require that the observed velocity width of the line depends on the gas column density. However, there is evidence that it is the peak radiation temperature, $\mathrm{T_R}$, that depends on $\mathrm{N(H_2)}$ and that Δv has only a weak dependence on $\mathrm{N(H_2)}$ (see Figure 1 and Wall 2006; Heyer et al. 1996; Pichardo et al. 2000; Ostriker et al. 2001; Ballesteros-Paredes & Mac Low 2002).

The purpose of the current paper is to propose an improved approach for understanding the X-factor that will resolve, or at least mitigate, the problems with DSS86. For example, the explanation proposed here includes radiative transfer in a clumpy medium and shows how the optically thick CO J = 1 → 0 emission of a cloud can be sensitive to the optical depths of the individual clumps. As a result, this explanation will permit, in some circumstances, a very weak dependence on $\mathrm{T_K}$ and $\mathrm{n(H_2)}$. Also, even though we will also use the virial theorem (except in one case), we can apply it to scales smaller than entire clouds. And the X-factor in the current proposed explanation will lose its dependence on virialization in the optically thin case. In addition, the proposed approach will naturally explain the dependence of the peak $\mathrm{T_R}$ on $\mathrm{N(H_2)}$. This improved approach has shortcomings of its own, but nevertheless *represents the first major improvement in understanding the X-factor since*

DSS86, because it is the first formulation to include radiative transfer. (The reader may also consult Wall 2006c, for a very brief description of the method.)

2. A Formulation for the X-Factor

2.1. Radiative Transfer in a Clumpy Cloud

The X-factor may yield a reasonable estimate of the molecular gas column density, because the integrated intensity of the CO J = 1 → 0 line is essentially counting optically thick clumps in the gas in the beam (e.g., see Evans 1999). Two clumps on the same line of sight within the beam will be, on average, separated in velocity by more than the velocity widths of the individual clumps, thereby allowing the clumps to contribute their intensities to separate velocities within the line profile without absorption of the emission from the more distant clump. And clumps at the same velocity within the line profile will be, on average, at different locations within the beam, their intensities simply added together at that velocity within the profile. This explanation does not, by itself, directly relate the masses of individual clumps to the observed integrated intensity, because, again, the clumps are optically thick in the CO J = 1 → 0 line. Applying *only* the DSS86 approach to the clumps will not work, because, as discussed in the introduction, DSS86 and the observed value of the X-factor together require densities an order of magnitude lower than is found in the clumps of real clouds. The DSS86 derivation of the X-factor depends on the beam-averaged column density, N, and the observed velocity width, Δv. We need a treatment of the problem in which the beam-averaged quantities, N and Δv, are cancelled out in favor of the corresponding quantities for an individual clump, i.e., N_c and $\Delta \mathrm{v_c}$. And we need a treatment of the radiative transfer in a clumpy medium.

Martin et al. (1984) (hereafter MSH84) developed a method for describing radiative transfer through a clumpy medium in a highly simplified case: they assumed that each clump was homogeneous and in LTE. For additional simplicity, they also assumed that the clumps were identical, although they pointed out that their method could be easily generalized to clumps with a spectrum of properties (see the Appendix of MSH84). The assumption of LTE was necessary because the implicit assumption is that the excitation temperature *of the transition* is constant throughout each clump, which is easily attained if the density is high enough for LTE. If the density is *not* high enough for LTE, then the populations of the rotational levels are affected by the ambient radiation field at the frequency of the line: all other things being equal, the molecules on the surface of a clump will be less excited than those in the clump center, because the former only see the radiation from roughly 2π steradians of solid angle, while the latter see it from the full 4π steradians.

This results in a spatial gradient in the line's excitation temperature. If the density *is* high enough for the transition to be in LTE, then this excitation temperature will be equal to the kinetic temperature of the gas throughout the clump. Since the clump is assumed to be homogeneous, this kinetic temperature is constant throughout the clump, thereby ensuring that the line's excitation temperature is also constant. These assumptions are particularly appropriate for the CO J = 1 → 0 line: because of its high optical depth (i.e., $\tau \sim \ few$) and low critical density (i.e., $n_{_{crit}} \simeq 3 \times 10^3\,\mathrm{cm}^{-3}$), this line is largely thermalized (i.e., close to LTE). Hence the method of MSH84 is appropriate here.

MSH84 used a statistical approach to find the appropriately averaged optical depth on a sightline through a cloud with clumps in a vacuum. The effective optical depth on a given sightline was expressed in terms of the individual clump opacities and the mean number of clumps on a sightline with velocities within a clump's velocity width for the case of identical clumps. This effective optical depth is the expectation value of the total optical depth of the clumps on a given sightline, considering the probability of a given clump impact parameter with respect to the sightline (i.e., perpendicular displacement of the clump center from the sightline) and, accordingly, of a given line-of-sight optical depth through each clump. Computing this expectation value then depends on an average opacity over all impact parameters for each clump, which is the appropriately determined average opacity over the clump's surface area projected in the sightline's direction. The appropriate average of the optical depth is determined from the average over values of $[1 - exp(-\tau)]$ and *not* over τ itself because the observed emission depends directly on the former and only indirectly on the latter — and the relationship between the two is non-linear. Accordingly, the effective optical depth, τ_{ef}, is given by $1 - exp(-\tau_{ef}) = \langle 1 - exp(-\tau) \rangle$, which implies $exp(-\tau_{ef}) = \langle exp(-\tau) \rangle$, where $\langle\rangle$ indicates expectation value. In the approximation of the spectral line width, Δv, being much larger than the velocity width of an individual clump, $\Delta \mathrm{v_c}$, τ_{ef} can be expressed as the product of the number of clumps per clump velocity width on a sightline and the effective optical depth of an individual clump. If N is the beam-averaged gas column density and $\mathrm{N_c}$ is the gas column density averaged over the projected area of a single clump, then $(N/\mathrm{N_c})(\Delta \mathrm{v_c}/\Delta \mathrm{v})$ is the number of clumps per sightline averaged over the beam per clump velocity width at the line central velocity. (Note that MSH84 defined N as the number of clumps per unit projected cloud area rather than the column density of gas. Note also that, below, $\mathrm{N_c}$ is actually the column density on the central sightline through the clump, but this change in definition accords with the definition of the clump average optical depth; see Appendix A for details.) If τ_0 is the optical depth on a sightline through the center of a single clump, then, following MSH84, $\mathrm{A}(\tau_0)$ is the clump effective optical depth. (Note that MSH84 called $\mathrm{A}(\tau_0)$ the effective optically thick area of the clump. Even though their term is more accurate, the simpler "clump effective optical depth" is adopted here.)

Consequently,

$$\tau_{ef}(v_z) = \frac{N}{\mathrm{N_c}} \frac{\Delta \mathrm{v_c}}{\Delta \mathrm{v}} \, \mathrm{A}(\tau_0) \exp\left(-\frac{{v_z}^2}{2\,\Delta \mathrm{v}^2} \right) \quad , \tag{1}$$

where v_z is the velocity component along the sightline and where a Gaussian line profile has been assumed. If $\tau(x, y)$ is the clump optical depth on the sightline at position (x,y) with respect to a sightline through the clump center, then the clump effective optical depth is given by

$$\mathrm{A}(\tau_0) = \frac{1}{\sqrt{2\pi}\ \Delta \mathrm{v_c}\ a_{_{eff}}} \int \mathrm{dv} \int \mathrm{dx} \int \mathrm{dy} \left\{ 1 - \exp\left[-\tau(\mathrm{x,y}) \exp\left(-\frac{v^2}{2\,\Delta \mathrm{v_c^2}} \right) \right] \right\} \quad , \tag{2}$$

where $a_{_{eff}}$ is clump's effective projected area defined in terms of its optical depth:

$$a_{_{eff}} \equiv \frac{1}{\tau_0} \int dx \int dy \ \tau(x, y) \quad . \tag{3}$$

The τ_0 is simply $\tau(x = 0, y = 0)$, the optical depth through the clump's center and at the center of the clump's velocity profile. The integrals are over the projected area of the clump and over the clump's velocity profile. For more details, see MSH84 and Appendix A. Figure 2 shows the variation of $\mathrm{A}(\tau_0)$ as a function of τ_0 for two types of clumps: cylindrical (seen orthogonally to the axis of symmetry) and spherical.

The observed line radiation temperature, $\mathrm{T_R}$, is then related to τ_{ef} by the usual expression

$$\mathrm{T_R}(\nu) = \mathcal{J}_\nu(\mathrm{T_K}) \ [1 - \exp(-\tau_{\mathrm{ef}})] \qquad , \tag{4}$$

where

$$\mathcal{J}_\nu(\mathrm{T_K}) \equiv \frac{\mathrm{h}\nu}{\mathrm{k}} \left\{ \left[\exp\left(\frac{\mathrm{h}\nu}{\mathrm{k T_K}} \right) - 1 \right]^{-1} - \left[\exp\left(\frac{\mathrm{h}\nu}{\mathrm{k T_{BG}}} \right) - 1 \right]^{-1} \right\} \quad . \tag{5}$$

$\mathrm{T_K}$ and $\mathrm{T_{BG}}$ are the gas kinetic and cosmic background temperatures, respectively. As stated earlier, LTE is assumed for the emission of the spectral line at frequency, ν. The $\mathcal{J}_\nu(\mathrm{T_K})$ is the source function in temperature units and is the correction for the cosmic microwave background emission and for the failure of the Rayleigh-Jeans approximation. Of course when $\tau_{ef} \ll 1$, we have the simplified form of equation (4):

$$\mathrm{T_R}(\nu) = \mathcal{J}_\nu(\mathrm{T_K})\, \tau_{\mathrm{ef}} \quad . \tag{6}$$

This is often called the "optically thin limit" for the equation of radiative transfer. A very interesting and important point here is that the effective optical depth is in the optically thin limit *even though the individual clumps can still be quite optically thick.* And this, of

course, will provide a partial explanation for the X-factor. Substituting equation (1) into equation (6) yields

$$\mathrm{T_R}(v_z) = \mathcal{J}_\nu(\mathrm{T_K})\,\frac{\mathrm{N}}{\mathrm{N_c}}\frac{\Delta \mathrm{v_c}}{\Delta \mathrm{v}}\,\mathrm{A}(\tau_0)\exp\left(-\frac{{v_z}^2}{2\,\Delta \mathrm{v}^2}\right) \quad , \tag{7}$$

As mentioned previously, the quantity $(N/\mathrm{N_c})(\Delta \mathrm{v_c}/\Delta \mathrm{v})$ is the number of clumps per sightline averaged over the beam within a clump velocity width at the line central velocity. (Note that this is not exactly correct. See the last paragraph of Appendix A for an explanation.) This quantity can be much less than unity, thereby permitting $\tau_{ef} \ll 1$ even for $\mathrm{A}(\tau_0) \gg 1$. (When $(N/\mathrm{N_c})(\Delta \mathrm{v_c}/\Delta \mathrm{v}) < 1$, it is similar to the geometric area filling factor within a narrow velocity interval, although it is not *necessarily* equivalent.) Since $\mathrm{A}(\tau_0)$ is roughly equivalent to $[1 - exp(-\tau)]$ for a single clump, the meaning of expression (7) is clear: it is the specific intensity of a single clump at velocity v_z — $\sim \mathcal{J}_\nu(\mathrm{T_K})\,[1 - \exp(-\tau)]$ — multiplied by the number of clumps at that velocity within a clump velocity width — $(N/\mathrm{N_c})(\Delta \mathrm{v_c}/\Delta \mathrm{v})\exp[-{v_z}^2/(2\,\Delta \mathrm{v}^2)]$. Simply multiplying the intensity of a single clump by the number of clumps gives the observed intensity *if* the clumps are radiatively de-coupled, and this is ensured if $\tau_{ef} \ll 1$. As τ_{ef} increases and becomes optically thick, the different clumps within each velocity interval start absorbing each other's emission and the radiation temperature approaches the source function $\mathcal{J}_\nu(\mathrm{T_K})$ asymptotically.

We are now better equipped to understand the behavior of the curves in Figure 2. $\mathrm{A}(\tau_0)$ represents the level of emission from a single clump averaged over the clump's projected area. When $\tau_0 \ll 1$, $\mathrm{A}(\tau_0) \simeq \tau_0$ because all lines of sight through the clump and the line's profile at all the clump's internal velocities are optically thin. As τ_0 increases past unity, the line profiles on sightlines passing near the clump's center start saturating in their cores and $\mathrm{A}(\tau_0)$ starts deviating noticeably from the $\mathrm{A}(\tau_0) = \tau_0$ line. Nevertheless, $\mathrm{A}(\tau_0)$ continues rising with increasing τ_0 because sightlines away from the clump's center are still optically thin. Even for sightlines near the clump's center, the line remains optically thin at velocities outside the line's core. As τ_0 continues increasing, $\mathrm{A}(\tau_0)$ deviates further and further from the $\mathrm{A}(\tau_0) = \tau_0$ line because the area of optically thick emission slowly increases outwards from the sightline through the clump center, covering more and more of the clump's projected area. The optically thick portion of the line profile on each sightline increases as well. Nevertheless, $\mathrm{A}(\tau_0)$ continues growing because of those lines of sight and those velocities at which the emission is still optically thin. Figure 2 shows two curves: one for a cylindrical clump of gas (i.e. a filament) and one for a spherical clump. The cylinder is viewed side-on (i.e. with its symmetry axis perpendicular to the sightline) and has length h. If the symmetry axis is the x-axis, then a Gaussian variation of the optical depth with y was adopted:

$$\tau(x,y) = \tau_0\, exp\left(-\pi h^2 \frac{y^2}{{a_{eff}}^2}\right) \quad . \tag{8}$$

The spherical clump also has Gaussian spatial variation with optical depth, but with radial distance, p, from the central sightline through the clump:

$$\tau(x,y) = \tau_0 \, exp\left(-\pi \frac{p^2}{a_{_{eff}}}\right) \quad , \tag{9}$$

where $p = \sqrt{x^2+y^2}$. This case was also treated by MSH84, and it is included here for comparison. (Note that the $a_{_{eff}}$ used here corresponds to the r_o^2 of MSH84.) The effective optical depth of the spherical clump grows faster with τ_0 for $\tau_0 \gtrsim 1$ than that of the cylindrical clump because the former's optically thick area is growing simultaneously in two dimensions, whereas the latter's grows only in one. While $\mathrm{A}(\tau_0)$ can grow without bound in these idealized cases, $\mathrm{T_R}$ cannot. Eventually, $\mathrm{A}(\tau_0)$ will grow large enough that $\tau_{ef} \ll 1$ is no longer valid and $\mathrm{T_R}$ asymptotically approaches $\mathcal{J}_\nu(\mathrm{T_K})$. The growing τ_0 causes this to happen because the clumps start crowding each other spatially and in velocity, due to their increasing optically thick areas and their increasingly saturated line profiles.

The curves of Figure 2 demonstrate that we can represent them as power-laws in τ_0 for $\tau_0 \leq 1$ or $\tau_0 \geq 3$:

$$\mathrm{A}(\tau_0) \simeq \mathrm{k_A} \, \tau_0^{\epsilon} \quad . \tag{10}$$

The values of k_A and ϵ obviously depend on the specific $\tau(x,y)$ — the opacity structure of the clump, except in the optically thin case. When $\tau_0 < 1$, we have $k_A = 1$ and $\epsilon = 1$, regardless of the specific variation of $\tau(x,y)$. A lower value of ϵ, i.e. closer to zero, indicates a clump with a better defined outer edge like a hard sphere. Conversely, aside from the optically thin case, a higher value of ϵ, i.e. closer to unity, indicates a clump with a more tenuous, or fluffier, outer region. Accordingly, ϵ will be called the "fluffiness" of the clump.

2.2. Relating Clump Velocity Width with Column Density

DSS86 required virialization in order to relate the line velocity width to the gas column density. That is also required here, but it will be combined with the radiative transfer in a clumpy cloud discussed in the previous subsection. The virial theorem in its simplest form neglects the effects of surface pressure and magnetic fields, yielding

$$2\,T + W = 0 \quad , \tag{11}$$

with T as the total internal kinetic energy of the cloud and W as its total internal potential energy. Assuming a spherical clump of uniform density gives

$$W = -\frac{3}{5}\frac{G\,M_c^2}{R} \quad , \tag{12}$$

where M_c and R are the clump mass and radius, respectively. The total kinetic energy is

$$T = \frac{1}{2}\, M_c\, \Delta v_{3d}^2 \quad . \tag{13}$$

The Δv_{3d} is the three-dimensional velocity dispersion of the gas. The exact kind of velocity dispersion this is depends on a number of factors, including the radiative transfer through the gas (E. Vazquez Semadeni, priv. comm.). Nevertheless, this velocity width most closely resembles an rms width. The Δv_{3d} is related to the one-dimensional velocity dispersion $\Delta \mathrm{v_c}$ by $\Delta v_{3d}^2 = 3\, \Delta \mathrm{v_c^2}$. If we assume that molecular hydrogen is the only form of hydrogen in the gas with number density, n_c, then the mass of the spherical clump is

$$M_c = \frac{4\pi}{3} n_c \mu \mathrm{m_{H2}} \mathrm{R}^3 \quad . \tag{14}$$

$\mathrm{m_{H2}}$ is the mass of the hydrogen molecule, μ is the helium correction, and R is the clump radius. The density n_c is related to the column density through the clump center by $n_c = \mathrm{N_c}/L_c$, where L_c is the path length on the central sightline through the clump is equal to $2R$. Substituting equations (13), (14), and (12) into (11) gives us

$$\Delta \mathrm{v_c} \;=\; k_v\, \mathrm{N_c^{0.5}}\, \mathrm{L_c^{0.5}} \tag{15}$$

and

$$k_v \;\equiv\; \left(\frac{\pi}{15}\, G\, \mu \mathrm{m_{H2}}\right)^{0.5} \quad . \tag{16}$$

Numerically in cgs units, this is

$$k_v \;=\; 2.47 \times 10^{-16} \quad ,$$

where $\mu = 1.3$ was used. For a more detailed treatment of spherical clumps, see Appendix C. (Also, see Appendix D for a treatment of cylindrical clumps.)

2.3. Relating Clump Optical Depth with Column Density

The clump optical depth on the sightline through the clump's center, τ_0, can be written in terms of the column density of CO in level J, N_J:

$$N_J = \frac{8\pi}{A_{J,J-1} \lambda_{J,J-1}^3} \left[exp\left(\frac{T_{J,J-1}}{T_K}\right) - 1 \right]^{-1} \tau_0 \sqrt{2\pi} \Delta \mathrm{v_c} \quad . \tag{17}$$

This comes from equation (A9) of Wall (2006) after applying the Boltzmann factor to change N_{J-1} to N_J. The velocity integral was replaced by $\tau_0 \sqrt{2\pi} \Delta \mathrm{v_c}$, where τ_0 is the optical depth

at the center of the clump's velocity profile and on the sightline through the clump's center. $T_{_{J,J-1}}$ is the energy of the $J \rightarrow J-1$ transition in units of temperature: i.e., $T_{_{J,J-1}} = h\,\nu_{_{J,J-1}}/k$ with $\nu_{_{J,J-1}}$ as the frequency of the transition. $A_{_{J,J-1}}$ and $\lambda_{_{J,J-1}}$ are the spontaneous transition rate and the wavelength of the transition, respectively. LTE is assumed, so $\mathrm{T_K}$ applies in place of $\mathrm{T_X(J \rightarrow J-1)}$. We can determine the total column density of CO, $N(CO)$, by substituting equation (17) into equation (A22) of Wall (2006):

$$N(CO) = \frac{8\pi}{(2J+1)A_{_{J,J-1}}\lambda^3_{_{J,J-1}}}\,Q(T_{_K})\,exp\left(\frac{T_{_{J,0}}}{T_{_K}}\right)\left[exp\left(\frac{T_{_{J,J-1}}}{T_{_K}}\right)-1\right]^{-1}\tau_0\sqrt{2\pi}\Delta\mathrm{v_c} \quad , \quad (18)$$

where $Q(T_{_K})$ is the partition function of CO. Setting J to 1 and rearranging for τ_0 results in

$$\tau_0 = \frac{3A_{10}\lambda^3_{10}}{8\sqrt{2}\,\pi^{\frac{3}{2}}\Delta\mathrm{v_c}\mathrm{Q(T_K)}}\left[1-exp\left(-\frac{T_{10}}{T_{_K}}\right)\right]\mathrm{N_c}X(CO) \quad . \quad (19)$$

The $N(CO)$ was replaced by $\mathrm{N_c}X(CO)$, where $X(CO)$ is the abundance of CO relative to H_2. The following values are used (see Wall 2006, and references therein): $A_{10} = 7.19 \times 10^{-8}\,\mathrm{s^{-1}}$, $T_{10} = 5.54\,\mathrm{K}$, $\lambda_{10} = 0.2601\,\mathrm{cm}$, and $X(CO) = 8 \times 10^{-5}$. Accordingly,

$$\tau_0 = \frac{1.21 \times 10^{-14}}{\sqrt{2\pi}\Delta\mathrm{v_c}\mathrm{Q(T_K)}}\left[1-exp\left(-\frac{5.54}{T_{_K}}\right)\right]\mathrm{N_c} \quad . \quad (20)$$

The above expression can be represented more simply as a power-law in $\mathrm{T_K}$:

$$\tau_0 = \frac{k_\tau}{\sqrt{2\pi}\Delta\mathrm{v_c}}\,\mathrm{N_c}\mathrm{T_K^{-\gamma}} \quad . \quad (21)$$

The exact values of k_τ and γ depend on the temperature range and can be computed by numerically comparing expressions (21) and (20). In the high-temperature limit, however, an analytical solution is possible. This limit means that $\mathrm{T_K} \gg T_{10}$ and $Q(\mathrm{T_K}) \rightarrow 2\mathrm{T_K}/T_{10}$ and $[1-exp(-T_{10}/T_{_K})] \rightarrow T_{10}/T_{_K}$. This results in $k_\tau = 1.85 \times 10^{-13}$ in *cgs* units and $\gamma = 2$. But we will be interested in the temperature range $\mathrm{T_K} = 10$ to $20\,\mathrm{K}$. The necessary numerical comparison gives us

$$k_\tau \;=\; 7.23 \times 10^{-14}\;(cgs\;units)$$

and

$$\gamma \;=\; 1.75$$

for that range. This approximation is accurate to within 1-2% on the above specified range. Equation (21) simplifies further by using expression (15) for $\Delta\mathrm{v_c}$ and $n_c = \mathrm{N_c}/L_c$:

$$\tau_0 = \frac{k_\tau}{k_v\sqrt{2\pi}}\,n_c^{0.5}\mathrm{T_K^{-\gamma}} \quad . \quad (22)$$

This interesting result suggests that the optical depth for this simplified case (i.e., the velocity profile of the optical depth is a simple Gaussian) of a virialized clump does not explicitly depend on the sightline pathlength nor the velocity width, but on their ratio. This is related to the Sobolev approximation (e.g., see Shu 1991) in which the optical depth is dependent on the velocity gradient within a given region and not explicitly on the region's size. The pathlength-to-velocity-width ratio ($L_c/\Delta \mathrm{v_c}$) in a virialized clump is determined by the average density, the spatial variation of the density, and the geometry. Therefore, the optical depth depends on those things and the gas temperature, but with *no* dependence on the clump size or velocity width (at least for this simplified case).

2.4. The X-Factor

Understanding how to combine the results of the previous subsections to derive an expression for the X-factor requires examining the observational data that inspired the current paper in the first place. Figure 3 shows the Orion data discussed in Wall (2006): the peak radiation temperature of the ^{12}CO J = 1 → 0 line (i.e., $\mathrm{T_R}$) for various positions in the Orion clouds normalized to the source function at each position (i.e., $\mathcal{J}_\nu(\mathrm{T_K})$) versus the gas column density (i.e., $\mathrm{N(H_2)}$) as determined from ^{13}CO J = 1 → 0. The plots demonstrate a clear correlation between $\mathrm{T_R}/\mathcal{J}_\nu(\mathrm{T_K})$ and $\mathrm{N(H_2)}$. The Spearman rank-order correlation test indicates that the correlation exists at better than the 99.99% confidence level. (In fact, the confidence level of the null proposition of *no* correlation is zero to within the machine precision — 10^{-38}.) This is more than just the expected correlation between the J = 1 → 0 lines of ^{12}CO and ^{13}CO, because the $\mathcal{J}_\nu(\mathrm{T_K})$ is determined from the dust temperature (see Wall 2006, for details). This suggests that the dust temperature really is a reliable measure of the kinetic temperature of the molecular gas, at least for the Orion clouds on the scales of parsecs (see Wall 2006,a,b, for more discussion of this). One way of explaining the correlation visible in Figure 3 is that the area filling factor of the clump in each clump velocity interval is less than unity. A rising beam-averaged column density, N, could mean that the filling factor is rising as more and more clumps fill the beam in each velocity interval. Eventually the clumps start crowding each other within the beam and within the line velocity profile and the $\mathrm{T_R}/\mathcal{J}_\nu(\mathrm{T_K})$ ratio starts to saturate and asymptotically approaches unity. (Another possibility is that N rises because of rising N_c within each clump, thereby increasing the clumps' optical depths. This would also produce the observed saturation effect without increasing the number of clumps within each velocity interval.) Obviously, the goal here is to be very specific about the relationship between $\mathrm{T_R}/\mathcal{J}_\nu(\mathrm{T_K})$ and $\mathrm{N(H_2)}$. There is sufficient scatter and uncertainty in the data that it is not possible to rule out *a priori* a number of such relationships.

Nevertheless, from simple radiative transfer theory, we know that the specific intensity of a source normalized to its source function, usually written I_ν/S_ν, will vary like $1-exp(-\tau)$ when plotted against the optical depth through the source, τ. Given that the column density, N, is proportional to τ for constant kinetic temperature and density, the data in Figure 3 mimic a curve with the form $1-exp(-aN)$ (see the plotted curves), where the aN probably represents some kind of optical depth. The majority of the data points are on the roughly linearly rising portion of the curve. This represents the optically thin region of the curve, *but the* ^{12}CO J = 1 → 0 *is known to be optically thick* from comparisons with the optically thin isotopologue ^{13}CO. Therefore, *a clue to understanding the X-factor is realizing that CO* J = 1 → 0 *emission behaves like it is optically thin, despite being optically thick.* This apparent contradiction is resolved when we consider the effective optical depth as described previously. While the individual clumps are themselves optically thick in CO J = 1 → 0, the cloud is optically thin "to the clumps." In other words, the emission from every clump in the telescope's beam through the cloud reaches the observer. An analogy would be observing the H I 21-cm line from an atomic cloud. In this case, the cloud is optically thin "to the atoms" in the sense that the emission from every atom in the telescope's beam through the cloud reaches the observer. And since every hydrogen atom is nearly identical in its 21-cm line emission properties, the conversion from I(H I) to N(H I) is physically straightforward and undisputed. For converting from I(CO) to N(H_2), assuming absolutely identical clumps would give a constant value of the X-factor, relatable to the clumps' properties. However, assuming identical clumps contradicts observational evidence (see, e.g., Tachihara et al. 2000; Nagahama et al. 1998; Kawamura et al. 1998; Onishi et al. 1996). But we need not restrict the clump properties so severely to explain the X-factor. All we need is to have the clumps similar *on average* from one beam to the next for the X-factor to stay relatively constant. And, of course, we must also allow the X-factor to vary in some cases (see Introduction); the clumps' average properties must vary from the "norm" in some clouds and locations.

We now need to quantify this picture, so that we might better understand it and its limitations. As Figure 3 clearly shows, the $T_R/\mathcal{J}_\nu(T_K) \propto N$ for $N \lesssim 1$ to $2 \times 10^{22}\, H_2\,cm^{-2}$. This is in the $\tau_{ef} \ll 1$ limit, so equation (7) applies and it has the desired proportionality. Of course, this proportionality is only visible if the clump properties — N_c, Δv_c, and $A(\tau_0)$ — and the observed line width, Δv, do not vary strongly with N. In fact, the scatter visible in the plots of Figure (3) is probably due to variations in all four of these quantities. Integrating equation (7) over velocity, v_z, gives

$$\begin{aligned} I(CO) &= \sqrt{2\pi}\, T_R(0)\, \Delta v \\ &= \sqrt{2\pi}\, \mathcal{J}_\nu(T_K) \tau_{ef}(0)\, \Delta v \quad . \end{aligned} \tag{23}$$

$T_R(0)$ is the radiation temperature of the CO J = 1 → 0 line at $v_z = 0$ and is also the peak radiation temperature of this line. Similarly, $\tau_{ef}(0)$ is the effective optical depth at $v_z = 0$.

The X-factor is then given by

$$X_f \;=\; \left[\sqrt{2\pi}\,\mathcal{J}_\nu(\mathrm{T_K})\,\tau_{\rm ef}(0)\,\Delta\mathrm{v}\,\mathrm{N}^{-1}\right]^{-1} \quad . \tag{24}$$

If we now substitute equation (1) evaluated at $v_z = 0$ into the above, then

$$X_f \;=\; \left[\sqrt{2\pi}\,\mathcal{J}_\nu(\mathrm{T_K})\,\mathrm{A}(\tau_0)\,\Delta\mathrm{v_c}\,\mathrm{N_c}^{-1}\right]^{-1} \quad . \tag{25}$$

The important thing to notice here is that the directly observed quantities, N and Δv, have been replaced by the corresponding clump properties, N_c and $\Delta\mathrm{v_c}$. In fact, all the parameters in expression (25) are clump parameters, as desired. It is convenient to define

$$C_T \;\equiv\; \frac{\mathrm{T_K}}{\mathcal{J}_\nu(\mathrm{T_K})} \quad . \tag{26}$$

We now use the approximation $\mathcal{J}_\nu(\mathrm{T_K}) \simeq \mathrm{T_K} - 3.4\,\mathrm{K}$ for $\mathrm{T_K} \gtrsim 10\,\mathrm{K}$ and the frequency of the ^{12}CO J = 1 → 0 line, $\nu = 115.271\,\mathrm{GHz}$. This is good to within 0.4% of $\mathrm{T_K}$ (and within 0.6% of $\mathcal{J}_\nu(\mathrm{T_K})$). Consequently,

$$C_T \;=\; \frac{\mathrm{T_K}}{\mathrm{T_K} - 3.4\,\mathrm{K}} \quad , \tag{27}$$

which approaches unity as $\mathrm{T_K}$ grows large. Now we substitute the results of the previous subsections into equation (25): equation (10) for $\mathrm{A}(\tau_0)$, (22) for τ_0, (15) for $\Delta\mathrm{v_c}$, and $\mathrm{T_K}/C_T$ for $\mathcal{J}_\nu(\mathrm{T_K})$. Except in the case of the end-on cylinder, where we defined the relationship between N_c and n_c differently, we also use $n_c = \mathrm{N_c}/L_c$. These substitutions yield

$$X_f = (2\pi)^{\frac{1}{2}(\epsilon-1)}\,C_T\,k_A^{-1}\,k_\tau^{-\epsilon}\,k_v^{\epsilon-1}\,\mathrm{T_K}^{\gamma\epsilon-1}\,n_c^{\frac{1}{2}(1-\epsilon)} \quad . \tag{28}$$

The expression (28) and its variants (e.g., see Appendices) will be examined in detail. It should be mentioned that expression (28) is more general than for just a clumpy medium and can also apply to a uniform-density cloud (see Appendix B).

The above formulation for X_f obviously accomplishes the goal of insensitivity to the parameters $\mathrm{T_K}$ and n_c that we have sought for X_f. The fluffiness parameter, ϵ, is in the range 0 to 1; any value in that range that is greater than 0 will confer a greater *in*sensitivity than occurs for the DSS86 explanation. A particularly interesting example is that value of ϵ for which $\gamma\epsilon - 1 = 0$. In the high temperature limit, $C_T \to 1$ and $\gamma \to 2$ and, if $\epsilon = 0.5$, then X_f *has no dependence on temperature.* (Notice that the density dependence is also very weak in this case: $X_f \propto n_c^{0.25}$.) Given that the CO J = 1 → 0 line is optically thick, this is counterintuitive; raising the temperature by some factor should simply increase $I(CO)$ by the same factor (in the high-$\mathrm{T_K}$ limit), thereby decreasing X_f by that factor. That is not the case here. Here we are dealing with a clumpy medium where the optical depth varies across

the projected area of each clump. There will always be some sightlines through a clump that will still be optically thin. There will also be some velocities in the clump's spectral line profile where the line emission is still optically thin. As T_K increases, τ_0 goes like T_K^{-2}, so that $A(\tau_0)$ goes like T_K^{-1} (see equations 21 and 10). But $\mathcal{J}_\nu(T_K)$ goes like T_K^1 (in this high-T_K limit), meaning that the observed T_R stays constant. The effect of the increasing kinetic temperature of the gas is cancelled by the decreasing effective optical depth of the clumps. Another way of saying this is that the effect of the rising temperature is cancelled by the shrinking effective optically thick areas of the clumps; the filling factors of the clumps decline as the temperature rises. (Note that this special case also occurs for lower temperatures. For $T_K = 10$ to 20 K, for example, $C_T \propto T_K^{-0.32}$ and $\gamma = 1.75$. The value of ϵ for which X_f is independent of temperature would be 0.75.) Therefore, *despite the optical thickness of the spectral line in the emitting clumps, changing the optical depths of the individual clumps will still have an appreciable effect on the line strength.* And this will reduce the dependence of the X-factor on the temperature and the density of the gas within the clumps.

In general, the X-factor provides estimates of gas column density because each sightline within the beam has some optically thin gas within certain narrow velocity ranges. Parameters like ϵ then allow extrapolation from the optically thin gas to all the gas.

One problem with the above analysis is that it assumes clumps of homogeneous density. This is inconsistent with most of the $\tau(x, y)$ functions that will be discussed in Section 3. The full analyses of these cases are given in the appendices.

3. Examination of the Properties of the X-Factor

In this section we examine the properties of the X-factor as formulated in the previous section.

3.1. Dependence on Clump Type

Here we examine how the X-factor relates to properties of the individual clumps, such as velocity width, optical depth, and mass. Accordingly, a "standard" clump — or, rather, a *set* of standard clumps — with specific input parameters must be adopted: geometry, dimensions, and density. These input parameters are based on the filamentary clumps as identified by Nagahama et al. (1998) with their ^{13}CO J = 1 → 0 map of the Orion A molecular cloud. (It should be mentioned here that the units responsible for the CO-line and dust-continuum emission may be subfragments within the filaments identified by Nagahama et al. (1998).

The filaments identified by that paper are nonetheless used as a first test of the X-factor's properties.) Table 2 of that paper lists the Orion A clumps and their characteristics, including dimensions and masses. Based on this table, the roughly cylindrical clumps have lengths ranging from 1.7 to 21 pc with a mean length of 6.2 pc, and diameters ranging from 0.7 to 3.5 pc with and a mean diameter of 1.8 pc. Using the mass-to-volume ratios, the average densities range from about 300 to 4000 $H_2 \cdot molecules \cdot \mathrm{cm}^{-3}$. Nagahama et al. (1998) also used ^{12}CO J = 1 → 0 data to estimate the gas kinetic temperature for each filament. Their Table 2 shows values ranging from about 10 to 40 K.

The adopted kinetic temperature and density values for the standard clumps use the above numbers in combination with other considerations. The adopted kinetic temperatures, for instance, also consider the numbers found for the Galactic disk at many-parsec scales. For example, the maximum temperature expected for the molecular gas and its dust on such scales in the Galaxy is about 20 K (e.g., see Sanders et al. 1985; Sodroski et al. 1994). Therefore, the standard clumps have adopted kinetic temperatures of either 10 K or 20 K, and not temperatures as high as the 30 to ∼40 K values in Table 2 of Nagahama et al. (1998). The adopted densities for the standard clumps are loosely related to the range of densities mentioned in the previous paragraph, but also expand the range to better explore the effect (or to demonstrate the lack of it) on the derived X-factor: the adopted densities for the standard clumps are 200, 2000, and 20000 $H_2 \cdot \mathrm{cm}^{-3}$.

The adopted dimensions for the standard clumps have no effect on the derived X-factor or clump optical depth (see equations 28 and 22), except in the case of a cylindrical filament viewed end-on. And even in that case, the derived X-factor still does not depend on the *individual* values of the diameter or length, but on their ratio (see Appendix D). Both the X-factor and clump optical depth depend on the clump temperature and average density, but *not* on clump size. Nevertheless, the clump dimensions still affect the derived clump mass and clump velocity width. For the spherical clumps, the adopted diameter is 1.8 pc — the same as the mean diameter of the observed Orion filaments. For the cylindrical filaments, the adopted length and diameter are 6.2 pc × 1.8 pc — again the same as the mean values of the observed Orion filaments.

Given that three kinds of density variations are considered for the spherical clumps and one for the cylindrical filamentary clumps, there are twenty-four standard clumps in the set. For each type of spherical clump, each with diameter 1.8 pc, there are six T_K,n_c combinations: T_K = 10 K, and n_c = 200, 2000, and 2000 $H_2\,\mathrm{cm}^{-3}$ and T_K = 20 K with those same three densities. For the single type of cylindrical clump, with *length* × *diameter* = 6.2 pc × 1.8 pc, there are the same six T_K,n_c combinations as for each type of spherical clump. The different kinds of density variations considered for the spherical clumps are as

follows: uniform, Gaussian, and squared Lorentzian. For the cylindrical filamentary clump, only the Gaussian radial density variation is considered, viewed from the side (perpendicular to the symmetry axis) and from the end (along that axis). All these cases are listed in Table 1, along with two extra cases discussed in the next two subsections.

The following subsections and the appendices examine these cases in detail, the results of which are summarized in Tables 1 – 5.

3.1.1. Completely Optically Thick Case: Optically Thick Disks with Flat-Topped Velocity Profiles

For this case we will examine face-on optically thick disks with completely flat-topped velocity profiles. This means that the optical depth of the ^{12}CO J = 1 → 0 line will be equal to τ_0 for all lines of sight through the clump and at every point in the velocity profile for each sightline. A(τ_0) would then have the thoroughly familiar form,

$$\mathrm{A}(\tau_0) = 1 - \exp(-\tau_0) \quad . \tag{29}$$

In the optically thick case, i.e. $\tau_0 \gtrsim 2$,

$$k_A = 1. \quad \text{and} \quad \epsilon = 0. \quad . \tag{30}$$

With fluffiness and k_A set to zero and unity, respectively, all dependence on optical depth parameters k_A, ϵ, k_τ, and γ disappears from expression (28), resulting in an expression for X_f that is devoid of radiative transfer:

$$X_f \;=\; (2\pi)^{-\frac{1}{2}}\, C_T\; k_v^{-1}\, \mathrm{T_K}^{-1}\, n_c^{\frac{1}{2}} \quad . \tag{31}$$

Numerically, this is

$$X_f(cgs) \;=\; 1.62 \times 10^{15}\; C_T\, \mathrm{T_K}^{-1}\, n_c^{\frac{1}{2}} \quad ,$$

or

$$X_f(X_{20}) \;=\; 1.62\; C_T\, \mathrm{T_K}^{-1}\, n_c^{\frac{1}{2}} \quad , \tag{32}$$

where the X-factor in (32) is in units of X_{20} or $10^{20}\, H_2 \cdot molecules \cdot\ \mathrm{cm}^{-2} \cdot (\mathrm{K} \cdot \mathrm{km} \cdot \mathrm{s}^{-1})^{-1}$. (Because the expressions 31 and 32 come from 28, we have actually assumed that the clumps are spheres rather than disks; the result is almost the same so long as A(τ_0) is given by 29.)

This of course is the DSS86 result with the $n_c^{0.5}/\mathrm{T_K}$ dependence for X_f. The resultant numerical values for X_f are listed in the first row of Table 1. Notice that these X_f values

are higher than those for the other cases. Also, notice that the only reasonable values for X_f occur for a density of $2 \times 10^2\, H_2\, \mathrm{cm}^{-3}$. Given that this result only occurs for this highly contrived case of optically thick disks with flat-topped velocity profiles, the DSS86 result is unlikely. Nevertheless, DSS86 represents a useful limit.

3.1.2. Completely Optically Thin Case

This case assumes that the line emission is optically thin on all sightlines through the clump and at all velocities within the line profile. Consequently, $\mathrm{A}(\tau_0) = \tau_0$ and

$$k_A = 1. \quad \text{and} \quad \epsilon = 1. \quad . \tag{33}$$

Now with fluffiness set to unity, dependence of X_f on k_v and n_c disappears. So expression (28) is free of the dependence on virialization; this is the exact opposite of the optically thick case discussed in the previous subsection. Accordingly,

$$X_f \;=\; C_T\; k_\tau^{-1}\, \mathrm{T}_\mathrm{K}^{\gamma-1} \quad . \tag{34}$$

For $\mathrm{T}_\mathrm{K} = 10$ to $20\,\mathrm{K}$,

$$X_f(X_{20}) \;=\; 1.38 \times 10^{-2}\; C_T\, \mathrm{T}_\mathrm{K}^{0.75} \quad . \tag{35}$$

These values of X_f are listed in the second row of Table 1. Notice that the X_f values are lower than those for the other cases. Equation 35 can also be written as,

$$N(H_2 \cdot cm^{-2}) \;=\; 1.38 \times 10^{18}\; C_T\, \mathrm{T}_\mathrm{K}^{0.75}\, I(CO)(K \cdot km \cdot s^{-1}) \quad . \tag{36}$$

Therefore, the relationship between column density and integrated intensity in the optically thin case is recovered. (This is easily verified by starting with expression 23 for $\mathrm{A}(\tau_0) = \tau_0$ and combining this with expression 21.)

3.1.3. Spherically Symmetric Clumps

Here we examine cases examined by MSH84: the hard sphere, the Gaussian sphere, and the squared-Lorentzian sphere. These examples do not necessarily represent the real clumps in real molecular clouds, but simply represent an interesting exploration of the parameter space that determines the X_f values. In all the cases considered in this paper, the clumps are isothermal and in LTE, implying that the clump optical depth as a function of impact parameter, or projected radius p, is proportional to that for the column density: $\tau_c(p) \propto N_c(p)$. See Appendix C for a detailed treatment of the spherically symmetric examples. As

stated at the beginning of Section 3.1, the spherical clumps considered here have radii equal to 1.8 pc.

First, the hard sphere example is examined. This is a uniform-density sphere with a well-defined edge at radius, R. Given that the density is uniform, the optical depth profile over the projected area of the clump is simply the sightline path-length for impact parameter, p:

$$\tau(p) = \tau_0 \left[1 - \left(\frac{p^2}{R^2}\right)\right]^{0.5} \quad , \tag{37}$$

the same as equation (12) of MSH84, with R in place of r_0. Using (37) along with (1), (2), and (3) yields the curve depicted with plus signs in Figure 5 of MSH84. Measuring the curve for $log\,\tau_0 \geq 0.5$ results in $k_A = 1.7$ and $\epsilon = 0.14$. Following the derivation in Subsections 2.2, 2.3, and 2.4 or in Appendix C yields expression (C13) for X_f. The numerical results for this case are listed in Tables 1 to 5 inclusive. The hard sphere is the case closest to the completely optically thick case and yields results within factors of a few of those of DSS86 (see Table 1). The hard sphere has the advantage of giving reasonable X_f values (i.e. $\sim 2\,X_{20}$ for reasonable densities (i.e. $\sim 10^3\,H_2\,\mathrm{cm}^{-3}$) and temperatures (i.e. 20 K), but has the disadvantage of sensitivity to density and temperature (i.e. $X_f \propto C_T\,n^{0.43}\mathrm{T_K}^{-0.76}$).

The Gaussian sphere has an optical depth profile given by expression (C15), with $\tau(p)$ and τ_0 in place of $N_c(p)$ and $n_0\,\sqrt{\pi}$, respectively. Using this $\tau(p)$ and the equations (1), (2), and (3) yields $\mathrm{A}(\tau_0)$ versus τ_0: the solid curve in Figure 5 of MSH84 and the dashed curve in Figure 2 of the current paper. Measurement of this curve gives $k_A = 1.6$ and $\epsilon = 0.36$ for $\tau_0 \geq 3$. The derivations in Subsection C.2 of Appendix C give the numerical results listed in Tables 1 to 5. As seen in Table 1, the expected X_f values for $\bar{\mathrm{n}} = 2 \times 10^3 H_2\,\mathrm{cm}^{-3}$ are within about a factor of 2 of the observed value for the Galactic disk. Also, expression (C19) shows that $X_f \propto C_T\,\bar{\mathrm{n}}^{0.32}\mathrm{T_K}^{-0.38}$, which is a greater *in*sensitivity to physical conditions than occurs for the hard sphere case.

The squared-Lorentzian sphere's optical depth profile is given by equation (C21), with a similar expression (i.e. C22) for the column density profile. Following the usual procedure gives the $\mathrm{A}(\tau_0)$ versus τ_0 curve: the "×" symbols in Figure 5 of MSH84, for which we find that $k_A = 1.5$ and $\epsilon = 0.57$. This particular optical depth profile has the advantage of low sensitivity to density and temperature (i.e. $X_f \propto C_T\,n^{0.22}\mathrm{T_K}^{-0.003}$), but the disadvantage of X_f values of roughly factors of 4 too low for a density of $\sim 10^3\,\mathrm{cm}^{-3}$.

In addition to the X_f values (i.e. Table 1), the tables also have the $\Delta\mathrm{v_c}$, τ_0, $\mathrm{A}(\tau_0)$, and M_c values (i.e. Tables 2 through 5 inclusive). The $\Delta\mathrm{v_c}$ and M_c in Tables 2 and 5, respectively, can be compared with the velocity widths and masses of the clumps in the Orion A cloud, as listed in Table 2 of Nagahama et al. (1998). Given that spherical clumps

with a diameter of 1.8 pc were adopted here, we need the roughly analogous clumps in Nagahama et al. (1998). These are the clumps numbered 14 and 23 in their Table 2, with dimensions 2.3 pc × 1.8 pc and 1.7 pc × 1.5 pc, respectively. The observed masses of these clumps, 330 $M_\odot$ and 220 $M_\odot$, suggest that they most closely resemble either the hard sphere of density 2000 cm^{-3} or the Gaussian sphere of average density 200 cm^{-3}. However, their observed velocity width of 1.1 $km \cdot s^{-1}$ suggests that they more closely resemble the hard sphere, but with about 2/3 the density, or $\sim 1300\,cm^{-3}$. Here we have also considered that the masses given in Table 2 of Nagahama et al. (1998) do not include the correction for helium. This lower density would imply $\Delta v_c \simeq 1.2\,km \cdot s^{-1}$, close to that observed. This implies that these clumps are virialized, as is required for a roughly constant X-factor to apply. However, hard spheres with $T_K \simeq 20$ K (see column 5 of Table 2 of Nagahama et al. 1998) and $n_c = 1300\,cm^{-3}$ would result in an X_f of about $1.3\,X_{20}$ or about 2/3 that observed for the Orion clouds (see Wall 2006; Dame et al. 2001). Consequently, clumps 14 and 23 are not entirely representative of the rest of the clumps of the Orion clouds.

Tables 3 and 4 give the optical depths on the central sightline, τ_0, and the clump effective optical depths, $A(\tau_0)$. The τ_0 values listed in Table 3 seem to be too high. The observed $I(^{13}CO)/I(^{12}CO)$ values for the Orion clouds (see Figure 5) are mostly in the range 0.1 to 0.4, implying $\tau(^{12}CO)$ of 6 to 24. However, Table 3 lists values that are an order of magnitude larger. Nevertheless, given that a roughly constant X-factor only occurs on large scales (i.e. many parsecs) and that the data for which the X-factor was estimated had a spatial resolution of about 1° (see Wall 2006), the relevant optical depth to use would be $A(\tau_0)$ and not τ_0. The former is listed in Table 4 and has values in the desired range and lower. (Although interpretation of the $I(^{13}CO)/I(^{12}CO)$ ratio is a little more complicated than in the case of homogeneous gas. See Section 3.3 for more details.)

3.1.4. Cylindrically Symmetric Clumps

Filaments or cylindrical clumps are discussed in detail in Appendix D. The behavior of these clumps — e.g., the derived τ_0 and X_f values — depend on whether these filaments are observed side-on (i.e., perpendicularly to their symmetry axes) or end-on (i.e., parallel to these axes). The filament considered here has a Gaussian density variation with distance from the central axis, viewed side-on and viewed end-on. As mentioned near the beginning of Section 3.1, the adopted dimensions of the filament are 6.2 pc × 1.8 pc.

For the case of the Gaussian cylinder viewed side-on, the optical depth, τ, as a function of projected distance from the central axis, y, is similar to equation (D8), but with $\tau(y)$ in place of $N_c(y)$ and τ_0 in place of $N_c(0)$. Using $\tau(y)$ with (1), (2), and (3) yields the solid

curve in Figure 2. Measuring the curve for $log\,\tau_0 \geq 0.5$ gives us $k_A = 1.5$ and $\epsilon = 0.25$. Side-on cylinders are expected to be less fluffy than spheres with the same optical depth profile, given that the former have optical depth variations in only one projected dimension and the latter have those variations in two projected dimensions. Here we see that the Gaussian side-on cylinder has a fluffiness that is only about 2/3 that of the Gaussian sphere (i.e. 0.25 versus 0.36). The derivation in Appendix D, Subsection D.1.1, gives the numerical results in Tables 1 to 5. As in the case of the Gaussian sphere, the resultant X_f values for an average density of $2 \times 10^3 H_2 \cdot \mathrm{cm}^{-3}$ are within a factor of 2 of the value inferred for our Galaxy. Like the hard sphere case, this X_f is a little too sensitive to $\mathrm{T_K}$ and $\bar{\mathrm{n}}$: $X_f \propto C_T\,\mathrm{T_K}^{-0.56}\,\bar{\mathrm{n}}^{0.37}$.

The Gaussian cylinder viewed end-on is similar to the Gaussian sphere in its optical depth profile. However, the central sightline optical depth, τ_0, depends on the cylinder length-to-diameter ratio or aspect ratio, $h/d_{1/2}$. Using the same k_A and ϵ as the Gaussian sphere, the derivation in Appendix D, Subsection D.2.1, gives the numerical results in Tables 1 to 5. The X_f value for an average density of $2 \times 10^3 H_2 \cdot \mathrm{cm}^{-3}$ and $\mathrm{T_K} = 20\,\mathrm{K}$ is very close to that observed for our Galaxy. Also like the Gaussian sphere, this X_f also has the advantage of relative insensitivity to $\mathrm{T_K}$ and $\bar{\mathrm{n}}$: $X_f \propto C_T\,\bar{\mathrm{n}}^{0.32}\mathrm{T_K}^{-0.38}$. Unfortunately, these advantages are merely lucky coincidences, because the X_f is dependent on the filament's aspect ratio ($X_f \propto (h/d_{1/2})^{0.64}$), which can vary by an order of magnitude or more. For example, the filaments of Orion A listed by Nagahama et al. (1998) have aspect ratios that vary from about 1 to 10. Another coincidence is that the end-on case implicitly assumes that the cylindrical filament is absolutely straight and pointing along the sightline — a low probability event.

Comparison of the results in Tables 1 to 5 with the clump properties listed in Table 2 of Nagahama et al. (1998) suggests that the Orion A filaments behave more or less like Gaussian cylinders, except for the inferred X_f values. Clumps 12, 22 and 33 have dimensions similar to the standard dimensions adopted here: $6.2\,\mathrm{pc} \times 1.8\,\mathrm{pc}$. The average densities of these filamentary clumps, $\bar{\mathrm{n}}$, can be inferred from the column densities divided by the product of the observed thicknesses and the k_N for a Gaussian cylinder (see Appendix D). These average densities and the dimensions can be combined to give the masses and velocity widths. These are found to agree with those in Table 2 of Nagahama et al. (1998) to within 7%, except for the velocity width of clump 33. The observed value for this clump is about double the virialized velocity width, strong evidence that this clump is not virialized. Another problem is the inferred X_f values. Table 2 of Nagahama et al. (1998) provides enough information to roughly estimate the X_f that would correspond to each of the filaments listed. Assuming side-on Gaussian cylinders for all 39 filaments listed gives $X_f = 0.6$ to $1.2\,X_{20}$, factors of roughly 2 to 4 lower than the estimated value for the Orion clouds (see Wall 2006; Dame et al. 2001). One way that the X_f can be raised to that estimated from

observations is to consider uniform-density filaments. As seen in Table 1 for the spheres for $\bar{n} = 2\times10^3\,cm^{-3}$, the uniform-density case (i.e., hard sphere) has X_f about a factor of 2 larger than for the Gaussian sphere. Accordingly, uniform-density filaments would correspond to higher X-factors, closer to that observed for Orion. One slight problem with uniform-density filaments is that the inferred virialized velocity widths are lower than those for the Gaussian filaments, resulting in a slightly greater number of non-virialized filaments. For uniform-density filaments, roughly half have velocity widths within 40% of the virial velocity widths. For Gaussian filaments, roughly half have velocity widths within 30% of the virial velocity widths.

3.1.5. Gravitationally Collapsing, Magnetized Filaments

The examples of clumps that have been examined up till now have all been virialized clumps. Strictly speaking, virialization is not required for determining X_f; all that is required is a relationship between the clump velocity width and the clump's density. Tilley & Pudritz (2003), for example, examine gravitationally collapsing, magnetized filaments. They investigate filaments with constant toroidal flux-to-mass ratio and those with constant thermal gas pressure to magnetic pressure. In the current paper only the former is considered (see Appendix D, Subsection D.3). Their equation (35) is rearranged to give the clump velocity width in terms of the density; see equation (D21). Tilley & Pudritz (2003) find that the density goes like $r^{-\alpha}$ at large r, where $\alpha = 2$ in the case of strong magnetic fields and $\alpha = 4$ for weak magnetic fields. Both of these cases are examined here.

For the case of $\rho(r) \propto r^{-2}$ (see Appendix D, Subsubsection D.3.1), the total clump mass, $M_c(r_1)$, depends on the ratio, r_1/r_0, where r_1 is the clump's outer radius and r_0 is the radius of the $\rho = constant$ core. In contrast, all the previous clump examples had finite $M_c(\infty)$. This dependence on r_1/r_0 also extends to $A(\tau_0)$. Numerically integrating (2) and (3) shows that ϵ is an increasing function of this ratio, asymptoting out at about 0.9 for $r_1/r_0 \gtrsim 5 \times 10^4$. It is clear then that the fluffiness of the filament depends not only on the density exponent, α, but also on the ratio r_1/r_0. As was found previously, increased fluffiness had the advantage of reduced sensitivity to T_K and $\bar{n}$, but the disadvantage of unrealistically low X_f. For example, for $r_1/r_0 = 1000$, we have $k_A = 1.46$, $\epsilon = 0.69$, and $X_f \propto C_T\, T_K^{0.21}\, \bar{n}^{0.16}$. To determine a value for X_f, we must specify a reasonable number for the fragmentation wavelength, λ_{frag}. The simplest way to specify this is to adopt the average cylinder length, 6.2 pc, that has been used up till now. Equation (35) of Tilley & Pudritz (2003) allows us to estimate this number. The observed Δv_c(FWHM) in most of the filaments in Orion A is 1-2 $km \cdot s^{-1}$ or velocity dispersions of 0.4-0.8 $km \cdot s^{-1}$ (after dividing by $\sqrt{8\,ln\,2}$). The

conversions from the central density to the average density are found in Appendix D. These together yield $\lambda_{frag} = 4.4$ to 8.8 pc for $\alpha = 2$ (and 3.5 to 7.0 pc for $\alpha = 4$). These numbers suggest that choosing $\lambda_{frag} = 6.2$ pc is acceptable. For reasonable temperature and density, $\mathrm{T_K} = 20\,\mathrm{K}$ and $\bar{\mathrm{n}} = 2000\,H_2 \cdot \mathrm{cm}^{-3}$, $X_f = 0.36\,X_{20}$, or a factors of ∼5 smaller than that for the Galaxy. On the other hand, if $r_1/r_0 = 10$, we have $k_A = 1.74$, $\epsilon = 0.27$, and $X_f \propto C_T\,\mathrm{T_K^{-0.53}}\,\bar{\mathrm{n}}^{0.37}$. For $\mathrm{T_K} = 20\,\mathrm{K}$ and $\bar{\mathrm{n}} = 2000\,H_2 \cdot \mathrm{cm}^{-3}$, $X_f = 1.6\,X_{20}$, which is close to the Galactic value. One problem with the $r_1/r_0 = 10$ case is that the power-law approximation for $\mathrm{A}(\tau_0)$ is noticeably poorer than for the othercases studied in the current paper. For these other cases, $\mathrm{A}(\tau_0) \simeq \mathrm{k_A}\,\tau_0^{\epsilon}$ is good to within about 13%. For $r_1/r_0 = 10$, it is only good to within about 26%.

For the case of $\rho(r) \propto r^{-4}$ (see Appendix D, Subsubsection D.3.2), $M_c(\infty)$ is finite and the power-law approximation for $\mathrm{A}(\tau_0)$ is as good as that for the majority of cases discussed in the current paper. Numerical integration of (2) and (3) yields $k_A = 1.15$ and $\epsilon = 0.37$, which results in $X_f \propto C_T\,\mathrm{T_K^{-0.36}}\,\bar{\mathrm{n}}^{0.32}$. For reasonable temperature and density, $\mathrm{T_K} = 20\,\mathrm{K}$ and $\bar{\mathrm{n}} = 2000\,H_2 \cdot \mathrm{cm}^{-3}$, $X_f = 1.9\,X_{20}$, which is approximately the value for molecular clouds in the Galactic disk.

One complication with the above analysis is that magnetized filaments have velocity dispersions that vary spatially within the filaments. The central velocity dispersion used in equation (35) of Tilley & Pudritz (2003) may differ from the observed velocity dispersion by a factor of about 2, as suggested by Figure 4 of Fiege & Pudritz (2000). If so, then λ_{frag} is a factor of two lower than the numbers used above. Of course, if this is true, then the value used for k_v must be increased by this factor of 2. Since X_f is a function of the product, $k_v\ \lambda_{frag}$, the factor of two decrease in λ_{frag} is cancelled by this factor of increase in k_v, leaving X_f unchanged.

The density dependences found for the collapsing, magnetized filament are those expected for an isothermal filament in hydrostatic equilibrium (Tilley & Pudritz 2003). Ostriker (1964) solved for the density distribution in an isothermal filament and found the $\rho(r) \propto r^{-4}$ at large r. This solution would also permit $\rho(r) \sim r^{-2}$ over a range of intermediate r. Since this is similar to the case of the collapsing, magnetized filament, how do the X_f values compare? The k_M values were computed in Appendix D, Subsection D.3, allowing determination of k_v for a virialized filament. Using the virialized k_v values and removing the $[d_{1/2}/(\lambda_{frag}\,k_{max})]^{(1-\epsilon)}$ factor will give the corresponding virialized X_f values. For $\rho(r) \propto r^{-2}$, X_f for the virialized, non-magnetic filament is up to nearly 20% smaller than that for the collapsing, magnetized filament. For $\rho(r) \propto r^{-4}$, X_f for the virialized, non-magnetic filament is almost 50% larger than that for the collapsing, magnetized filament. The X-factor values derived in the isothermal, virialized case are then easily within a factor of 2 of those for the

gravitationally collapsing, magnetized filament.

3.2. Other Effects on the X-Factor

3.2.1. Fluffiness

One advantage of the current, proposed formulation of the X-factor is that X_f can be insensitive to the kinetic temperature and density. But this advantage is coupled to an important disadvantage: X_f is sensitive to the fluffiness, ϵ. Another way of saying this is that the problem of sensitivity to temperature and density has been recast as one of sensitivity to another physical parameter. If real clumps in real clouds can indeed be characterized, at least approximately, with a parameter ϵ and if the proposed formulation of the X-factor is roughly correct, then a relatively constant X_f requires constant ϵ. Understanding the X-factor would then provide insights into molecular cloud structure. More specifically, the X-factor would itself be a probe of the opacity structure in CO-emitting clumps.

One obvious way to do this is to plot X_f as a function of ϵ and see what range of ϵ values gives realistic X_f values. This must be done for specific and realistic values of $\mathrm{T_K}$ and $\bar{\mathrm{n}}$, but the parameters k_A, k_v, and k_N have implicit dependences on ϵ. These dependences are not simple, given that they are affected by many things, such as geometry and density variations. However, these dependences are not strong and a crude variation of X_f versus ϵ can be plotted if we adopt "typical" values for these quantities: $k_A = 1.4$, $k_v = 3.4 \times 10^{-16}\, cgs$, and $k_N = 1.5$. These values along with $\bar{\mathrm{n}} = 2000\, H_2\, \mathrm{cm}^{-3}$ and $\mathrm{T_K} = 10$ and 20 K were substituted into equation (C11) to yield the curves of Figure 4. Note that the curve is about 30% lower than the level expected for $\epsilon = 0$ and $\epsilon = 1$ (cf. Table 1). This occurs because k_v, k_N, and especially k_A were fixed. Another point to consider is that the positions of these curves also depend on exactly how the "average" densities are defined. Nevertheless, the curves of Figure 4 still permit approximate estimates of ϵ in molecular clouds.

Figure 4 can estimate the range of ϵ that results in X_f within a factor of 2 of that for Galactic disk molecular clouds. Given that Galactic disk molecular clouds have $X_f \simeq 2\, X_{20}$ (Dame et al. 2001), what range of ϵ permits X_f to be in the range 1 to $4\, X_{20}$? For $\mathrm{T_K} = 20$ K and $\bar{\mathrm{n}} = 2000\, H_2\, \mathrm{cm}^{-3}$, $\epsilon = 0.0$ to 0.35. (Taking into account the underestimate of X_f for $\epsilon = 0$, this lower limit is more like 0.05.) For $\mathrm{T_K} = 10$ K and $\bar{\mathrm{n}} = 2000\, H_2\, \mathrm{cm}^{-3}$, $\epsilon = 0.17$ to 0.46. For $X_f = 2\, X_{20}$, $\epsilon = 0.15$ when $\mathrm{T_K} = 20$ K and $\bar{\mathrm{n}} = 2000\, H_2\, \mathrm{cm}^{-3}$ and $\epsilon = 0.31$ when $\mathrm{T_K} = 10$ K and $\bar{\mathrm{n}} = 2000\, H_2\, \mathrm{cm}^{-3}$. So for the adopted density, the clumps in Galactic disk molecular clouds behave most like hard spheres if $\mathrm{T_K} = 20$ K and roughly like Gaussian spheres or filaments if $\mathrm{T_K} = 10$ K. If instead the clumps are filaments with $\rho \propto r^{-2}$, then the

estimated ϵ values constrain the ratio of the maximum-to-minimum radii of the r^{-2} region, r_1/r_0. The $\epsilon = 0.15$ for $T_K = 20\,K$ and $\bar{n} = 2000\,H_2\,cm^{-3}$ requires $r_1/r_0 = 2$. The $\epsilon = 0.31$ for $T_K = 10\,K$ and $\bar{n} = 2000\,H_2\,cm^{-3}$ requires $r_1/r_0 = 16$.

In short, the likely range of ϵ is subject to a number of assumptions, but is probably $\epsilon = 0.05$ to 0.46. One point that should be emphasized is that the curves of Figure 4, for the given densities and temperatures, are *not* universal. These curves are dependent on the definition of average density (see Section 4.7.1).

3.2.2. CO Abundance

The effect of the CO abundance on the X-factor has been discussed in the literature (e.g., see Kutner & Leung 1985; Maloney & Black 1988). One might expect that X_f would depend only weakly on the CO abundance given that the ^{12}CO J = 1 → 0 line is optically thick. However, as discussed in Maloney & Black (1988), a reduced CO abundance means less self-shielding from the interstellar radiation field and a smaller CO-emitting volume, resulting in a lower area filling factor. The current proposed formulation would suggest a very specific dependence on the CO abundance, $X(CO)$. From equations (19) and (21) in Section 2.3, we see that $k_\tau \propto X(CO)$. Equation (28) tells us that $X_f \propto k_\tau^{-\epsilon}$. Accordingly, $X_f \propto X(CO)^{-\epsilon}$. Given that the most likely values for ϵ are between 0.05 and 0.46 (see Section 3.2.1), this is a weak dependence on the CO abundance.

However, a more relevant approach is to determine the dependence on the volume-averaged abundance. In irregular galaxies it has been found that CO is virtually absent over large volumes of molecular clouds, while having roughly Galactic abundance of CO within small central regions within those clouds (see Israel 1997a, 2000, and references therein). Accordingly, an *effective* CO abundance, $X(CO)$, is defined which is related to the Galactic CO abundance, $X_G(CO)$, within a spherical central region of radius, r_{co}, within a spherical clump of radius, r_1, by

$$X(CO) = X_G(CO)\ \left(\frac{r_{co}}{r_1}\right)^3 \qquad . \tag{38}$$

It is easy to show that the optical depth on the central sightline through the clump, τ_0, is proportional to r_{co}/r_1. From equations (7) and (10) we know that,

$$T_R(0) \propto \frac{N}{N_c}\ \tau_0^\epsilon \qquad . \tag{39}$$

The quantity N/N_c is the number of clumps per sightline averaged over the beam. It had been assumed up till this point that the entire volume of each clump was emitting in the

CO line. If we now only consider the case where the projected emitting area is less than the entire projected area of each clump, then it is easy to show that $N/\mathrm{N_c} \propto (\mathrm{r_{co}}/\mathrm{r_1})^2$. Putting all of this together yields,

$$X_f \propto X(CO)^{-\frac{1}{3}(\epsilon+2)} \quad . \tag{40}$$

Given that $\epsilon = 0.05$ to 0.46,

$$X_f \propto X(CO)^{-0.7\ to\ -0.8} \quad . \tag{41}$$

This is a considerably stronger dependence on the CO abundance than was derived in the previous paragraph. In fact, the derived dependence is nearly as strong as that expected for optically thin ^{12}CO J $= 1 \rightarrow 0$: $X_f \propto X(CO)^{-1}$. Notice that (40), in fact, has this dependence in the optically thin case: i.e., when $\epsilon = 1$.

Filamentary clumps may imply a different dependence of X_f on $X(CO)$ from that of spherical clumps. If the filaments are much longer than their diameters (i.e., high aspect ratio), then the dependence of $X(CO)$ on r_{co}/r_1 may be two-dimensional rather than three-dimensional. This is only an approximation because the strong radiation fields or low metallicities that can lead to low effective $X(CO)$ (see Israel 1997a, 2000, and references therein) would reduce the length of a filament's CO-emitting volume as well as its diameter. However, for a filament with a high aspect ratio, the *fractional* change would be larger for the diameter than for the length. As long as the effective $X(CO)$ is not extremely low, we can roughly assume that $X(CO) \propto (r_{co}/r_1)^2$. If the filaments are viewed side-on, $N/\mathrm{N_c} \propto \mathrm{r_{co}}/\mathrm{r_1}$. Using a similar approach to that for the spherical clumps,

$$X_f \propto X(CO)^{-\frac{1}{2}(\epsilon+1)} \quad . \tag{42}$$

Given that $\epsilon = 0.05$ to 0.46,

$$X_f \propto X(CO)^{-0.5\ to\ -0.7} \quad . \tag{43}$$

For end-on filaments it is simple to show that,

$$X_f \propto X(CO)^{-1} \quad , \tag{44}$$

regardless of the value of ϵ. Since filaments, on average, are viewed neither completely side-on nor completely end-on, the expected power-law index would be between -0.5 and -1.0. Again, notice that (42) gives the dependence expected in the optically thin case for $\epsilon = 1$. For (44) this optically thin dependence holds regardless of the value of ϵ, given that the effective $X(CO)$ is affected only by the *projected* area of the CO-emitting volume.

3.2.3. Effective Optical Depth

The proposed formulation for the X-factor assumes that the ^{12}CO J = 1 → 0 line is optically thin "to the clumps": i.e., $\tau_{ef} \ll 1$. But this is not necessarily the case. The panels of Figure 3 suggest that saturation starts for $N(H_2) \gtrsim 1$ to $2 \times 10^{22}\,\mathrm{cm}^{-2}$. Finding the ^{12}CO J = 1 → 0 brightness that corresponds to this surface density is *not* straightforward; the inferred τ_{ef} also depends on the source function, $\mathcal{J}_\nu(\mathrm{T_K})$. Another consideration is that the conditions for saturation that are inferred here really only apply to the Orion clouds and not necessarily to other clouds. Still another point is that the peak $\mathrm{T_R}$ is more relevant than the I(CO), because the latter includes the velocity width of the line. The I(CO) of an external galaxy, for instance, can have a very large velocity width often dominated by large-scale systematic motions, such as the large-scale rotation of the galaxy, rather than the smaller scale virialized velocity dispersions within individual clumps or clouds.

With these caveats in mind, it is at least possible to specify a rough minimum peak $\mathrm{T_R}$ as a *necessary* (and certainly *not* sufficient) condition for the start of saturation. Within the Orion clouds, this is $\mathrm{T_R} \gtrsim 6$ to 8 K, although there are still positions for which $\mathrm{T_R} \simeq 10$ to 12 K and $\tau_{ef} \ll 1$ still applies. So some measure of the source function is necessary to be certain that saturation is occurring.

If saturation is indeed a problem for some sources (or some positions within a source), then the actual X-factor necessary for determining the gas surface density could be factors of roughly two or more higher than the "standard" value applicable to most other sources (or to most other positions within a source). This saturation behavior of the X-factor can be understood better by examining either panel of Figure 3. The X-factor of a given point on the curve is proportional to the reciprocal of the slope of a line-segment joining the origin to that point. As the column density increases, the point moves to the right and the line-segment to the origin has an ever decreasing slope; the X-factor increases without bound. Therefore, in *this* optically thick limit, the ^{12}CO J = 1 → 0 line loses its sensitivity to column density, as expected.

3.2.4. Interclump Gas

Including the effects of a more or less continuous low-density medium between the clumps — an interclump gas — in the current treatment of the X-factor is beyond the scope of the current paper. Nonetheless, the effects of such gas on X_f can be crudely estimated.

From expressions (23), (10), and (1), we have

$$I(CO) = \sqrt{2\,\pi}\,\mathcal{J}_\nu(\mathrm{T_K})\,\frac{\mathrm{N}}{\mathrm{N_c}}\,\Delta\mathrm{v_c}\,\mathrm{k_A}\,\tau_0^\epsilon \qquad , \tag{45}$$

which assumes $\tau_{ef} \ll 1$, as used throughout most of this paper. Of course, the beam-averaged column density, N, is a measure of the mass of CO-emitting gas within the beam. If CO-containing gas is added to the beam, then $I(CO)$ increases. How $I(CO)$ increases depends on how this gas is added:

1. If the gas is added in the form of more clumps to each velocity interval, without changing the clumps' properties, then $I(CO) \propto N$ and $X_f = N/I(CO)$ remains constant.

2. If the added gas increases $\mathrm{N_c}$ of each clump, without changing the clumps' dimensions, then $N/\mathrm{N_c}$ remains constant and $\Delta\mathrm{v_c} \propto \mathrm{N_c^{0.5}}$. Given that $\tau_0 \propto \mathrm{N_c}/\Delta\mathrm{v_c}$, $I(CO) \propto N^{0.5(1+\epsilon)}$, requiring that $X_f \propto N^{0.5(1-\epsilon)}$.

3. If a very distended envelope is added to each clump, then $\mathrm{N_c}$ changes very little and $\Delta\mathrm{v_c} \propto \mathrm{N^{-0.5}}$. This is a dependence of $\Delta\mathrm{v_c}$ on N because the total mass in the beam has increased, which will change the velocity widths of the clumps, even though $\mathrm{N_c}$ has changed little. This is an inverse dependence of $\Delta\mathrm{v_c}$ on N because the mass is added at large distances from each clump center (see more discussion of this below). Again, it results that $I(CO) \propto N^{0.5(1+\epsilon)}$ and $X_f \propto N^{0.5(1-\epsilon)}$.

4. There are other cases where $\mathrm{N_c}$ is increased only a small amount, but $\Delta\mathrm{v_c}$ is increased by a bit more, resulting in $I(CO) \propto N^\beta$, where $\beta > 1$. (Note that if $\tau_0 < 1$, then $\beta = 1$, because $\epsilon = 1$ and $\tau_0\,(\Delta\mathrm{v_c}/\mathrm{N_c}) = 1$.) Hence, $X_f \propto N^{1-\beta}$ and X_f decreases with increasing N.

One thing to notice about all these cases is that, if the gas is optically thin in the ^{12}CO J $= 1 \rightarrow 0$ line (i.e. $\tau_0 < 1$ and $\epsilon = 1$), then $I(CO) \propto N$ and X_f is constant. Except for point #4 above, the addition of extra CO-emitting gas will increase, or leave unchanged, the X-factor. And point #4 does not necessarily represent a very common case.

A quantitative estimate of how strongly the interclump gas could affect X_f can come from assuming that such gas behaves like an envelope for each clump. The self-potential energy of such a clump-envelope system would be

$$W = -k_W\,y_W\,\frac{G\,M_c^2}{p_{1/2}} \qquad , \tag{46}$$

where k_W and M_c are the quantities that apply to the clump without the envelope and y_W is the correction due to the envelope. The internal kinetic energy is

$$T = \frac{1}{2}\,M_c\,\Delta v_{3d}^2\,(1\ +\ r_M) \qquad , \tag{47}$$

where

$$r_M \equiv \frac{M_e}{M_c} \tag{48}$$

is the mass ratio of the envelope to the clump without the envelope. The r_M is also

$$= r_\rho \, r_\sigma^3 \quad , \tag{49}$$

with

$$r_\rho \equiv \frac{\rho_{e0}}{\rho_{c0}} \tag{50}$$

as the ratio of the central densities of the envelope to bare clump. The r_σ is the ratio of sizes of envelope to bare clump. Employing the Virial theorem in its simplest form and $\Delta v_{3d}^2 = 3\,\Delta \mathrm{v_c^2}$ yields

$$\Delta \mathrm{v_c} = \mathrm{k_v\, y_v^{0.5}\, \bar{n}\, d_{1/2}} \quad , \tag{51}$$

with

$$y_v \equiv \frac{y_W}{1 \, + \, r_M} \quad . \tag{52}$$

The central column density of the clump-envelope system, $\mathrm{N_c}$, is

$$\mathrm{N_c} = 2\, k_N \, y_N \, \bar{\mathrm{n}} \, p_{1/2} \quad . \tag{53}$$

The k_N is the quantity for the bare clump and

$$y_N \equiv 1 \, + \, r_\rho \, r_\sigma \tag{54}$$

$$= 1 \, + \, r_M \, r_\sigma^{-2} \tag{55}$$

From expressions (51) and (53) we see that the k_v and k_N in expression (C11) for X_f must be replaced by $k_v \, y_v^{0.5}$ and $k_N \, y_N$, respectively. The formula for X_f ends up with an extra factor of $y_X^{1-\epsilon}$ in which

$$y_X \equiv y_N \, y_v^{-0.5} \quad . \tag{56}$$

We are now ready to estimate the effects of the interclump gas on the X-factor. To effectively be the interclump gas the envelope must extend far from the clump; i.e., $r_\sigma \to \infty$. Obviously, this yields $y_W \to 1$ and $y_v \to (1 \, + \, r_M)^{-1}$. Hence the addition of the envelope to the bare clump actually reduces the clump velocity width (see point #3 two paragraphs back). Because this limit implies that $y_N \to 1$, we have $y_X \to (1 \, + \, r_M)^{0.5}$. It is clear then that the interclump gas has only a small effect on X_f. If the interclump gas mass does not dominate the mass of the cloud, then $r_M < 1$ and X_f would increase by less than about 40%.

For r_σ not large, these numbers would be smaller. Also, the envelope would increase the effective ϵ and k_A of the clumps, thereby further decreasing the effect of the interclump gas on the X-factor. (A numerical test of this found that ϵ can increase by about 50%, requiring $r_\sigma = 10$ and the extreme $r_M = 10$. A less extreme $r_M = 1$ produced the usual ϵ but a 25% increase in k_A.)

Knowing the size of the effect on X_f for finite r_σ requires knowing the specific density variation within the clump and envelope. It is easy to show that for $r_\sigma = 1$ that $y_X = (1 + r_M)^{0.5}$ as it does for $r_\sigma \to \infty$. (This comes from $y_W = (1 + r_M)^2$ when $r_\sigma = 1$.) Therefore, for r_σ between 1 and ∞, y_X must achieve a minimum or a maximum. (And, since the envelope must surround the clump and not vice-versa, r_σ must be greater than unity.) Examining the cases of a uniform-density spherical clump and envelope and a Gaussian spherical clump and envelope shows that both these cases have a minimum for y_X in the desired range for r_σ. In the former case, this minimum is greater than unity but less than $(1 + r_M)^{0.5}$. In the latter case, the minimum of y_X is less than unity but greater than $(1 + r_M)^{-0.5}$. Therefore, the largest deviations from unity for y_X occur for r_σ large. Accordingly, only for r_σ large is the effect on the X-factor maximized; and even in this large-r_σ limit the effect is no more than 40% if $r_M \leq 1$. (Note that r_σ large means that $r_\sigma \gg r_M^{\frac{1}{3}}$ when $r_M < 1$ and $r_\sigma \gg r_M$ when $r_M > 1$ for the uniform-density case and $r_\sigma \gg r_M^{\frac{1}{2}}$ when $r_M < 1$ and $r_\sigma \gg r_M^2$ when $r_M > 1$ for the Gaussian case.)

Another point to consider is if the interclump gas has a different temperature from that of the clumps. Since this interclump gas is at a lower density than that of the clumps and, if there is even very crude pressure equilibrium between the clumps and interclump medium, then T_K(interclump) > T_K(clump). The warmer interclump gas could then possibly have appreciable emission compared to that of the clumps and reduce X_f appreciably. However, if there is true clump/interclump pressure equilibrium and if the density of the interclump gas is lower than that of the clump gas by an order of magnitude, then the temperature would be higher by an order of magnitude. This would bring down the optical depth of the ^{12}CO J = 1 → 0 line in the interclump medium by *two* orders of magnitude and could weaken its emission below what it would have been if T_K(interclump) = T_K(clump). If so, then the interclump gas would have an even weaker effect on the X-factor than has been estimated above.

Of course, the above analysis assumes that the dominant CO-emitting gas is in the clumps, so that the presence of the interclump gas only increases X_f. However, if the interclump gas were to dominate the mass of the cloud and its ^{12}CO J = 1 → 0 emission, then the appropriate average density to use in the expression for X_f would be considerably lower, thereby lowering X_f.

In summary, interclump gas would likely increase the X-factor by less than about 40%, so long as this gas did not dominate the mass of the cloud. If the interclump gas did dominate the mass, then the X-factor would be decreased, because the average density of the dominate CO-emitting gas would decrease. One other important effect of the interclump medium would be to increase the effective ϵ. Estimates of ϵ from inferred X_f values (and assumed or estimated clump densities and temperatures, see Section 3.2.1) or from ^{13}CO J = $1 \rightarrow 0/^{12}$CO J = $1 \rightarrow 0$ line ratios (see Sections 3.3 and 4.4) could be higher than those expected from just clumps alone.

3.3. ^{13}CO J = 1 → 0/^{12}CO J = 1 → 0

One implication of the proposed formulation is that there is an additional layer of complication in interpreting line ratios. For example, if two spectral lines have $\tau_{ef} \ll 1$, then the ratio of their intensities depends on the ratio their respective $\mathcal{J}_\nu(\mathrm{T_x})\,\mathrm{A}(\tau_0)$ values (where $\mathrm{T_x}$ is the excitation temperature of the transition), instead of depending on the ratio of their $\mathcal{J}_\nu(\mathrm{T_x})\,[1 - \exp(-\tau_0)]$ values. If the two spectral lines have similar optical depths (i.e. similar $\mathrm{A}(\tau_0)$ values) and $\tau_{ef} \ll 1$, then this complication is minimized. Given that the ^{12}CO to ^{13}CO abundance ratio is about 60 (e.g., Langer & Penzias 1990), the ratios of ^{13}CO lines to those of ^{12}CO still have this complication.

To appreciate this, we start with a uniform slab of gas in which the J = 1 → 0 lines of ^{12}CO and ^{13}CO are in LTE:

$$\frac{I(^{13}\mathrm{CO})}{I(^{12}\mathrm{CO})} \simeq \frac{1 - exp(-x_r\tau_{12})}{1 - exp(-\tau_{12})} \quad , \tag{57}$$

where x_r is the ^{13}CO/^{12}CO abundance ratio, $X(^{13}\mathrm{CO})/\mathrm{X}(^{12}\mathrm{CO})$. τ_{12} is the optical depth of ^{12}CO J = 1 → 0 and, in LTE, the optical depth of ^{13}CO J = 1 → 0, τ_{13}, is related to τ_{12} by $\tau_{13} = x_r \cdot \tau_{12}$. Expression (57) is an approximation because the integrated intensities are used here instead of the radiation temperatures at a particular velocity within the line profile. (It is also an approximation because the temperature corrected for the cosmic background and for failure of the R-J approximation, $\mathcal{J}_\nu(\mathrm{T_K})$, is slightly different for the the two J = 1 → 0 lines.) This line ratio has the following limiting cases:

$$\frac{I(^{13}\mathrm{CO})}{I(^{12}\mathrm{CO})} \simeq x_r \quad , \; for\ \tau_{12} \ll 1\ and\ \tau_{13} \ll 1, \tag{58}$$

$$\simeq 1 - exp(-x_r\tau_{12}) \quad , \; for\ \tau_{12} \gg 1, \tag{59}$$

$$\simeq x_r\tau_{12} \quad , \; for\ \tau_{12} \gg 1\ and\ \tau_{13} \ll 1, \tag{60}$$

$$\simeq 1 \quad , \; for\ \tau_{12} \gg 1\ and\ \tau_{13} \gg 1. \tag{61}$$

Equation (58) represents the uncommon case of optically thin ^{12}CO J $= 1 \rightarrow 0$ and has the unsurprising result that the line ratio is the abundance ratio when both lines are optically thin. Equation (60) shows a linear relationship between the line ratio and the abundance ratio. When both lines are optically thick, as represented by equation (61), the line ratio is completely insensitive to the abundance ratio.

If we now consider a clumpy medium and use the MSH84 formalism, then

$$\frac{I(^{13}\mathrm{CO})}{I(^{12}\mathrm{CO})} \simeq \frac{1 \; - \; exp(-a\tau_{ef,12})}{1 \; - \; exp(-\tau_{ef,12})} \qquad , \tag{62}$$

where $\tau_{ef,12}$ is the effective optical depth of the ^{12}CO J $= 1 \rightarrow 0$ line and where,

$$a \equiv \frac{\tau_{ef,13}}{\tau_{ef,12}} = \frac{\mathrm{A}(\tau_{0,13})}{\mathrm{A}(\tau_{0,12})} \qquad . \tag{63}$$

Here it is implicitly assumed that $\mathrm{A}(\tau_0)$ has the same functional form for both ^{12}CO J $= 1 \rightarrow 0$ and ^{13}CO J $= 1 \rightarrow 0$. This is not necessarily the case given that ^{13}CO can be selectively photodissociated more easily than ^{12}CO (Warin et al. 1996). Nevertheless, for simplicity, the same $\mathrm{A}(\tau_0)$ for both of the J $= 1 \rightarrow 0$ lines will be assumed here. Even for the same $\mathrm{A}(\tau_0)$, the k_A and ϵ values can be different if ^{13}CO J $= 1 \rightarrow 0$ and ^{12}CO J $= 1 \rightarrow 0$ are in different optical depth regimes (i.e. $\tau_0 \lesssim 1$ versus $\tau_0 \gtrsim 3$):

$$a = \frac{k_{A,13} \; \tau_{0,13}^{\epsilon_{13}}}{k_{A,12} \; \tau_{0,12}^{\epsilon_{12}}} \qquad . \tag{64}$$

When ^{13}CO J $= 1 \rightarrow 0$ is optically thin in the clump (i.e. $\tau_{0,13} \ll 1$), $k_{A,13} = 1$ and $\epsilon_{13} = 1$. If, at the same time, ^{12}CO J $= 1 \rightarrow 0$ is optically thick in the clump (i.e. $\tau_{0,12} \gtrsim 3$), then it is easy to see that

$$a = x_r \; k_A^{-1} \; \tau_0^{1-\epsilon} \qquad , \tag{65}$$

where the subscript "12" was omitted from the k_A and ϵ. In the other limit, when ^{13}CO J $= 1 \rightarrow 0$ is optically thick in the clump, $k_{A,13} = k_{A,12}$ and $\epsilon_{13} = \epsilon_{12}$ and

$$a = x_r^{\epsilon} \qquad , \tag{66}$$

where ϵ is both ϵ_{13} and ϵ_{12}. With these expressions in mind, the following limiting cases result:

$$\frac{I(^{13}\mathrm{CO})}{I(^{12}\mathrm{CO})} \simeq \; x_r \qquad , \; for \; \tau_{ef,12} \ll 1, \; \tau_{ef,13} \ll 1, \; \tau_{0,12} \lesssim 1, \; and \; \tau_{0,13} \lesssim 1, \tag{67}$$

$$\simeq \; x_r \, k_A^{-1} \, \tau_{0,12}^{(1-\epsilon)} \qquad , \; for \; \tau_{ef,12} \ll 1, \; \tau_{ef,13} \ll 1, \; \tau_{0,12} \gtrsim 3, \; and \; \tau_{0,13} \lesssim 1, \tag{68}$$

$$\simeq \; x_r^{\epsilon} \qquad , \; for \; \tau_{ef,12} \ll 1, \; \tau_{ef,13} \ll 1, \; and \; \tau_{0,13} \gtrsim 3, \tag{69}$$

$$\simeq \quad x_r\,\tau_{0,12}\,\frac{N}{\mathrm{N_c}}\,\frac{\Delta \mathrm{v_c}}{\Delta \mathrm{v}} \qquad , \; for\; \tau_{ef,12} \gg 1,\; \tau_{ef,13} \ll 1,\; and\; \tau_{0,13} \lesssim 1, \tag{70}$$

$$\simeq \quad x_r^{\epsilon}\,k_A\,\tau_{0,12}^{\epsilon}\,\frac{N}{\mathrm{N_c}}\,\frac{\Delta \mathrm{v_c}}{\Delta \mathrm{v}} \qquad , \; for\; \tau_{ef,12} \gg 1,\; \tau_{ef,13} \ll 1,\; and\; \tau_{0,13} \gtrsim 3, \tag{71}$$

$$\simeq \quad 1 \qquad , \; for\; \tau_{ef,12} \gg 1\; and\; \tau_{ef,13} \gg 1. \tag{72}$$

The k_A and ϵ are those for $\tau_0 \gtrsim 3$. Only in the last case is the line ratio completely independent of the abundance ratio. When $\tau_{0,13} \gtrsim 3$, $I(^{13}\mathrm{CO})/\mathrm{I}(^{12}\mathrm{CO}) \propto \mathrm{x_r^{\epsilon}}$ which is the same proportionality that the X-factor has in the case when the X(CO) is not spatially varying (see first paragraph of Section 3.2.3). This represents a very important contrast with the case of uniform gas: *even when both* $^{12}CO\; J = 1 \rightarrow 0$ and $^{13}CO\; J = 1 \rightarrow 0$ *are optically thick on the central sightlines of the clumps, the observed* $^{13}CO\; J = 1 \rightarrow 0/^{12}CO\; J = 1 \rightarrow 0$ *line ratio does* not *reach an asymptotic value of unity,* unless $\tau_{ef,13} \gg 1$. And when both $\tau_{ef,12} \ll 1$ and $\tau_{ef,13} \ll 1$ for $\tau_{0,13} \gtrsim 3$, the line ratio saturates near an asymptotic value that depends on the abundance ratio and the clump fluffiness.

Expression (62) and its limiting forms, (67) to (72) inclusive, can be applied to the ^{13}CO J = 1 → 0 and ^{12}CO J = 1 → 0 data of the Orion A and B molecular clouds (Wall 2006). The line ratio $I(^{13}\mathrm{CO})/\mathrm{I}(^{12}\mathrm{CO})$ is plotted against $\tau_{ef,12}$ in the panels of Figure 5. The $\tau_{ef,12}$ was found from solving equation (4) for τ_{ef}. The $\mathcal{J}_\nu(\mathrm{T_K})$ was determined from the observed $\mathrm{I}_\nu(140\,\mu\mathrm{m})/\mathrm{I}_\nu(240\,\mu\mathrm{m})$ ratio and the one- and two-component models described in Wall (2006). The uncertainties in τ_{ef}, $\sigma(\tau_{ef})$, were estimated from

$$\sigma(\tau_{ef}) = \frac{\sigma(\eta_{ff})}{1\; -\; \eta_{ff}} \qquad , \tag{73}$$

where $\eta_{ff} \equiv \mathrm{T_R}/\mathcal{J}_\nu(\mathrm{T_K})$. Any attempt to model the points in Figure 5 must consider the large scatter. The points with $\tau_{ef} \lesssim 0.3$ and $I(^{13}\mathrm{CO})/\mathrm{I}(^{12}\mathrm{CO}) \gtrsim 0.3$, for instance, have large vertical scatter due to their large vertical error bars (which are really twice as large as shown, see figure caption). Even if the vertical scatter for these points is not entirely real, the high $I(^{13}\mathrm{CO})/\mathrm{I}(^{12}\mathrm{CO})$ ratios still seem to be likely — i.e., $I(^{13}\mathrm{CO})/\mathrm{I}(^{12}\mathrm{CO}) \sim 0.6$. This combination of high $I(^{13}\mathrm{CO})/\mathrm{I}(^{12}\mathrm{CO})$ and low τ_{ef} is difficult to explain, and is best represented by expression (69). For $x_r = 1/60$, a line ratio of $I(^{13}\mathrm{CO})/\mathrm{I}(^{12}\mathrm{CO}) = 0.6$ requires $\epsilon = 0.12$, roughly consistent with clumps that are hard spheres. Hence these points could be explained by gas with a low filling factor (and, accordingly, low τ_{ef}) and with clumps approximating hard spheres.

On the other hand, the vertical scatter is probably real in the quasi-horizontal band of points that extends from $\tau_{ef} \simeq 0$ to $\tau_{ef} > 1$ for $I(^{13}\mathrm{CO})/\mathrm{I}(^{12}\mathrm{CO}) \lesssim 0.3$ to 0.5. Accordingly, no *single* theoretical curve can adequately model this band; models that have two curves each are plotted in the panels of Figure 5. Before the two-curve models are discussed, the one-curve models are described.

3.3.1. Crude Modeling of $I(^{13}\mathrm{CO})/\mathrm{I}(^{12}\mathrm{CO})$ versus $\tau_{ef,12}$

The data points in Figure 5 are those positions in the Orion A and B molecular clouds for which the peak $\mathrm{T_R}(^{12}\mathrm{CO}\ \mathrm{J}=1\rightarrow 0) > 3\,\sigma$, and $\mathrm{I}_\nu(140\,\mu\mathrm{m})$, $\mathrm{I}_\nu(240\,\mu\mathrm{m})$, and $\mathrm{I}(^{13}\mathrm{CO})$ are all $> 5\,\sigma$ for a total of 372 points (see Wall 2006). One set of $\tau_{ef,12}$ values were derived from one-component models, hereafter $\tau^{(1)}_{ef,12}$, and another from two-component models, hereafter $\tau^{(2)}_{ef,12}$. These models were necessary for estimating the source function, $\mathcal{J}_\nu(\mathrm{T_K})$, from the $140\,\mu$m and $240\,\mu$m DIRBE data (see details in Wall 2006). While both panels of Figure 5 show roughly the same basic trend of $I(^{13}\mathrm{CO})/I(^{12}\mathrm{CO})$ with $\tau_{ef,12}$, the models fit the $I(^{13}\mathrm{CO})/I(^{12}\mathrm{CO})$ versus $\tau^{(1)}_{ef,12}$ plot much better (i.e., upper panel) than the $I(^{13}\mathrm{CO})/I(^{12}\mathrm{CO})$ versus $\tau^{(2)}_{ef,12}$ (i.e., lower panel). This is due to the unrealistically small errors in $\tau^{(2)}_{ef,12}$. But these errors are only the formal errors. While the two-component models for the Orion clouds are better than the one-component models in many ways, they do not seem to adequately estimate the source function, $\mathcal{J}_\nu(\mathrm{T_K})$. This source function depends on a model parameter, c_0, that is not well constrained (unless combined with another parameter). Therefore, when systematic effects are considered, the effective errors in $\tau^{(2)}_{ef,12}$ would be much larger. This must be borne in mind when considering the models described below.

One of the simplest models to consider is that where each model curve is characterized only by a value of a, where a is defined in expression (63). This kind of model represents a picture in which the clump properties are constant (i.e. fixed τ_0, $\Delta\mathrm{v_c}$, $\mathrm{N_c}$) and $\tau_{ef,12}$ and $\tau_{ef,13}$ increase only because the average number of clumps per sightline within each clump velocity width is increasing (i.e., increasing $\frac{N}{\mathrm{N_c}}\frac{\Delta\mathrm{v_c}}{\Delta\mathrm{v}}$), thereby increasing the beam-averaged column density N. In the limit where $\tau_{ef,12}\rightarrow 0$ and $a\tau_{ef,12}\rightarrow 0$, (62) becomes

$$\frac{I(^{13}\mathrm{CO})}{I(^{12}\mathrm{CO})} \rightarrow a \ + \ 0.5\,a\,(1-a)\,\tau_{ef,12} \tag{74}$$

If a is constant, then the line ratio would have a linear dependence on $\tau_{ef,12}$ with slope $0.5a(1-a)$ and intercept a. It turns out that (74) is very good approximation *even when* the limit $\tau_{ef,12}\rightarrow 0$ is *not* valid. For example, (74) yields a result that is within 2% of that of expression (62) even for $\tau_{ef,12}=3$, when $a=0.3$. A sample of clumpy gas with identical clumps, but varying $\tau_{ef,12}$ would have a clear signature in a diagram like Figure 5: a straight line extending to the right from the intercept on the vertical axis with a positive slope, and there would be a well-defined relationship between the slope and the intercept. Figure 5 shows that, for the Orion clouds at least, such a simple signature is not obvious.

Nevertheless, models with one curve were attempted using the orthogonal regression method described in Wall (2006). Models with two curves were also tried. *Neither the one-curve nor the two-curve models were successful.* The two-curve models produced fits with

reduced chi-square values of $\chi^2_\nu = 13.9$ and 24.4 for the $\tau^{(1)}_{ef,12}$ and the $\tau^{(2)}_{ef,12}$, respectively. These are factors of roughly 3 better than for the corresponding one-curve models. The recovered a values for the $\tau^{(1)}_{ef,12}$ are 0.13 and 0.24 from the two-curve models. These are the same for the $\tau^{(2)}_{ef,12}$.

Models that are slightly more complicated are those that assume constant $\mathrm{A}(\tau_{0,12})/\tau_{\mathrm{ef},12}$. The model curves here are characterized by two parameters: the $\mathrm{A}(\tau_{0,12})/\tau_{\mathrm{ef},12}$ ratio, b, and the clump fluffiness, ϵ. This kind of model represents a picture in which the average number of clumps per sightline within each clump velocity width is constant (i.e., constant $\frac{N}{\mathrm{N_c}}\frac{\Delta \mathrm{v_c}}{\Delta \mathrm{v}}$), but $\tau_{0,12}$ and $\tau_{0,13}$ increase, thereby increasing $\tau_{ef,12}$ and $\tau_{ef,13}$. Combining equation (10) with the constant b yields,

$$\tau_{0,12} = b^{1/\epsilon}\ k_A^{-1/\epsilon}\ \tau_{ef,12}^{1/\epsilon} \qquad , \tag{75}$$

where k_A and ϵ are those for $\tau_{0,12} \gg 3$. Substituting (65) into (75) gives

$$a \ = \ b_\tau\, \tau_{ef,12}^{(1-\epsilon)/\epsilon} \qquad , \tag{76}$$

where

$$b_\tau \ \equiv \ x_r\ k_A^{-1/\epsilon}\ b^{\frac{1-\epsilon}{\epsilon}} \qquad . \tag{77}$$

Substituting (76) into (62) results in

$$\frac{I(^{13}\mathrm{CO})}{I(^{12}\mathrm{CO})} \ \simeq \ \frac{1 \ - \ exp(-b_\tau \tau_{ef,12}^{1/\epsilon})}{1 \ - \ exp(-\tau_{ef,12})} \qquad . \tag{78}$$

The above expression results in $\tau_{ef,13}$ growing very rapidly for small ϵ. This growth cannot continue unchecked and must slow when a reaches its saturation value, given by expression (66). Consequently, in this limit,

$$\frac{I(^{13}\mathrm{CO})}{I(^{12}\mathrm{CO})} \ \simeq \ \frac{1 \ - \ exp(-x_r^\epsilon \tau_{ef,12})}{1 \ - \ exp(-\tau_{ef,12})} \qquad . \tag{79}$$

Each model curve combines (78) and (79): the minimum of the two $I(^{13}\mathrm{CO})/I(^{12}\mathrm{CO})$ values for each $\tau_{ef,12}$ is used. As a result, the $I(^{13}\mathrm{CO})/I(^{12}\mathrm{CO})$ versus $\tau_{ef,12}$ curves are from expression (78) for lower $\tau_{ef,12}$ and expression (79) for higher $\tau_{ef,12}$. This produces an abrupt transition at some intermediate $\tau_{ef,12}$ value (see curves in Figure 5). This abrupt transition is not real and only appears in these model curves because the smooth transition of $\mathrm{A}(\tau_0)$ from optically thin to optically thick behavior (i.e., for $1 \lesssim \tau_0 \lesssim 3$) has not been considered here. Nevertheless, these intermediate τ_0 values represent only a small portion of the curves. Accordingly, the abrupt transitions in the curves only introduce small inaccuracies into the final results.

Models with one curve and models with two curves were fitted, each fit optimizing b_τ and ϵ. The best fits of the one-curve models had reduced chi-square values that were factors of 2.1 to 2.5 worse than those of the two-curve models. The data points in Figure 5 are not entirely independent, so the effective number of degrees of freedom is about a factor of 9 lower than the number of points (see discussion of this in Wall 2006), or about 40. Therefore, the F-test states that the two-curve models are better than the one-curve models at a 97.5% confidence level. The resultant parameter and reduced chi-square values are given in Figure 5. Even if the two-curve models are superior to the one-curve models, the fits of the former to the data are not impressive. Nonetheless, the fit to the $\tau_{ef,12}^{(1)}$ is not too bad ($\chi_\nu^2 \simeq 4$) considering the vertical spread in the points, even in the quasi-horizontal band. The fit to the $\tau_{ef,12}^{(2)}$ is considerably worse, but then this is due to the unrealistically small horizontal error bars. These two-curve models (where each curve uses two parameters) are better than the previous simpler two-curve models (where each curve uses one parameter) at the 95% confidence level or better, according to the F-test. For $\tau_{ef,12}$ beyond some threshold, the constant a models (with one parameter per curve) superficially resemble the constant $\mathrm{A}(\tau_{0,12})/\tau_{\mathrm{ef},12}$ models (with two parameters per curve), because the latter have constant a (i.e., $a = x_r^\epsilon$) in this $\tau_{ef,12}$ range. Consequently, the latter being significantly better than the former is because the latter models have a rapid non-linear rise at smaller $\tau_{ef,12}$ where the majority of the points lie.

The systematic uncertainties in the resultant parameter values were found by adopting systematic errors of 30% for $I(^{13}\mathrm{CO})/I(^{12}\mathrm{CO})$, η_{ff}, and x_r. Specifically, 0.7 and 1.3 were each multiplied by one of these quantities and the models were refit, a total of 6 refits. The minimum and maximum b_τ and ϵ were chosen from these refits as measures of the uncertainties. The uncertainty in b_τ is about a factor of 2 and for ϵ about 30%. Expression (77) and $\epsilon \sim 0.3$ imply that the systematic uncertainty in b is roughly a factor of $\sqrt{2}$ or about 40%. Given that $1/b$ is in reality $\frac{N}{\mathrm{N_c}}\frac{\Delta \mathrm{v_c}}{\Delta \mathrm{v}}$, this latter also has a systematic uncertainty of about 40%.

With these systematic uncertainties in mind, the ϵ values given in Figure 5 for the upper panel are consistent with those in the lower panel. The b_τ values given in Figure 5 are significantly different between the two panels. Nonetheless, the changes in ϵ from one panel to the other conspire with the b_τ values to produce b values that are much closer together (in a logarithmic sense). Solving (77) for b, adopting $k_A = 1.5$, and using the b_τ values in Figure 5 results in

$$\frac{N}{\mathrm{N_c}}\frac{\Delta \mathrm{v_c}}{\Delta \mathrm{v}} = 1 \times 10^{-2} \; and \; 6 \times 10^{-2} \quad , \; for \; \tau_{ef,12}^{(1)}, \tag{80}$$

$$= 2 \times 10^{-2} \; and \; 8 \times 10^{-2} \quad , \; for \; \tau_{ef,12}^{(2)}. \tag{81}$$

Considering that the effective spatial resolution of the observations was slightly less than

1° (or a linear resolution of 8 pc for the adopted distance of 450 pc), these numbers are reasonable. The fluffiness values are more succintly summarized as roughly the following: $\epsilon \simeq 0.3 \pm 0.1$. This range is consistent with that found in Section 3.2.1.

One concern raised by the modeling here is that many positions seem to have non-negligible optical depths in the ^{13}CO J = 1 → 0 line. The modeling of physical conditions by Wall (2006) required ^{13}CO J = 1 → 0 to be optically thin. Examination of the upper panel of Figure 5 suggests that the majority of points are not towards optically thick sightlines in ^{13}CO J = 1 → 0. Most of the points are associated with the curve with the lower b_τ value and, hence, lower A($\tau_{0,12}$) values. The majority of these points are at lower $\tau_{ef,12}$ than occurs for the abrupt transition at $\tau_{ef,12} = 0.34$. It is easy to compute that $\tau_{0,13} \simeq 2$ at this transition. Accordingly, the majority of points have $\tau_{0,13} < 2$. Given that $\tau_{0,12} \propto \tau_{ef,12}^{1/\epsilon}$ (cf. equation 75), the $\tau_{0,13}$ is very strong function of $\tau_{ef,12}$ and drops rapidly with $\tau_{ef,12}$ decreasing below the transition point. Therefore, the majority of points do not represent sightlines optically thick in ^{13}CO J = 1 → 0, although some important minority of points may indeed represent such sightlines.

In summary, the modeling of the $I(^{13}\mathrm{CO})/\mathrm{I}(^{12}\mathrm{CO})$ versus $\tau_{ef,12}$ diagram did not produce exceptionally good fits, but does strongly favor one scenario over another. Specifically, it favors the case of growing clump optical depth as the column density increases from position to position, rather than the case of a growing number of clumps per sightline. The model fits suggest that the average number of clumps per sightline per clump velocity width is a $few \times 10^{-2}$ and the fluffiness is 0.3 ± 0.1, consistent with that expected for the observed X_f value (see Section 3.2.1).

4. Discussion

The Orion clouds have been used as a test bed for the ideas developed here. More general implications are examined in this section.

4.1. Comparisons with Previous Work

Much of the previous work on the X-factor was based in one way or another on DSS86. Two examples of this are Sakamoto (1996) and Weiss et al. (2001), which examined the relationship between X_f and physical parameters — i.e., n(H_2) and T_K. The former used LVG models to explore the behaviour the X-factor under non-LTE conditions. The latter used observational data to estimate the dependence of X_f on density and temperature.

Sakamoto (1996) has the advantage that it deals with non-LTE conditions, but has the disadvantage that it does not consider radiative transfer through a clumpy cloud. Obviously, the advantage and disadvantage of the current paper complement those of Sakamoto (1996). Accordingly, a treatment that combines non-LTE conditions with radiative transfer in a clumpy medium would be desirable, but is beyond the scope of the current work.

Any attempt to at least roughly estimate the properties of such a combined treatment must compensate for some minor errors found in Sakamoto (1996).

- The expression for the virial mass, equation (5) of that paper, is missing a factor of $\frac{1}{2}$. This can be verified for the uniform density case by comparing with the derivation given in Section 2.2 of the current paper. This can also be verified for the $\rho(r) \propto r^{-1}$ case by comparing with the expressions given in Maloney (1990). Both of these comparisons confirm the absence of the factor $\frac{1}{2}$ in equation (5) of Sakamoto (1996). So equations using the parameter k_3 must use $\frac{k_3}{2}$ in place of k_3. Consequently, the numerical values of X_f computed from equation (7) of that paper must be corrected downward by a factor of $\sqrt{2}$.

- The claim that X_f is independent of T_K in the optically thin (i.e. $\tau(^{12}\mathrm{CO\ J} = 1 \rightarrow 0) \ll 1$), thermalized limit is incorrect. This claim and its explanation are given in point #2 (which contains expression 11) of Sakamoto (1996). Section 3.1.2 shows that such a claim is false. A very simple physical argument makes it obvious that X_f *must* depend on T_K in the optically thin, LTE limit: as T_K increases in the high-T_K, LTE limit the CO molecules populate more and more of the upper-J levels, thereby decreasing the column density of CO in the $J = 1$ level. If the $J = 1 \rightarrow 0$ line is optically thin, then $I(CO)$ decreases for fixed total $N(H_2)$, resulting in X_f increasing with increasing T_K (cf. Section 3.1.2). The panels of Figure 3 of Sakamoto (1996) do indeed show that X_f varies by less than factor of about 2 (from smallest to largest) over the range $T_K = 10$ to 100 K for CO abundances less than about 10^{-5}. However, contrary to point #2 of Sakamoto (1996), even $n(H_2)$ as high as $10^4\,\mathrm{cm}^{-3}$ does *not* thermalize the ^{12}CO J = 1 → 0 line when it is optically thin — LTE still does *not* apply. Given that the critical density of the ^{12}CO J = 1 → 0 line is $\sim 3 \times 10^3\ H_2\,\mathrm{cm}^{-3}$, it is natural to assume that densities corresponding to the lower two panels of Figure 3 of that paper — i.e., $3 \times 10^3\ H_2\,\mathrm{cm}^{-3}$ and $1 \times 10^4\ H_2\,\mathrm{cm}^{-3}$ — are sufficient to bring the J = 1 → 0 line of CO close to LTE. The problem is that critical densities are normally computed as though a given atom or molecule is just a two-level system. For the CO molecule, there are many rotational levels *and* the radiative decay rates increase very rapidly — roughly like J^3 — as one moves up the rotational ladder. When the CO J = 1 → 0 line is optically thin, radiative trapping effects are minimized and the CO molecules pile up mostly in the $J = 0$ and $J = 1$ states, often resulting in superthermal $J = 1/J = 0$

population ratios (i.e., the excitation temperature of the J = 1 → 0 transition is greater than T_K) or even population inversions, because of the higher levels with large radiative decay rates. Therefore, non-LTE effects play a role in the behavior of the J = 1 → 0 line even at densities around 3×10^3 $H_2\,cm^{-3}$ (provided that the J = 1 → 0 line is optically thin). For the specific cases of the densities considered in Figure 3 of Sakamoto (1996) and for CO abundances $\lesssim 10^{-5}$, the increasing T_K populates the $J = 1$ level from the $J = 0$ level at an increasing rate, but also *de*populates the $J = 1$ level to the higher-J levels at an increasing and roughly comparable rate. Accordingly, the column density of CO molecules in the $J = 1$ level stays roughly constant. Given that the CO J = 1 → 0 line is optically thin for these abundances, the observed line brightness is directly proportional to the column density in the $J = 1$ (and *not* the $J = 0$) state, resulting in roughly constant line brightness and, ergo, roughly constant X_f. Therefore, expression (11) of Sakamoto (1996), which states that $X_f \propto X(CO)^{-1}$ with no dependence on T_K nor $n(H_2)$, is approximately correct. And again, this is only in this particular *non*-LTE case. In the LTE limit when CO J = 1 → 0 is optically thin, the dependence of X_f on T_K is as given in Section 3.1.2.

- The statement that the observed spectral profiles of the CO J = 1 → 0 line place an upper limit on its opacity is erroneous, and is at odds with the clumpy cloud picture presented in Figure 1 of Sakamoto (1996). That paper states that the ^{12}CO J = 1 → 0 line cannot be very optically thick or its profiles would be flat-topped. For a given volume of gas with more or less uniform density, that would be true; increasing the optical depth would saturate the line core before it would do so in the line wings. But this is *not* necessarily the case in a clumpy cloud. The optical depth of the ^{12}CO J = 1 → 0 line within each clump can increase without bound and, as long as the filling factor within each velocity interval within the line profile is sufficiently small, the observed line profile can still be Gaussian (e.g., see equation 7 of the current paper). This point is important for avoiding unrealistically low upper limits on the optical depth of the ^{12}CO J = 1 → 0 line.

With these caveats in mind, a relatively *simple* treatment of clumpy clouds that includes both radiative transfer and non-LTE effects can be developed. This will be particularly useful for developing insights into the emission of high-dipole molecules like CS, whose transitions are farther from LTE than those of CO.

In the meantime, a rough estimate of the behavior of X_f in the non-LTE limit is possible from combining the results of Sakamoto (1996) with the current work. For example, in the high-density, metal-rich case Sakamoto (1996) finds that $X_f \propto n(H_2)^{1/2}\ T_K^{-1}$. In the current paper, this can correspond to any of the cases in Sections 3.1.3, 3.1.4, or 3.1.5. All of these cases show a weaker dependence of X_f on $n(H_2)$ and on T_K. The side-on Gaussian cylinder,

for instance, requires roughly the following: $X_f \propto C_T\, \mathrm{T_K^{-0.6}}\, \mathrm{n(H_2)^{0.4}}$. Therefore, as has been noted previously, the radiative transfer through a clumpy medium has the effect of softening the dependence of the X-factor on density and kinetic temperature. Two other cases are discussed in that paper. The case of intermediate density (i.e. $\sim 3 \times 10^3\ H_2\,\mathrm{cm^{-3}}$) and low metallicity shows no dependence of X_f on $\mathrm{n(H_2)}$ nor $\mathrm{T_K}$. Including radiative transfer through a clumpy medium is unlikely to change this. The case of low density (i.e. $\lesssim 3 \times 10^2\ H_2\,\mathrm{cm^{-3}}$) and low metallicity has the following behavior: $X_f \propto \mathrm{n(H_2)^{-1}\ T_K^{-1/2}\ X(CO)^{-1}}$. Combining this with radiative transfer in clump medium will yield $X_f \propto \mathrm{n(H_2)^{-\delta_1}\ T_K^{-\delta_2}\ X(CO)^{-1}}$, where $\delta_1 < 1$ and $\delta_2 < \frac{1}{2}$. Very crude guesses would be that $\delta_1 \sim 0.6$ and $\delta_2 \sim 0.4$. Something else worth considering is that in low-metallicity clouds, such as those in irregular galaxies, the CO abundance *within the CO-emitting region within each cloud* is close that in our Galaxy (see Israel 1997a, 2000, and references therein). Consequently, the behavior of the X-factor in such clouds may be closer to that described in Sections 3.1 and 3.2.2 than assuming optically thin, non-LTE ^{12}CO J = 1 → 0 emission.

Weiss et al. (2001) observationally tested the dependence of the X-factor on density and temperature. They observed the central region of the galaxy M 82 in the lower-J lines of ^{12}CO, ^{13}CO, and C^{18}O to constrain estimates of the molecular gas density and temperature. Using their estimates of $\mathrm{N(H_2)}$, $\mathrm{n(H_2)}$, and $\mathrm{T_K}$, they plotted $\mathrm{N(H_2)/I(CO)}$ versus $\mathrm{n(H_2)^{1/2}\ T_K^{-1}}$ for the observed positions and found a roughly linear relationship (see their Figure 11). Determining the densities and kinetic temperatures from line ratios with sufficient accuracy is fraught with difficulties; Weiss et al. (2001) do not include the error bars in this plot and it is easy to show that the total horizontal uncertainty of each plotted point (i.e. from smallest to largest value for each point) is roughly 1/3 the horizontal extent of the entire figure. Accordingly, a large range of dependences on temperature and density are *not* ruled out. In general, such observational tests of the behavior of the X-factor are very uncertain.

4.2. The Dependence of $\mathrm{X_f}$ on CO Abundance

The molecular gas in low-metallicity irregular galaxies has very low CO abundance over large volumes and has roughly the Galactic abundance level in small internal regions within the molecular clouds (see Israel 1997a, 2000, and references therein). Based on this picture, Section 3.2.2 discussed the dependence of the X-factor on the CO abundance and found that $X_f \propto X(CO)^{-\theta}$, where θ can be anywhere from 0.5 to 1.0. Israel (2000) examined the dependence of X_f on the metallicity in a sample of Magellanic irregular galaxies and had the result that $X_f \propto X(O)^{-2.5}$. If the CO abundance is largely determined by the O abundance,

then $X_f \propto X(CO)^{-2.5}$. If, however, the CO abundance is largely determined by the C abundance and, given that $X(C) \propto X(O)^{1.7}$ (Israel 2000, and references therein), $X_f \propto X(CO)^{-1.5}$. Instead, the CO abundance might be strongly affected by the photodissociation rate and would be inversely proportional to that rate. Given that the photodissociation rate is proportional to $X(O)^{-3}$ (Israel 1997a, and references therein), this results in $X_f \propto X(CO)^{-0.8}$. Hence, there are three possibilities:

$$X_f \propto X(CO)^{-2.5} \quad , \tag{82}$$

or

$$X_f \propto X(CO)^{-1.7} \quad , \tag{83}$$

or

$$X_f \propto X(CO)^{-0.8} \quad . \tag{84}$$

Expressions (82) and (83) represent dependences that are steeper than one would expect even in the optically thin case (i.e., $X_f \propto X(CO)^{-1.0}$). Having such a steep dependence would require that other physical parameters like density and kinetic temperature also depend on the CO abundance. When the volume-averaged $X(CO)$ is small, the interstellar radiation field that reaches the CO-containing gas is strong, resulting in high gas temperatures. This would produce a smaller X-factor at small $X(CO)$ (based on the expressions of Section 3.1) and the dependence of X_f on $X(CO)$ would be less steep. On the other hand, the strong interstellar radiation field would preferentially photodissociate the low-density molecular gas, leaving the high-density gas. The low X(CO) would be associated with higher densities and higher densities mean higher X_f (see Section 3.1). Higher X_f at low $X(CO)$ means a steeper dependence of X_f on $X(CO)$. Consequently, the effects of the higher temperature would compete against the effects of higher density, making it uncertain if such steep relations are possible or even likely. The most likely dependence is that of expression (84). And this is consistent with the range found in Section 3.2.2.

4.3. The Relationship between X_f and ^{13}CO J = 1 → 0/^{12}CO J = 1 → 0

That a relationship exists between the X-factor and the ^{13}CO J = 1 → 0/^{12}CO J = 1 → 0 line ratio is not new and has been used to determine whether the X-factor varies spatially. For example, Rickard & Blitz (1985) and Paglione et al. (2001) observed the J = 1 → 0 lines of ^{12}CO and ^{13}CO in external galaxies and found that the $I(^{13}\mathrm{CO})/\mathrm{I}(^{12}\mathrm{CO})$ ratio was significantly different in the nuclear regions from that in the disks. This is evidence that the X-factor in galactic nuclei is also different from that in the disks. Based on the current work, how do changes in $I(^{13}\mathrm{CO})/\mathrm{I}(^{12}\mathrm{CO})$ relate to changes in X_f? This can be assessed by

using an equation analogous to (34) for ^{13}CO. Equation (34) assumes that ^{12}CO J = 1 → 0 is optically thin (i.e., $\tau_{0,12} \lesssim 1$). Since ^{13}CO J = 1 → 0 is likely to be optically thin on the scales of many parsecs, the appropriate expression is

$$X_f = C_T \; k_\tau^{-1} \, \mathrm{T_K^{\gamma-1}} \; x_r^{-1} \; \frac{I(^{13}\mathrm{CO})}{I(^{12}\mathrm{CO})} \quad . \tag{85}$$

The X_f and k_τ are those for ^{12}CO and not for ^{13}CO; accordingly the $I(^{13}\mathrm{CO})/I(^{12}\mathrm{CO})$ and x_r^{-1} are necessary to correct for those, respectively. Notice that when ^{12}CO J = 1 → 0 is optically thin as well ($\tau_{0,12} \lesssim 1$), the line ratio is x_r (see equation 67) and equation (85) reduces to (34), as required. When $\tau_{0,12} > 3$, equation (68) for $I(^{13}\mathrm{CO})/I(^{12}\mathrm{CO})$ applies; when this is substituted into expression (85), equation (28) for X_f is recovered, also as required. Therefore, the X-factor is proportional to the ^{13}CO J = 1 → 0/^{12}CO J = 1 → 0 line ratio.

However, the situation is not quite that simple. Given that the X-factor is also proportional to $\mathrm{T_K^{\gamma-1}}$ $\mathrm{x_r^{-1}}$, determining spatial variations in X_f from one observed position to another can be obscured by unknown spatial variations in $\mathrm{T_K}$ and x_r. For example, X_f may be varying spatially while $I(^{13}\mathrm{CO})/I(^{12}\mathrm{CO})$ remains constant and vice versa. One way to estimate the dependence between X_f and $I(^{13}\mathrm{CO})/I(^{12}\mathrm{CO})$ when there are also spatial variations in $\mathrm{T_K}$ is to assume some kind of correlation between the $\mathrm{T_K}$ and $\mathrm{n(H_2)}$. For example, $\mathrm{T_K} \propto \mathrm{n(H_2)}^w$. One of the limiting forms of equation (62) in Section 3.3 — i.e., equations (67) to (71) — is useful here: the most appropriate of these for the bulk of molecular clouds is equation (68). Using that expression along with that of (22) and substituting into (85) results in the following possible dependence:

$$X_f \propto \left[\frac{I(^{13}\mathrm{CO})}{I(^{12}\mathrm{CO})} \right]^u \quad , \tag{86}$$

where

$$u \equiv \frac{\frac{1}{2}(1-\epsilon) \; + \; w(\gamma\epsilon - 1.32)}{(\frac{1}{2} - \gamma w)(1-\epsilon)} \qquad for \; \mathrm{T_K} = 10 \; to \; 20 \, K. \tag{87}$$

In the high-$\mathrm{T_K}$ limit, the "1.32" is replaced with "1.00". Of particular interest is pressure equilibrium, where $w = -1$. For $\epsilon = 0.2$ to 0.4 (see Section 3.3.1), $u = 0.8$ to 0.7 when $\mathrm{T_K} = 10$ to 20 K. In the high-$\mathrm{T_K}$ limit, the corresponding range in u is 0.5 to 0.3. Hence, if there are spatial variations of the molecular gas kinetic temperature from one observed position to another, and pressure equilibrium applies, the apparent correlation between the X-factor and the ^{13}CO J = 1 → 0/^{12}CO J = 1 → 0 line ratio could be weak.

There are, of course, additional complications. One is that equation (85) assumes LTE; non-LTE effects might be important in some sources and this would require an explicit density

dependence in the relationship between X_f and $I(^{13}\mathrm{CO})/I(^{12}\mathrm{CO})$. Another complication is that the ^{13}CO J = 1 → 0/^{12}CO J = 1 → 0 ratio may be saturated (see equation 69) toward some positions in some sources. (See Section 4.4 for more details.)

Nonetheless, if a large number of positions are sampled in a source where the kinetic temperature is roughly constant, such as in a galactic disk on large scales, then there could be an approximately linear correlation between the X-factor and the ^{13}CO J = 1 → 0/^{12}CO J = 1 → 0 line ratio.

4.4. Determining ϵ from ^{13}CO J = 1 → 0/^{12}CO J = 1 → 0

One way to constrain estimates of X_f is to model the data in the $I(^{13}\mathrm{CO})/I(^{12}\mathrm{CO})$ versus $\tau_{ef,12}$ plot, as was done in Section 3.3.1, thereby estimating ϵ and possibly other parameters. However, this method has the considerable drawback that it requires some measure of the source function. Wall (2006) did this for the Orion clouds by using the far-IR continuum data. The Orion clouds are 10° to 20° out of the Galactic plane, meaning that the origin of the continuum emission was unambiguous. Due to the lack of velocity information, continuum data is not very useful for isolating the emission of individual clouds along lines of sight through the Galactic plane. Therefore, determination of the source function of such clouds with continuum data would be very difficult, if possible at all.

Another simpler approach is to use the histogram of $I(^{13}\mathrm{CO})/I(^{12}\mathrm{CO})$ values. One such histogram for the Orion clouds is shown in Figure 6. It shows a prominent peak between ^{13}CO J = 1 → 0/^{12}CO J = 1 → 0 line ratios of about 0.1 and 0.3 with a maximum at about 0.2. The left edge of this peak roughly corresponds to the self-shielding limit for molecules — i.e., $A_v \simeq 1\,mag$. The ^{13}CO J = 1 → 0/^{12}CO J = 1 → 0 line ratio approximately correlates with the gas column density. For the Orion clouds, $I(^{13}\mathrm{CO})/I(^{12}\mathrm{CO}) = 0.1$ corresponds to total hydrogen-nuclei column density, N(H I+2H$_2$), of 0.7 to 1.5×10^{21} cm^{-2} or about $A_v = 0.5$ to 1.0 magnitudes. (Note that this range applies regardless of whether the column densities were derived from one- or two-component models and regardless of imposed restrictions on the signal-to-noise ratio; cf. Wall (2006).) The right edge of the peak can be interpreted by inspecting the panels of Figure 5; the value of $I(^{13}\mathrm{CO})/I(^{12}\mathrm{CO})$ corresponding to the right edge of the histogram peak corresponds to where the model curves are linear — i.e., where the ^{13}CO J = 1 → 0/^{12}CO J = 1 → 0 ratio saturates. According to equation (69), this is x_r^ϵ. If r_e is the ^{13}CO J = 1 → 0/^{12}CO J = 1 → 0 ratio at the right edge of the peak, then ϵ is given by

$$\epsilon = \frac{ln(r_e)}{ln(x_r)} \quad . \tag{88}$$

If the ^{13}CO/^{12}CO abundance ratio, x_r, is the same in the Orion clouds as in the inner Galactic disk, then the fluffiness, ϵ, of the molecular cloud clumps are also the same. For $x_r = 1/60$, $\epsilon = 0.29$. This is consistent with model results of Section 3.3.1. However, the observations of Langer & Penzias (1990) show that x_r in the inner galaxy systematic varies with Galactocentric radius by a factor of about 2 from the center to the solar circle. Because of the logarithmic dependence on x_r the affect on ϵ is relatively small: $\epsilon = 0.29$ to 0.35 from the solar circle to the inner Galaxy. And these values are still consistent with the model results of Section 3.3.1, even though those results only apply to the Orion clouds. Whether the X-factor is the same in the Orion clouds as in the inner Galaxy also depends on the typical densities and temperatures in the molecular cloud clumps in the two. If they are the same on average, then Figure 4 provides a crude estimate of the X-factor: $X_f \simeq 1.2$ to $2.2\,X_{20}$ depending on the curve and ϵ value (i.e. 0.29 or 0.35) used.

Of course, not all positions have ^{13}CO J = 1 $\rightarrow$ 0/^{12}CO J = 1 $\rightarrow$ 0 ratios between 0.1 and 0.3. A few are much larger, up to 0.95. Line ratios this high can only occur if either ϵ is smaller than the value(s) that occurs for the positions in the peak, as discussed in Section 3.3, or if $\tau_{ef,13}$ is large. It is possible that there is a distribution of ϵ values in clouds. This distribution would probably have to be sharply peaked to permit the peak in the histogram to have reasonably defined right edge (e.g., the peak from its maximum down to some poorly defined zero level on the right side has ^{13}CO/^{12}CO line ratios from about 0.2 to about 0.45). To have a rough guess at what such a distribution might look like, it could be *assumed* that *all* the observed positions have saturated ^{13}CO J = 1 $\rightarrow$ 0/^{12}CO J = 1 $\rightarrow$ 0 ratios. Then equation (88) with all the observed line ratios used in place of r_e will give a histogram that would contain such a distribution within its boundaries. Adopting symmetry about the maximum of the ϵ distribution as a working assumption implies that there is an excess in the number of positions with high ϵ values ($\epsilon > 0.3$), which corresponds to an excess in the number of positions with low ^{13}CO J = 1 $\rightarrow$ 0/^{12}CO J = 1 $\rightarrow$ 0 ratios (< 0.3). This excess supports the interpretation that these low line ratios are *un*saturated as expected, and do not represent part of this hypothetical distribution of ϵ values.

Comprehending exactly what limits the range of ϵ values in a molecular cloud, cloud complex, or galaxy is key to understanding the X-factor. It is also key to comprehending the narrow range of ^{13}CO J = 1 $\rightarrow$ 0/^{12}CO J = 1 $\rightarrow$ 0 ratios. Therefore, understanding the narrow range of ^{13}CO J = 1 $\rightarrow$ 0/^{12}CO J = 1 $\rightarrow$ 0 ratios is key to understanding the X-factor. These two are linked. Even if the formulation for the X-factor proposed in this paper were incorrect, even if it were not possible to clearly define a quantity like ϵ in real molecular clouds, the connection between the restricted range of ^{13}CO J = 1 $\rightarrow$ 0/^{12}CO J = 1 $\rightarrow$ 0 ratios and the X-factor would exist independently.

4.5. Clump/Interclump

Real molecular clouds (like Orion and Rosette) have about $\frac{3}{4}$ of their mass and $\frac{1}{10}$ of their volume in the form of clumps, and the remainder in an interclump medium (see, e.g., Ostriker 1999; Williams et al. 1995; Bally et al. 1987). Adopting θ_H as the former quantity and f_H as the latter (as done in Ostriker 1999), then $r_M = \theta_H^{-1} - 1 = \frac{1}{3}$ and $r_\sigma = [(1 - f_H)/f_H]^{\frac{1}{3}} \simeq 2$. For $r_M < 1$, we need $r_\sigma \gg r_M^{\frac{1}{3}}$ for the r_σ large limit to apply; since $2 \gg 0.7$ is more or less valid, X_f would be increased by about $(1 + r_M)^{0.5(1-\epsilon)}$, which is an increase of less than 15%. Therefore, if most molecular clouds are like the examples given here, then the interclump medium will have a small effect on the X-factor. This is especially true if this interclump gas is mostly atomic (e.g., see Williams et al. 1995, and references therein).

4.6. Radial Density Profiles

The density dependence on radius in dark clouds or in the clumps (or cores) of clouds is often $\rho \propto r^{-\alpha}$, where α is 2 or nearly so (e.g., Harvey et al. 2001; Tachihara et al. 2000; Lada et al. 1999; Alves et al. 1998; Henriksen et al. 1997; Williams et al. 1995). As discussed in Appendices C and D (see Sections C.4 and D.3.1) and Section 3.1.5, a $\rho \propto r^{-2}$ dependence requires specifying an outer radius, r_1, to keep the total mass finite and an inner radius to the r^{-2} region, r_0, to keep the density finite. Also, the ratio r_1/r_0 determines the fluffiness, ϵ, of the clump. And estimates of ϵ can be constrained by observations X_f or of the ^{13}CO J = 1 $\rightarrow$ 0/^{12}CO J = 1 $\rightarrow$ 0 intensity ratio (cf. Sections 3.3 and 3.3.1). Accordingly, the observations can constrain the r_1/r_0 ratio (assuming that the bulk of the ^{12}CO J = 1 $\rightarrow$ 0 emission originates in structures with $\rho \propto r^{-2}$). The histogram of $I(^{13}\mathrm{CO\ J} = 1 \rightarrow 0)/\mathrm{I}(^{12}\mathrm{CO\ J} = 1 \rightarrow 0)$ values suggests that $\epsilon \simeq 0.3$, the same as that found in the modeling in Section 3.3.1 for the Orion clouds. If the range of ϵ values found from that modeling are relevant to much of the Galactic disk, then $\epsilon = 0.2$ to 0.4. If the clumps are spherical, then r_1/r_0 would be in the range 2 to 9. If the clumps are cylindrical filaments viewed side-on, then r_1/r_0 would be from 4 to 42. (End-on cylindrical filaments would have a much more restricted range of r_1/r_0, but these need not be considered here. It is much more likely to view high-aspect cylinders close to side-on than close to end-on. Hence, the side-on cylinders would probably dominate the emission from most clouds.)

Observations suggest r_1/r_0 ratios that are consistent with the ϵ values specified above. Specifically, r_1/r_0 is found to be from about 4 to 15 (e.g., Harvey et al. 2001; Tachihara et al. 2000; Lada et al. 1999; Alves et al. 1998; Henriksen et al. 1997; Williams et al. 1995). It must be borne in mind that many of these observed r_1/r_0 values are merely lower limits due

to limitations in spatial resolution, which place upper limits on r_0 — the inner radius of the $\rho \propto r^{-2}$ region within each clump.

4.7. Molecular Clouds in Some Specific Regions

4.7.1. Rosette and Orion

The literature has papers with lists of clump temperatures, masses, and dimensions for certain molecular clouds. Two examples are Williams et al. (1995) for the clumps in the Rosette Molecular Cloud (RMC) and Nagahama et al. (1998) for the clumps in the Orion A cloud. With these clump properties, rough estimates of X_f can be made.

For the RMC, Table 2 of Williams et al. (1995) provides the necessary information, after adjusting the adopted $N(H_2)/N(^{13}\mathrm{CO})$ ratio. Williams et al. (1995) adopt $N(H_2)/N(^{13}\mathrm{CO}) = 5\times10^5$, which may be quite reasonable, especially for the ρ Oph cloud (see Bertoldi & McKee 1992, and references therein). Frerking et al. (1982) find an abundance of 8×10^{-5} for ^{12}CO and Langer & Penzias (1990) find 1/60 for $X(^{13}\mathrm{CO})/\mathrm{X}(^{12}\mathrm{CO})$ in the Galactic disk approximately at the solar circle (and out to Orion). These imply $N(H_2)/N(^{13}\mathrm{CO}) \simeq 7.8\times10^5$. Adopting this abundance ratio implies 55% higher clump masses (see M_{LTE} in their Table 2) and an observationally determined X_f that is also 55% higher or $1.7\,X_{20}$, which is about the value expected for molecular clouds in the Galactic disk. At the very least, this higher $N(H_2)/N(^{13}\mathrm{CO})$ ratio is the same as that adopted for the Orion clouds.

For the RMC clumps, Williams et al. (1995) find $\frac{r_1}{r_0} = 5$ (cf. their Figure 22), which may only be a lower limit due to resolution constraints. If taken at face value, this means that $\epsilon = 0.30$ and $k_A = 1.80$. Section C.4 of Appendix C computes the specific expression for X_f for those parameter values — expression (C43). The densities of the clumps were determined by assuming spherical clumps with the masses (i.e., M_{LTE} increased by 55%) and radii (i.e., ΔR) as listed in Table 2 of Williams et al. (1995). The densities and temperatures of the clumps either inferred from, or listed in, Table 2 of that paper will then give the X_f value corresponding to each clump — that is, the X_f value that would result in a hypothetical cloud filled with clumps identical to this one. The median of these X_f values is then taken as an estimate of the X_f of the cloud. (The mean is not used because it is influenced by extreme outliers. A better way to do this is to develop a formulation that includes clumps with a distribution of densities and temperatures, but that is beyond the scope of the current paper.) Here the X_f values use the density as averaged over the entire clump volume (i.e. equation C46) and is more appropriate in this case (see Williams et al. 1994, 1995). The X_f values found for the RMC range from about 2 to $10\,X_{20}$ with a median of $3.4\,X_{20}$. This

median is double that determined observationally (and adjusted to the new $N(H_2)/N(^{13}\mathrm{CO})$ ratio): $1.7\,X_{20}$. This suggests that the formulation is moderately successful, for the RMC at least, because it estimates the X-factor to within a factor of 2.

It may be possible, however, to improve the agreement between the model X_f and that observed. At least some of the temperatures listed in Table 2 of Williams et al. (1995) are probably underestimated. These temperatures are excitation temperatures of the J = $1 \rightarrow 0$ transition of ^{12}CO that were computed from the peak radiation temperature, T_R, of that line. In practical terms, this excitation temperature is about the same as the kinetic temperature, given that the ^{12}CO J = $1 \rightarrow 0$ line is easily thermalized (and Williams et al. (1995) themselves implicitly assumed equivalence between the two temperatures when they determined column densities of *all* the molecular gas and *not just* the column densities in the $J = 1$ state of ^{13}CO.) This method of determining excitation temperatures or, roughly equivalently in this case, kinetic temperatures implicitly assumes that the emitting gas fills the beam within each velocity interval of the line profile, especially at the line peak. Despite the scatter, the inferred clump temperatures have a definite positive correlation with the clump diameters; the Spearman rank-order correlation test places a 99.998% confidence level on the correlation (or the significance of the null proposition of no correlation is $\sim 2 \times 10^{-5}$). In contrast, in the Orion A cloud, where the kinetic (excitation) temperatures were also estimated using the peak T_R of the ^{12}CO J = $1 \rightarrow 0$ line (see Nagahama et al. 1998), the Spearman test places only a 40% to 60% confidence on the correlation (depending on whether the clump size used was filament length or filament diameter). Accordingly, any correlation between clump size and inferred clump temperature in Orion A is either weak or non-existent. (Although it should be mentioned that these temperatures are not entirely reliable either, given that certain values are frequently repeated.) The Orion clumps have linear sizes (i.e., in parsecs) factors of 3 to 5 larger than those of the RMC and the Orion clouds are nearly a factor of 4 closer than the RMC. The interpretation of why the RMC clumps clearly show a correlation between size and inferred temperature while the Orion clumps do not is then fairly straightforward: the smaller clumps in the RMC are not being resolved in the velocity interval at the line peak, while the larger clumps are better resolved. Hence it is likely that at least some of the inferred clump temperatures for the RMC are too low. These inferred temperatures range from about 5 to 31 K with a median of about 9 K. For Orion A, the range is 13 to 37 K with a median of about 18 K, which is the dominant dust temperature of the Orion clouds (see Wall et al. 1996; Wall 2006) and even of the Galactic plane clouds (Sodroski et al. 1994). Both Orion A and the RMC are GMCs and should have clumps with roughly similar properties; the median temperature of the clumps of the RMC should not be half of that of the Orion A clumps. In short, there are three reasons why some of the clump temperatures in the RMC are probably underestimated:

1. The temperature versus clump size correlation argues for a spatial resolution effect.

2. Both the RMC and Orion A are GMCs forming massive stars and their clumps should have similar temperatures.

3. An additional reason is that the RMC is close to the Galactic plane (i.e. about 2°) and the dust temperatures in the plane is about 18 K (e.g., see Sodroski et al. 1994). If the RMC is like the Orion clouds in that its dust-gas temperature difference is small (Wall 2006), then the gas kinetic temperatures must be roughly double the listed values for some of the clumps.

Correcting all the RMC clump temperatures upwards by a factor of 2 would not be appropriate; the temperature-size correlation suggests that the correction factor should be largest for the "coldest," smallest clumps and progressively decrease towards unity for the "warmer," larger clumps.

How do these corrections to the temperatures affect the inferred X-factor values? A simple way to address this is to raise all the listed temperatures by a factor of 1.5. This approach is less extreme than doubling all of the temperatures and is simpler than finding some prescription for applying different scale factors to the temperatures of different-sized clumps. This temperature correction will then affect the observed column densities and, in turn, the inferred averaged densities by a factor $1.5^{\gamma-1.32}$ or 1.19. (Again, note that the "1.32" in the exponent becomes "1.00" for $T_K \gg 20$ K.) The theoretical X_f will then change by a factor of $1.5^{-0.47} \times 1.19^{0.35}$ or 0.88. The median X_f becomes $2.8\,X_{20}$. The observationally inferred X_f, however, increases by a factor 1.19 to about $2.0\,X_{20}$. Consequently, there is still a discrepancy between the X_f from the currently proposed formulation and that that would be inferred observationally; the theoretical X_f must be corrected downwards by 30%.

There is a similar but somewhat smaller discrepancy for the Orion clouds. The Orion clumps are filaments (Nagahama et al. 1998) and are treated here as $\rho \propto r^{-2}$ cylinders. This type of cylinder was treated in Section D.3.1 of Appendix D, but it was collapsing and magnetized. Here we assume the cylinders to be virialized and again adopt the average density to be over the entire volume. This gives $k_v = 2.76 \times 10^{-16}$ in *cgs* units and $k_N = (r_1/r_0)[2 - (r_0/r_1)][1 + 2\,ln(r_1/r_0)]^{-1}$. Here $r_1/r_0 = 14$ is adopted because it has the fluffiness of that obtained from the modeling in Section 3.3.1 (also see Section 4.4); numerical integration of (2) and comparison with (10) results in $\epsilon = 0.30$ and $k_A = 1.76$. Therefore,

$$X_f(X_{20}) = 0.57\ C_T\ T_K^{-0.48}\ n_a^{0.35} \tag{89}$$

The X_f value corresponding to each clump listed in Table 2 of Nagahama et al. (1998) was determined from the temperatures listed in, and the densities inferred from, that table. The densities were estimated from the listed filament masses and dimensions. For the Orion clouds, assuming cylindrical clumps and that the inferred densities are over the entire volume

will result in X_f values that range from 1.5 to $2.7\,X_{20}$ with a median value of $1.9\,X_{20}$, which is close to the observed value of about $2.1\,X_{20}$ (Wall 2006). (Note that this X_f applies to the one-component models of Wall (2006). The two-component models would imply that $X_f \simeq 3.5\,X_{20}$, except that it is uncertain exactly how much mass is in the other colder component — see Wall (2006b).) One additional consideration is that at least some of the observed filaments are being viewed partly end-on. If we were to simplistically assume that there were only end-on filaments with the same dimensions, densities, and temperatures as those listed in Table 2 of Nagahama et al. (1998), then the median X_f would roughly double, even though the $r_1/r_0 = 14$ cylinders considered here have $\epsilon = 0.53$ when viewed end-on. If we then consider that some of the filaments are partly end-on, then the best estimate of the theoretical X_f would be somewhere around $3\,X_{20}$. In fact, given that high-aspect filaments are more likely viewed side-on than end-on, this would probably be closer to about $2.5\,X_{20}$. Accordingly, the derived X-factor must be corrected downward by about 20-30% (assuming that $r_1/r_0 = 14$ is appropriate for the Orion filaments).

There are a few points to consider here. One is that average density defined as being over the whole cylindrical volume results in an X-factor that *increases* slowly with increasing ϵ; this is quite different from the behavior seen with the previous definition of average density (see Section 3.2.1 and Figure 4). Another point is that defining the average density this way results in fewer of the Orion A clumps being virialized; the fraction of clumps with velocity widths within 40% of the virialized width drops from 74% to 51%. And the final point is that the derived X-factor values must be corrected downwards by about 20-30% to match those observed. This may only require a better definition for the average density. It is also possible that simply redefining the average density is not enough to account for the discrepancy between the theoretical and observed X-factor values. There must be some additional consideration to be included in the formulation. This is not surprising given that the current formulation simplistically neglects the effects of magnetic fields and surface pressure (e.g., see Bertoldi & McKee 1992; Tilley & Pudritz 2003). It is likely that improved understanding of molecular cloud physical conditions is also necessary for reducing this discrepancy. In any event, the derived X-factor is within a factor of 2 of that observed.

4.7.2. The Galactic Center

The molecular gas within the central few hundred parsecs of the Galaxy represents an environment that is distinct from that of the Galactic disk. Compared to the disk gas, the molecular gas in the Galactic center is denser and hotter by an order of magnitude and very dynamically active (e.g., see Martin et al. 2004; Rodríguez-Fernández et al. 2001;

Paglione et al. 1998; Hüttemeister et al. 1998, 1993; Bally et al. 1988, 1987a; Harris et al. 1985; Güsten et al. 1985). Consequently, it is no surprise that the X-factor for the Galactic center clouds differs greatly from that for the Galactic disk clouds. Specifically, it is between a factor of a few and more than an order of magnitude smaller in the Galactic center than in the disk (see, e.g., Dahmen et al. 1998; Oka et al. 1998; Sodroski et al. 1995). Smaller X-factors may be common in the central few hundred parsecs of spiral galaxies (e.g., Rickard & Blitz 1985; Israel 1988; Wall et al. 1993; Regan 2000; Paglione et al. 2001)(see also Dahmen et al. 1998, and references therein).

How do we account for these low X-factors? Given that tidal forces may be appreciable in the Galactic center, the outer layers of clumps or clouds may be sheared off, producing a substantial interclump or intercloud medium (Stark et al. 1989). As mentioned in Section 3.2.4, if interclump gas dominates the ^{12}CO J = 1 $\rightarrow$ 0 emission and the gas mass, then X_f decreases because of the low average density in this gas. As stated in the previous paragraph, there is evidence for dense, hot molecular gas in the Galactic center region, but does this apply to the bulk of the CO-emitting gas in the Galactic center? If, for example, this CO-emitting gas is an order of magnitude hotter and an order of magnitude *less* dense than that in the Galactic disk, then the low X_f might be explained. However, the evidence for this is less than compelling. Dahmen et al. (1998) find high $I(^{12}\mathrm{CO\ J} = 1 \rightarrow 0)/\mathrm{I}(\mathrm{C}^{18}\mathrm{O\ J} = 1 \rightarrow 0)$ ratios that are sometimes nearly as high as the ^{12}CO/C^{18}O abundance ratio. They argue that the higher the $I(^{12}\mathrm{CO\ J} = 1 \rightarrow 0)/\mathrm{I}(\mathrm{C}^{18}\mathrm{O\ J} = 1 \rightarrow 0)$ ratio, the lower the gas density, claiming densities as low as $\mathrm{n(H_2)} \sim 10^2\,\mathrm{cm}^{-3}$, even though a simpler explanation is that the higher ratio only really implies lower optical depths in the J = 1 $\rightarrow$ 0 lines of ^{12}CO and ^{13}CO. These authors used observed molecular gas velocity gradients (or velocity widths per unit size) to impose constraints on the model velocity gradient. These observed gradients only really apply to the scale of entire clouds, and applying them to the model gradients is no more valid than applying such constraints to gas volume density. Such cloud-scale quantities are only rough lower limits to the relevant quantities to be used in non-LTE radiative codes, such as the LVG code. Assuming that the lowest and highest observed cloud-scale velocity gradients represent both lower and upper limits on the velocity gradients to be used in the LVG code is not correct and imposes an artificial connection between optical depth and density — both rise and fall together. Thus when the $I(^{12}\mathrm{CO\ J} = 1 \rightarrow 0)/\mathrm{I}(\mathrm{C}^{18}\mathrm{O\ J} = 1 \rightarrow 0)$ ratio approaches the abundance ratio, the optical depths of both ^{12}CO J = 1 $\rightarrow$ 0 and C^{18}O J = 1 $\rightarrow$ 0 drop and, because of the imposed constraint on the velocity gradient, the density drops too. Thus imposing constraints on the velocity gradients in this way leads to the assertion that $I(^{12}\mathrm{CO\ J} = 1 \rightarrow 0)/\mathrm{I}(\mathrm{C}^{18}\mathrm{O\ J} = 1 \rightarrow 0)$ being close to $X(^{12}\mathrm{CO})/\mathrm{X}(\mathrm{C}^{18}\mathrm{O})$ cannot occur in LTE — which is incorrect. Densities of $\mathrm{n(H_2)} \sim 10^2\,\mathrm{cm}^{-3}$ may indeed be present in the CO-emitting gas in the Galactic centre region, but it cannot be verified with

this line ratio alone; additional information is needed (and something more than *large*-scale velocity gradients).

Nonetheless, partly explaining the low X-factors in the Galactic center region is still possible. The large observed values of the $I(^{12}\mathrm{CO\ J} = 1 \rightarrow 0)/\mathrm{I}(\mathrm{C}^{18}\mathrm{O\ J} = 1 \rightarrow 0)$ ratio (Dahmen et al. 1998), for example, suggest that ^{12}CO J = 1 → 0 is optically thin or nearly so. From Table 1 we see that the optically thin case has X_f an order of magnitude or more lower than the Hard Sphere case, this latter having roughly the X_f for Galactic disk clouds when $\mathrm{T_K} = 20\,\mathrm{K}$ and $\mathrm{n(H_2)} = 2000\,\mathrm{cm^{-3}}$. One problem with this is that there is evidence that the molecular gas could have high kinetic temperatures, e.g. $\mathrm{T_K} \gtrsim 100\,\mathrm{K}$ (e.g., Martin et al. 2004; Rodríguez-Fernández et al. 2001; Hüttemeister et al. 1998, 1993; Güsten et al. 1985; Harris et al. 1985). If $\mathrm{T_K}$ is 100 K, then X_f *rises* to about $0.5\,X_{20}$ (see equation 34 in Section 3.1.2), or a factor of ~ 4 lower than that for the Galactic disk clouds. To have more than an order of magnitude lower X_f, an additional effect is necessary. The Galactic center's clouds are very dynamically active and have line widths factors of 5 to 10 larger than found in Galactic disk clouds (see, e.g., Bally et al. 1987a, 1988). If this also means that the velocities of the Galactic center gas are factors of 5 to 10 beyond virialization, then the effective k_v of this gas is larger than the virialized value by the same factors. Given that $X_f \propto k_v^{\epsilon-1}$, X_f would be reduced by factors between 1 and 5 to 10, depending on ϵ. If the ^{12}CO J = 1 → 0 line truly is optically thin, then $\epsilon = 1$ and the velocity structure is irrelevant (i.e., only *in*directly relevant because the velocity structure partly determines the optical depth) for determining X_f. Not all the observed $I(^{12}\mathrm{CO\ J} = 1 \rightarrow 0)/\mathrm{I}(\mathrm{C}^{18}\mathrm{O\ J} = 1 \rightarrow 0)$ ratios are high enough to indicate optically thin ^{12}CO J = 1 → 0, so an intermediate ϵ of 0.5 might be more appropriate. But this would only result in an X-factor that is only about a factor of 6 lower than the disk value. Finding X-factors that are more than an order of magnitude smaller (see Dahmen et al. 1998) in molecular gas that is warm and optically thin (or nearly so) is difficult to explain. Heightening the abundance of ^{12}CO by a factor of a few might do this, but it would lead to other difficulties, such as explaining how ^{12}CO J = 1 → 0 could be so close to being optically thin (as suggested by the high $I(^{12}\mathrm{CO\ J} = 1 \rightarrow 0)/\mathrm{I}(\mathrm{C}^{18}\mathrm{O\ J} = 1 \rightarrow 0)$ ratios). The best way to reduce X_f seems to be assuming that the gas behaves like fluffy clumps, something like the Squared Lorentzian Sphere. If the gas has a temperature of about 100 K and is still marginally optically thick, then it is easy to obtain $X_f \simeq 0.4\,X_{20}$ — a factor of about 5 smaller than in the Galactic disk. If we also consider that the gas velocity widths are an order of magnitude larger than required by virialization, then this reduces the X-factor another factor of nearly 3 and it can be an order of magnitude smaller than that in the disk.

In short, it is possible to explain X-factor values that are an order of magnitude smaller than is found in Galactic disk molecular clouds, but the really low values — nearly two

orders of magnitude smaller (see Dahmen et al. 1998) — are not so easily accounted for.

4.7.3. Irregular Galaxies

As discussed in Sections 3.2.2 and 4.2, the unusually high X-factors found in molecular clouds in irregular galaxies are largely due to the low abundances of ^{12}CO (or low $X(^{12}\mathrm{CO})$) in these galaxies. As listed in Israel (1997), the X_f values found in molecular clouds of irregular galaxies can range from a factor of a few to about 100 higher than that found in the Galactic disk molecular clouds. As described in Section 3.2.2, the abundance $X(^{12}\mathrm{CO})$ is an average over the volume of the molecular gas; there are CO-emitting regions with a Galactic abundance of CO surrounded by envelopes of CO-deficient molecular gas (see Israel 1997, 2000, and references therein). Consequently, a map of some molecular gas tracer that can show the molecular gas not traced by CO can be compared with CO maps to test the correlation between the observed X_f and the inferred volume ratio of molecular gas to CO-emitting gas. Madden et al. (1997), for example, map the low-metallicity irregular galaxy IC 10 in the [C II] 158 μm line and find that this emission is largely associated with molecular gas in photodissociation regions (PDRs). Their Figure 5 shows the contours of the [C II] 158 μm-line emission with superposed contours of CO emission. Depending on exactly how the relative areas are estimated, the ratio of projected areas of molecular gas to CO-emitting gas is about 10 to 20. Assuming that the volume goes like $(\mathrm{area})^{1.5}$, then these correspond to volume ratios of about 30 to 90. Accordingly, the volume-averaged $X(^{12}\mathrm{CO})$ would be roughly the Galactic disk value divided by these volume ratios. Given that the X-factor goes like $X_f \propto X(^{12}\mathrm{CO})^{-0.8}$ (see Section 4.2), X_f would be factors of about 15 to 40 larger than found in the Galactic disk; Madden et al. (1997) find that this factor to be about 100. Therefore, using only very crude estimates of the volume ratio of molecular gas to CO-emitting gas, the X-factor is estimated to within a factor of a few. If the molecular gas in IC 10 is very roughly representative of that in other irregular galaxies, then it is easy to understand the high X-factors in these galaxies. If X_f/X_{fG} is the ratio of the observed X-factor to the "standard" value found in Galactic disk clouds, and if A_r is the ratio of projected areas of molecular gas to CO-emitting gas, then $X_f/X_{fG} \simeq A_r^{1.2}$ is expected. Deviations from this dependence would be extremely interesting, providing clues to differences in physical conditions (e.g., ϵ, $\mathrm{n(H_2)}$, $\mathrm{T_K}$) between those in the molecular clouds of irregular galaxies and those in Galactic disk clouds.

5. Summary and Conclusions

An improved formulation for the X-factor is proposed that combines virialization of the gas with radiative transfer in a clumpy medium. The statement that the velocity-integrated radiation temperature of the ^{12}CO J = 1 → 0 line, $I(^{12}\mathrm{CO})$, "counts" optically thick clumps is quantified using the formalism of MSH84 for line emission in a clumpy cloud. Adopting the simplifying assumptions of thermalized ^{12}CO J = 1 → 0 line emission and isothermal gas, an effective optical depth, τ_{ef}, is defined as the product of the clump filling factor within each velocity interval, $\frac{N}{\mathrm{N_c}}\frac{\Delta \mathrm{v_c}}{\Delta \mathrm{v}}$, and the clump effective optical depth (or effective optically thick area), $\mathrm{A}(\tau_0)$, as a function of the optical depth, τ_0, on the clump's central sightline. The $\mathrm{A}(\tau_0)$ is well approximated (to within about 13-26%) as a power law in τ_0 with power-law index, ϵ, called the clump "fluffiness," and has values between zero and unity. While the ^{12}CO J = 1 → 0 line is optically thick within each clump (i.e., high τ_0), it is optically thin "to the clumps" (i.e., low τ_{ef}). Thus the dependence of $I(CO)$ on τ_{ef} is linear, resulting in an X-factor that depends only on the properties of the clumps rather than having a direct dependence on the entire cloud. Assuming virialization of the clumps yields an expression for the X-factor whose dependence on physical parameters like density and temperature are "softened" by power-law indices of less than unity that depend on the fluffiness parameter, ϵ. The X-factor provides estimates of gas column density because each sightline within the beam has optically thin gas within certain narrow velocity ranges. Determining column density from the optically thin gas is straightforward and parameters like ϵ then allow extrapolation of the column density of the optically thin gas to that of all the gas. Implicit in this formulation is the assumption that fluffiness is, on average, constant from one beam to the next. This is less true for density and temperature for which the X-factor, X_f, may have a weaker dependence.

The proposed formulation addresses the problems of the explanation proposed by DSS86:

1. *Treatment of radiative transfer.* The dependence on fluffiness, ϵ, represents a radiative transfer parameter of the clumps. The optically thin case results by simply setting $\epsilon = 1$: dependence on virialization disappears and the expression for column density in terms of $I(CO)$ in the optically thin case remains. In a hypothetical completely optically thick case with flat-topped line profiles, $\epsilon \rightarrow 0$ and the radiative transfer vanishes, leaving only virialization (as in DSS86).

2. *Reduced sensitivity to T_K and $n(H_2)$.* The effect of the fluffiness reduces the dependence of X_f on density and temperature from $X_f \propto \frac{\mathrm{n(H_2)^{0.5}}}{\mathrm{T_K}}$ to roughly $X_f \propto \left(\frac{\mathrm{n(H_2)}}{\mathrm{T_K}}\right)^{0.3}$ in the high-$\mathrm{T_K}$ limit. Thus variations of an order of magnitude in either n or $\mathrm{T_K}$ would allow X to vary by less than a factor of 2.

3. *Virialization of entire clouds is* un*necessary.* The densities required to give reasonable values of X_f are consistent with those found in cloud clumps (i.e. $\sim 10^3\,H_2\,\mathrm{cm}^{-3}$). Thus virialization of clumps, rather than of entire clouds, is consistent with the observed values of X_f. And even virialization of clumps is not strictly required; only a relationship between clump velocity width and column density similar to that of virialization can still yield reasonable values of the X-factor. The underlying physics is now at the level of cloud clumps, implying that the X-factor can probe sub-cloud structure.

4. *Stronger dependence of peak T_R on N(H_2) than of Δv on N(H_2) is now explained.* The peak $\mathrm{T_R}$ depends linearly on the filling factor within each velocity interval, $\frac{N}{\mathrm{N_c}}\frac{\Delta \mathrm{v_c}}{\Delta \mathrm{v}}$, thereby accounting for its dependence on $N(H_2)$. The Δv, on the other hand, is the observed line width and is not necessarily directly related to the beam-averaged column density, $N(H_2)$. If virialization is important at the level of the clumps, then the velocity width-column density relation is between that of the clump velocity width, $\Delta \mathrm{v_c}$, and clump column density, $\mathrm{N_c}$.

X-factor values were computed for both spherical clumps and cylindrical clumps (i.e. filaments) of densities 2×10^2, 2×10^3, and $2\times10^4\,H_2\,\mathrm{cm}^{-3}$ and kinetic temperatures 10 and 20 K and different internal density variations. The clumps of average density $2\times10^3\,H_2\,\mathrm{cm}^{-3}$ that reproduce the standard observed X_f value of about $2\,X_{20}$ for the Galactic disk clouds within a factor of 2 are the Hard Sphere (or uniform-density sphere), the Gaussian Sphere, and the Gaussian Filament (see Table 1). Aside from the clumps listed in Table 1, spherical clumps and filaments with average densities of $\sim 10^3\,H_2\,\mathrm{cm}^{-3}$ and an r^{-2} density variation can also produce X-factors within a factor of 2 of the standard value. Testing these clump types reveals a potentially strong inverse dependence of X_f on ϵ, as shown in Figure 4. Increasing the fluffiness has the advantage of weakening the dependence of the X-factor on density and temperature, but the disadvantage of decreasing X_f to values appreciably below the standard value. This strong dependence of X_f on ϵ is related to how the average density is defined. For clump types with no clearly defined outer radius (e.g., Gaussian or Squared Lorentzian), the average density was defined as that within a spherical or cylindrical (depending on clump geometry) diameter equal to the FWHM of the projected surface density distribution. For clumps with an r^{-2} density variation, an outer radius must be defined to keep the clump mass finite. The average density can be defined as done previously, but also can be defined over the whole clump volume. The latter definition can result in a weakly rising X_f as a function of ϵ.

The proposed formulation also suggests a specific dependence of the X-factor, X_f, on the ^{12}CO abundance, $X(^{12}\mathrm{CO})$. In the molecular clouds in irregular galaxies, the CO abundance within the CO-emitting regions is about the same as that in Galactic disk clouds, but the average over the entire molecular cloud volume is much lower (see Israel 1997, 2000, and

references therein). If $X(^{12}\mathrm{CO})$ is this volume-averaged abundance, then the formulation predicts $X_f \propto X(^{12}\mathrm{CO})^{0.7 \text{ to } 0.8}$ (for $\epsilon \simeq 0.3$). This is consistent with observations (see Section 4.2).

This formulation has implications for the interpretation of spectral line ratios, especially for the $I(^{13}\mathrm{CO\ J} = 1 \rightarrow 0)/\mathrm{I}(^{12}\mathrm{CO\ J} = 1 \rightarrow 0)$ ratio. Modeling the plot of this ratio against the effective optical depth, τ_{ef}, — determined from the peak radiation temperature of the $^{12}\mathrm{CO\ J} = 1 \rightarrow 0$ line normalized to the source function (in temperature units) — for the Orion clouds provides crude estimates of the fluffiness: $\epsilon \simeq 0.3 \pm 0.1$. Histograms of $^{13}\mathrm{CO\ J} = 1 \rightarrow 0/^{12}\mathrm{CO\ J} = 1 \rightarrow 0$ line strength ratios can also provide estimates of ϵ, and have the very important advantage that no estimates of the source function are necessary. Such a histogram from observations of the Orion clouds shows a peak that extends from $I(^{13}\mathrm{CO\ J} = 1 \rightarrow 0)/\mathrm{I}(^{12}\mathrm{CO\ J} = 1 \rightarrow 0) \simeq 0.1$ to 0.3. These limits for the Orion clouds (and possibly for other Galactic disk clouds) correspond to the minimum column density for self-shielding against the interstellar radiation field (i.e. $A_v \simeq 1\,mag$) at the low end and to the saturation of the $^{13}\mathrm{CO\ J} = 1 \rightarrow 0/^{12}\mathrm{CO\ J} = 1 \rightarrow 0$ line ratio at the high end. The value of this ratio at saturation is determined from the dominant value of ϵ (i.e. ~ 0.3) within the clouds' substructures. Consequently, a narrow range in ϵ can simultaneously account for the limited range of $^{13}\mathrm{CO\ J} = 1 \rightarrow 0/^{12}\mathrm{CO\ J} = 1 \rightarrow 0$ line ratios and for a relatively constant X-factor. In any event, it is no surprise that $^{13}\mathrm{CO\ J} = 1 \rightarrow 0/^{12}\mathrm{CO\ J} = 1 \rightarrow 0$ line ratio is related to the X-factor.

Observations of the $^{13}\mathrm{CO\ J} = 1 \rightarrow 0/^{12}\mathrm{CO\ J} = 1 \rightarrow 0$ line ratio have been used, for example, to infer differences in the X-factor between the molecular clouds of the nucleus of a spiral galaxy and that of its disk clouds (e.g., Rickard & Blitz 1985; Paglione et al. 2001). The formulation finds a linear relationship between X_f and $I(^{13}\mathrm{CO\ J} = 1 \rightarrow 0)/\mathrm{I}(^{12}\mathrm{CO\ J} = 1 \rightarrow 0)$, provided that $\mathrm{T_K}$ and $X(^{13}\mathrm{CO})/\mathrm{X}(^{12}\mathrm{CO})$ (or x_r) are constant. If these quantities vary spatially, then X_f can have a dependence on $I(^{13}\mathrm{CO\ J} = 1 \rightarrow 0)/\mathrm{I}(^{12}\mathrm{CO\ J} = 1 \rightarrow 0)$ that is weaker than linear.

The proposed formulation and observed $I(^{13}\mathrm{CO\ J} = 1 \rightarrow 0)/\mathrm{I}(^{12}\mathrm{CO\ J} = 1 \rightarrow 0)$ ratios, or observed X-factor values, can constrain estimates of properties of substructures within molecular clouds, often by imposing limits on estimates of the fluffiness, ϵ. Many clumps or small clouds have an r^{-2} density (or ρ) dependence. If the clump outer radius is, r_1, and the inner radius of the $\rho \propto r^{-2}$ region within the clump is r_0, then the ratio r_1/r_0 is constrained by the limits on ϵ. Given that $\epsilon \simeq 0.2$ to 0.4, and assuming that $\rho \propto r^{-2}$ structures are the dominant source of the $^{12}\mathrm{CO\ J} = 1 \rightarrow 0$ emission, spherical clumps would have $r_1/r_0 = 2$ to 9 and cylindrical clumps would have $r_1/r_0 = 4$ to 42. Observations are apparently consistent with these limits, where r_1/r_0 is about 4 to 15 (e.g., Harvey et al. 2001; Tachihara et al. 2000;

Lada et al. 1999; Alves et al. 1998; Henriksen et al. 1997; Williams et al. 1995), although spatial resolution limitations often mean that the observed numbers are merely lower limits.

The properties of real clumps in real molecular clouds can be used to estimate the X-factor within these clouds and then be compared with the observationally determined X-factor. Applying this to the Orion A cloud (Nagahama et al. 1998) and the Rosette Molecular Cloud or RMC (Williams et al. 1995) yields estimates of the X-factor that are within a factor of 2 of the observed values. While this is acceptable as a start, reducing this discrepancy will require improving the formulation. Simply changing the definition of the average density can reduce the discrepancy, but it seems likely that something else is missing from the current formulation.

A future, improved formulation for the X-factor must address the following shortcomings of the current formulation:

A) It is not entirely clear why the fluffiness seems to be constant, or at least sharply peaked, at one value. This value seems to be about $\epsilon \simeq 0.3$.

B) The resultant X-factor values are too dependent on the precise definition of the average density. A closer to optimal way of defining such a density must be found.

C) The desired insensitivity of the X-factor to density and temperature often comes at the price of too low an X-factor value. Again, this is affected by the definition of average density.

D) There is a potentially strong dependence on the fluffiness, ϵ. This dependence can be weakened by the appropriate choice for the definition of average clump density.

E) The current formulation does not consider clumps with a spectrum of properties, such as distributions of densities and temperatures. This will introduce other parameters in addition to ϵ, T_K, and $n(H_2)$ for determining the X-factor.

F) Additional physical effects must be considered. These would include non-LTE effects and the effects of magnetic fields, surface pressure, and turbulence.

G) Observational determinations of parameters such as ϵ can be complicated by clumps having a spectrum of properties, such as ranges in densities, temperatures, optical depths, etc. The presence of interclump gas might complicate this as well.

Despite these shortcomings, the currently proposed formulation represents the first major improvement in understanding the X-factor since Dickman et al. (1986) (i.e., DSS86),

because it includes radiative transfer. Previous explanations of the X-factor involved counting optically thick clumps (or entire clouds) and a relationship between the gas column density and the velocity width of the CO J = 1 → 0 spectal line (e.g., DSS86 Israel 1988; Evans 1999). But applying the DSS86 approach directly to cloud clumps often overestimates the X-factor. At first glance, applying radiative transfer to an optically thick line is apparently pointless. However, portions of the gas are not optically thick, permitting estimates of the mass of the gas when radiative transfer is considered. And including radiative transfer does indeed result in reasonable estimates of the X-factor even when applying the formulation to the level of individual clumps.

Determination of the X-factor on scales of many parsecs can constrain the average properties of the molecular gas at scales of just a few parsecs. Future formulations may refine the X-factor into a potent probe of molecular cloud structure.

This work was supported by CONACyT grant #211290-5-0008PE to W. F. W. at *INAOE.* I am very grateful to W. T. Reach for his comments and support. I thank T. A. D. Paglione, G. MacLeod, E. Vazquez Semadeni, F. P. Israel and others for stimulating and useful discussions. The author is grateful to R. Maddalena and T. Dame, who supplied the map of the peak ^{12}CO J = 1 → 0 line strengths and provided important calibration information.

A. The Effective Optical Depth of a Single Clump

MSH84 derive the effective optical depth of a clump, A(τ_0), which they call the effective optically thick area, for the case of a clump with a Gaussian spatial variation of its optical depth. This appendix gives a quick derivation of A(τ_0) for a clump with a more general optical depth variation. MSH84 derive the effective optical depth on a line of sight through a clumpy cloud:

$$\tau_{ef}(v_z) = \frac{\mathcal{N}_c}{\sqrt{2\pi}\ \Delta \mathrm{v}} \int dv\, exp\left(-\frac{v^2}{2\,\Delta \mathrm{v}^2}\right) \int dx \int dy \left\{1 - exp\left[-\tau(x,y)\, exp\left(-\frac{(v-v_z)^2}{2\,\Delta \mathrm{v_c}^2}\right)\right]\right\} \quad . \tag{A1}$$

Notice that different notation from that of MSH84 is used here. The $\mathcal{N}_c$ is the number of clumps per unit projected area of the cloud and corresponds to the N of MSH84. The velocity widths here are rms velocity widths, whereas those of MSH84 are ratios of the Gaussian line profile areas to their amplitudes. This results in extra factors of $\sqrt{2\pi}$. The spectral line velocity width was represented by σ in MSH84 and is given by $\sqrt{2\pi}\Delta$v here. The velocity width of a single clump was v_o in MSH84 and is $\sqrt{2\pi}\Delta \mathrm{v_c}$ here. The velocity v_z is the bulk velocity of a clump along the sightline and the velocity, v, is the velocity of a

given element of gas along the sightline. Following MSH84, the assumption of the line width being much greater than the velocity width of a single clump, i.e. $\Delta \mathrm{v} \gg \Delta \mathrm{v_c}$, is adopted. This means that v cannot deviate too far from v_z without making the integrand very small. At the same time, the first exponential factor of the integrand does not change much from $exp(-v_z^2/(2\,\Delta \mathrm{v}^2))$, because $\Delta \mathrm{v}$ is so much larger than $\Delta \mathrm{v_c}$. Consequently, expression (A1) simplifies:

$$\tau_{ef}(v_z) = \frac{\mathcal{N}_c}{\sqrt{2\pi}\ \Delta \mathrm{v}}\, exp\left(-\frac{v_z^2}{2\,\Delta \mathrm{v}^2}\right) \int dv' \int dx \int dy \left\{1 - exp\left[-\tau(x,y)\, exp\left(-\frac{v'^2}{2\,\Delta \mathrm{v_c}^2}\right)\right]\right\} \quad , \tag{A2}$$

where v' replaced $v - v_z$. Now the integrals are only over the clump velocity width and the clump's projected surface area. Therefore, the integrals, when properly normalized, must give the effective optical depth of a single clump, $\mathrm{A}(\tau_0)$. Normalizing for the velocity width requires dividing by $\sqrt{2\pi}\Delta \mathrm{v_c}$. Normalizing for the effective projected area of the clump requires dividing by $a_{_{eff}}$ (see equation 3). This results in equation (2), as desired.

Equation (A2) then becomes

$$\tau_{ef}(v_z) = \frac{a_{_{eff}} \mathcal{N}_c\, \Delta \mathrm{v_c}}{\Delta \mathrm{v}}\, \mathrm{A}(\tau_0) \exp\left(-\frac{{v_z}^2}{2\,\Delta \mathrm{v}^2}\right) \quad . \tag{A3}$$

Given that $a_{_{eff}} \mathcal{N}_c = N/\mathrm{N_c}$, equation (A3) becomes equation (1), also as desired.

Equation (1) can be used as the starting point instead. It represents a logical relationship between the effective optical depth through the cloud and that for a single clump; its derivation is trivial. Comparing equation (1) with equation (A2) then gives equation (2) for $\mathrm{A}(\tau_0)$.

The reader may have noticed that the definition of $\mathrm{A}(\tau_0)$ is lacking a certain geometric correction. For example, in the $\tau_0 \ll 1$ limit, $\mathrm{A}(\tau_0) \simeq \tau_0$. And yet $\mathrm{A}(\tau_0)$, which is an appropriately averaged τ over the projected surface of the clump, cannot simply be the τ through the center of the clump, i.e. τ_0. It must be less than this value, at least for those clumps where τ_0 is highest on the central sightline. Consider, for example, the hard sphere, which means a sphere with clearly defined edges and uniform internal density. (See MSH84 for their treatment of hard spheres.) Since we are only considering LTE and uniform kinetic temperatures, and that these clumps have uniform internal density, the optical depth on any given sightline through the clump is proportional to the path length through the clump on that sightline. The average path length through a hard sphere is its volume divided by its projected area or $\frac{2}{3}d$, where d is the sphere's diameter. The average optical depth of such a sphere in the optically thin limit is then $\frac{2}{3}\tau_0$ rather than simply τ_0. However, the clump optical depth, $\mathrm{N_c}$, as defined in the text is also used as the column density on the

central sightline through the clump. This means that $N/\mathrm{N_c}$ is not exactly the number of clumps in the beam as stated in the text: a slight correction factor is needed. Nevertheless, this correction factor cancels that needed for $\mathrm{A}(\tau_0)$, thereby yielding the correct result for τ_{ef}. Another way to argue this is to consider the factors $\mathrm{A}(\tau_0)/\mathrm{N_c}$ and $N\Delta\mathrm{v_c}/\Delta\mathrm{v}$. The former factor is the average optical depth per unit column density for a clump, since both $\mathrm{A}(\tau_0)$ and $\mathrm{N_c}$ are referred to the central sightline. The latter factor is the beam-averaged column density within velocity interval $\Delta\mathrm{v_c}$ at the line central velocity, $v_z = 0$. Therefore, the product of the the two factors must give the optical depth at the line central velocity, and this is equation (1) evaluated at $v_z = 0$, as desired.

B. The X-Factor for a Small Beam on a Uniform-Density Cloud

Here the $N(H_2)/I(CO)$ conversion factor is estimated for the case of a beam much smaller than the source, where that source is a uniform-density cloud. The velocity-integrated radiation temperature of the ^{12}CO J = 1 → 0 line, $I(CO)$, in LTE in a cloud of uniform kinetic temperature is

$$I(CO) = \mathcal{J}_\nu(\mathrm{T_K}) \int_{\mathrm{line}} \mathrm{dv}\ [1\ -\ \exp(-\tau(\mathrm{v}))] \qquad , \tag{B1}$$

where the integral is over the spectral line profile. The optical depth velocity profile is

$$\tau(v) = \tau_0\, exp\left(-\frac{v^2}{2\,\Delta\mathrm{v}^2}\right) \qquad . \tag{B2}$$

Numerically integrating (B1) shows that the integral can be approximated by

$$\int_{line} dv\ [1\ -\ exp(-\tau(v))] \simeq \sqrt{2\pi}\,\Delta\mathrm{v}\,\mathrm{k_A}\,\tau_0^\epsilon \qquad , \tag{B3}$$

where $k_A = 1.3$ and $\epsilon = 0.14$. If we now assume a uniform density sphere and virialization, then the derivation of Δv of Section 2.2 is relevant. It is also assumed that the velocity width on whatever sightline through the cloud reflects the virialization of the entire cloud and does not have appreciable contributions from other types of motion. Repeating the derivation of Section 2.4 again yields equation (28). This means that this equation and its variants (see Appendices C and D) are more general than only treating radiative transfer through a clumpy medium. All that is required is that $I(CO) \propto \tau_0^\epsilon$ and $\Delta\mathrm{v} \propto (\mathrm{N\,L})^{0.5}$, where N and L are the column density and pathlength, respectively, on the sightline through the cloud. In fact, the density and kinetic temperature that appear in expression (28) must be replaced, in

the current treatment only, by the corresponding quantities that are appropriately averaged over the entire cloud, rather than for just an individual clump.

C. Treatment of Spherically Symmetric Clumps

Here we assume that the mass density ρ is simply a function of the radius, r, within each spherical clump: $\rho = \rho(r)$. This is similarly true for the number density, $n(r)$. If the x-y plane is perpendicular to the observer's sightline and z is measured along the sightline, then $n(r)$ is $n(\sqrt{p^2+z^2})$, where $p \equiv \sqrt{x^2+y^2}$ is the projected radius as seen by the observer. The clump column density as a function of projected radius, $N_c(p)$, is given by

$$N_c(p) = \int_{-\infty}^{+\infty} dz\; n(\sqrt{p^2+z^2}) \quad . \tag{C1}$$

The mass within radius r, $M(r)$, is given by

$$M_c(r) = 4\pi \int_0^r d\mathcal{R}\; \mathcal{R}^2\, \rho(\mathcal{R}) \quad . \tag{C2}$$

A useful quantity is the average density $\bar{\rho}$. This can be defined in a number of ways, but is chosen here to be in terms of the half-width-at-half-maximum projected radius of the clump, $p_{1/2}$, defined such that $N_c(p_{1/2}) \equiv 0.5\, N_c(p=0)$. Then $\bar{\rho}$ is

$$\bar{\rho} \equiv \frac{M_c(r=p_{1/2})}{\frac{4\pi}{3} p_{1/2}^3} \quad . \tag{C3}$$

The self-potential due to gravity is

$$W = -16\pi^2 G \int_0^\infty d\mathcal{R}\; \mathcal{R}^2 \rho(\mathcal{R}) \int_0^{\mathcal{R}} d\mathcal{R}'\; \frac{\mathcal{R}'^2}{\mathcal{R}}\, \rho(\mathcal{R}') \quad . \tag{C4}$$

If N_c is defined as the column density through the clump center — i.e., $N_c \equiv N_c(p=0)$ — and M_c is defined as the total clump gas mass — i.e., $M_c \equiv M_c(r=\infty)$, then we can write these and W as

$$N_c = 2\, k_N\, \bar{\mathrm{n}}\, p_{1/2} \quad , \tag{C5}$$

$$M_c = k_M\, \bar{\rho}\, p_{1/2}^3 \quad , \tag{C6}$$

$$W = -k_W\, \frac{GM_c^2}{p_{1/2}} \quad . \tag{C7}$$

The constants k_N, k_M, and k_W are given by the precise functional form of $\rho(r)$. Specifically, these constants are determined by comparing equations (C1), (C2), and (C4) with (C5), (C6), and (C7), respectively.

The simple form of the Virial theorem applied in Section 2.2 and the full-width-at-half-maximum, $d_{1/2} \equiv 2p_{1/2}$, are now used to derive $\Delta \mathrm{v_c}$:

$$\Delta \mathrm{v_c} \;=\; k_v \; \bar{\mathrm{n}}^{\frac{1}{2}} \; d_{1/2} \quad , \tag{C8}$$

where

$$k_v \;\equiv\; \left[\frac{1}{12} \; k_W \; k_M \; \mu \mathrm{m_{H2}} \mathrm{G}\right]^{\frac{1}{2}} \quad , \tag{C9}$$

where the expressions (C6) and (C7) and $\bar{\rho} = \mu \, \mathrm{m_{H2}} \, \bar{\mathrm{n}}$ was also used (also see Section 2.2).

In addition to the above equations, we need the appropriate equation for τ_0. Starting with equation (21) and plugging in (C8) and (C5) yields,

$$\tau_0 = \frac{k_\tau k_N}{k_v \sqrt{2\pi}} \, \bar{\mathrm{n}}^{0.5} \mathrm{T_K}^{-\gamma} \quad , \tag{C10}$$

which is a more general form of (22). Equation (22) assumed a sphere of uniform density, for which $k_N = 1$, and (C10) reduces to (22).

Now we can combine the expressions developed here with (25), (26), and (10) to obtain,

$$X_f = (2\pi)^{\frac{1}{2}(\epsilon-1)} \, C_T \, k_A^{-1} \, k_\tau^{-\epsilon} \, k_v^{\epsilon-1} \, k_N^{1-\epsilon} \, \mathrm{T_K}^{\gamma\epsilon-1} \, \bar{\mathrm{n}}^{\frac{1}{2}(1-\epsilon)} \quad . \tag{C11}$$

This is a more general version of equation (28), which assumed a uniform-density sphere. In fact, equation (C11) is more general than for just spherical clumps: as long as $\Delta \mathrm{v_c}$, $N_c(0)$, τ_0, and $\mathrm{A}(\tau_0)$ can be represented by expressions (C8), (C5), (C10), and (10), respectively, the expression for the X-factor can have the specific form given by (C11).

A few examples of spherically symmetric clumps are examined in the following subsections.

C.1. Uniform-Density Sphere

This case is also called the "Hard Sphere" in Section 3.1, the tables, and in MSH84. Because the hard sphere has a well-defined edge with a well-defined radius, R, this R is used in place of $p_{1/2}$. The density, $\rho(r)$, is constant and equal to both ρ_c and $\bar{\rho}$. Similarly $n(r) \equiv n_c$ and $n(r) \equiv \bar{\mathrm{n}}$ for all r from zero up to R. Accordingly, it is trivial to show that

$k_M = \frac{4\pi}{3}$, $k_W = \frac{3}{5}$, and $k_N = 1$. It then follows that expressions (16), (22), and (28) result from (C9), (C10), and (C11), respectively. The central sightline optical depth, τ_0, is then,

$$\tau_0 = 1.18 \times 10^2 \, n_c^{0.5} \, \mathrm{T_K^{-1.75}} \quad , \tag{C12}$$

for $\mathrm{T_K} = 10$ to 20 K. These values along with the k_A and ϵ values given in Subsection 3.1.2 yield,

$$X_f(X_{20}) = 0.488 \, C_T \, \mathrm{T_K^{-0.76}} \, \bar{\mathrm{n}}^{0.43} \quad , \tag{C13}$$

where this X-factor is in units of X_{20} or $10^{20} \, H_2 \; molecules \cdot \; \mathrm{cm^{-2}} \cdot (\mathrm{K \cdot km \cdot s^{-1}})^{-1}$.

Specific numerical results of these calculations are listed in Tables 1 through 5.

C.2. Gaussian Sphere

The optical depth profile, $\tau(p)$, for the Gaussian sphere is given by (9). For an isothermal clump in LTE, the volume density, $\rho(r)$, that would give this $\tau(p)$ is Gaussian:

$$\rho(r) = \rho_0 \, exp\left(-\frac{r^2}{\sigma_r^2}\right) \quad , \tag{C14}$$

where ρ_0 is the density at the center of the sphere and σ_r is the (1/e)-folding radius for the density variation. The analogous expression exists for $n(r)$ and placing this in (C1) results in

$$N_c(p) = n_0 \, \sqrt{\pi} \, exp\left(-\frac{p^2}{\sigma_r^2}\right) \quad . \tag{C15}$$

so that $N_c = n_0 \, \sqrt{\pi} \, \sigma_r$. From (C15) we see that $\sigma_r = p_{1/2}/\sqrt{ln\,2}$. The mass as a function of r is

$$\frac{M_c(r)}{M_c(\infty)} \;=\; erf\left(\frac{r}{\sigma_r}\right) - \frac{2r}{\sigma_r \sqrt{\pi}} \, exp\left(-\frac{r^2}{\sigma_r^2}\right) \quad , \tag{C16}$$

where,

$$M_c(\infty) \;=\; \pi^{\frac{3}{2}} \, \rho_0 \, \sigma_r^3 \quad . \tag{C17}$$

The erf is the Gaussian error function. Replacing r with $p_{1/2}$ in (C16) yields $M_c(p_{1/2})/M_c(\infty) = 0.2878$. Placing this into (C3) gives us $\bar{\rho} = 0.6630 \, \rho_0$. Accordingly, $k_N = 1.606$, $k_M = 14.55$. Using expressions (C4) and (C7) gives $k_W = \sqrt{(ln\,2)/2\,\pi} = 0.3321$, which in turn gives $k_v = 3.420 \times 10^{16} cgs$. The central sightline optical depth, τ_0, is accordingly,

$$\tau_0 = 1.38 \times 10^2 \, \bar{\mathrm{n}}^{0.5} \, \mathrm{T_K^{-1.75}} \quad , \tag{C18}$$

for $T_K = 10$ to 20 K. These together with the k_A and ϵ values given in Subsection 3.1.3 yield,

$$X_f(X_{20}) = 0.204\, C_T\, T_K^{-0.38}\, \bar{n}^{0.32} \quad . \tag{C19}$$

Specific numerical results of these calculations are listed in Tables 1 through 5.

C.3. Squared-Lorentzian Sphere

This case was discussed in MSH84. The optical depth profile is given by

$$\tau(p) = \tau_0(0)\, \left[1 + \left(\frac{p^2}{r_0^2}\right)\right]^{-2} \quad , \tag{C20}$$

where the r_0 is the projected radius at which τ falls to $0.25\,\tau_0$. It also gives the effective area, where $a_{eff} = \pi\, r_0^2$. For an isothermal clump in LTE, it follows that

$$N_c(p) = N_c(0)\, \left[1 + \left(\frac{p^2}{r_0^2}\right)\right]^{-2} \quad . \tag{C21}$$

It is easy to show that $r_0 = (\sqrt{2} - 1)^{-0.5}\, p_{1/2}$. The volume density, $\rho(r)$, that corresponds to the surface density of equation (C21) is

$$\rho(r) = \rho_0\, \left[1 + \left(\frac{r^2}{r_0^2}\right)\right]^{-2.5} \quad . \tag{C22}$$

This is easily demonstrated by substituting the expression analogous to (C22) for $n_c(r)$ into (C1). Doing so gives,

$$N_c = \frac{4}{3}\, n_0\, r_0 \quad . \tag{C23}$$

Substituting (C22) into (C2) results in,

$$\frac{M_c(r)}{M_c(\infty)} \;=\; \left[\left(\frac{r^2}{r_0^2}\right) + 1\right]^{-1.5} \quad , \tag{C24}$$

where,

$$M_c(\infty) \;=\; \frac{4\pi}{3}\, \rho_0\, r_0^3 \quad . \tag{C25}$$

Applying (C3) yields $\bar{\rho} = 2^{-0.75}\, \rho_0$. Consequently,

$$\begin{aligned} k_N &= \frac{4}{3}\, \left(2 - \sqrt{2}\right)^{-0.5} \\ &= 1.742 \end{aligned} \tag{C26}$$

and

$$k_M = \frac{4\pi}{3}\left(2^{0.75}\right)\left(\sqrt{2}-1\right)^{-1.5} = 26.43 \quad . \tag{C27}$$

Plugging (C22) into (C4) and doing some work yields

$$k_W = \frac{3\pi}{32}\left(\sqrt{2}-1\right)^{0.5} = 0.1896 \quad . \tag{C28}$$

From these the following is obtained:

$$k_v = \left[\frac{\pi^2}{96\left(\sqrt{2}-1\right)}\left(2^{0.75}\right)\mu\,\mathrm{m_{H2}}\,\mathrm{G}\right]^{0.5} = 3.481\times10^{-16} cgs \quad . \tag{C29}$$

The above results give the central sightline optical depth:

$$\tau_0 = 1.46\times10^2\,\bar{\mathrm{n}}^{0.5}\,\mathrm{T_K^{-1.75}} \quad , \tag{C30}$$

for $\mathrm{T_K}$ = 10 to 20 K. All of the above results along with the k_A and ϵ values given in Subsection 3.1.3 give

$$X_f(X_{20}) = 0.0756\,C_T\,\mathrm{T_K^{-0.003}}\,\bar{\mathrm{n}}^{0.22} \quad . \tag{C31}$$

Specific numerical results of these calculations are listed in Tables 1 through 5.

C.4. $\rho \propto \mathbf{r^{-2}}$ Sphere

The adopted sphere density, $\rho(r)$, is flat for $r \le r_0$ and falls like r^{-2} outside of this and out to $r = r_1$:

$$\rho(r) = \rho_0 \qquad for\ r \le r_0 \tag{C32}$$

$$= \rho_0\left(\frac{r_0}{r}\right)^2 \quad for\ r_0 \le r \le r_1 \quad . \tag{C33}$$

It is easy to show that the mass is given by

$$M_c(r_1) = \frac{4\pi}{3}\,\rho_0\,r_0^3\left(3\frac{r_1}{r_0} - 2\right) \quad . \tag{C34}$$

Notice that the mass, $M_c(r_1)$, would diverge if $r_1 \rightarrow \infty$, so a maximum radius, r_1 must be specified. The usual quantities (e.g., for k_v and k_N) must now be determined in terms of $M_c(r_1)$ instead of $M_c(\infty)$. Employing expressions (C1) and the number density analogs of (C32) and (C33) yields

$$N_c(p) = 2n_0\sqrt{r_0^2 - p^2} + \frac{2\, n_0\, r_0^2}{p}\left[arccos\left(\frac{p}{r_1}\right) - arccos\left(\frac{p}{r_0}\right)\right] \quad for\ p \leq r_0 \quad \text{(C35)}$$

$$= \pi\ n_0\, r_0^2\, p^{-1}\, arccos\left(\frac{p}{r_1}\right) \quad for\ r_0 \leq p \leq r_1, \quad \text{(C36)}$$

where $N_c(0) = 2\, n_0\, r_0\, (2\ -\ \frac{r_0}{r_1})$.

Determining the self-potential, W, and applying the simple form of the Virial theorem leads to

$$\Delta \mathrm{v_c^2} = 4\,\pi\,\mathrm{G}\,\rho_0\,\mathrm{r_0^2}\ \ \frac{\frac{\mathrm{r_1}}{\mathrm{r_0}}\ -\ \frac{2}{3}\,\ln\left(\frac{\mathrm{r_1}}{\mathrm{r_0}}\right)\ -\ \frac{14}{15}}{3\frac{\mathrm{r_1}}{\mathrm{r_0}}\ -\ 2} \quad . \quad \text{(C37)}$$

For simplicity, $\frac{r_1}{r_0} \gg 1$ is assumed and

$$\Delta \mathrm{v_c} = \left[\frac{4\,\pi}{3}\,\mathrm{G}\,\mu\,\mathrm{m_{H2}}\right]^{0.5}\ \mathrm{n_0^{0.5}}\ \mathrm{r_0} \quad , \quad \text{(C38)}$$

where $\rho_0 = n_0\,\mu\,\mathrm{m_{H2}}$ was used. It can be shown that

$$r_0 = \frac{2}{\pi}\ p_{1/2} \quad \text{(C39)}$$

and

$$\rho_0 = \frac{\pi^3}{4\,(3\pi\ -\ 4)}\ \bar{\rho} \quad , \quad \text{(C40)}$$

$$= 1.429\,\bar{\rho}$$

Expressions (C39) and (C40) again assume that $\frac{r_1}{r_0} \gg 1$. With these expressions in hand, expressions for k_N and k_v follow:

$$k_N = \frac{\pi^2}{3\pi\ -\ 4} \quad , \quad \text{(C41)}$$

$$= 1.819$$

and

$$k_v = \left[\frac{\pi^2}{3\,(3\pi\ -\ 4)}\,G\,\mu\,\mathrm{m_{H2}}\right]^{0.5} \quad , \quad \text{(C42)}$$

$$= 4.20 \times 10^{-16}\ cgs \quad .$$

Computing X_f requires specifying r_1/r_0. The particular example discussed in Section 4.7.1 is of the Rosette Molecular Cloud, where Williams et al. (1995) find $\frac{r_1}{r_0} = 5$ for many of the clumps. Simple numerical integration yields $\epsilon = 0.30$ and $k_A = 1.80$ for this value of $\frac{r_1}{r_0}$. Therefore,

$$X_f(X_{20}) = 0.22\ C_T\ \mathrm{T_K^{-0.47}}\ \bar{\mathrm{n}}^{0.35} \tag{C43}$$

Because the r^{-2} sphere must have an outer radius, the average density can also be defined as over the entire volume — i.e., n_a. Doing this changes k_N and k_v:

$$k_N = 2\,\frac{r_1}{r_0} \qquad , \tag{C44}$$

and

$$\begin{aligned} k_v &= \left[\frac{\pi}{9}\,G\,\mu\,\mathrm{m_{H2}}\right]^{0.5} \qquad , \\ &= 3.18 \times 10^{-16}\ cgs \qquad . \end{aligned} \tag{C45}$$

For the clumps of the Rosette Molecular Cloud, again using the numbers of the previous paragraph, we have,

$$X_f(X_{20}) = 0.88\ C_T\ \mathrm{T_K^{-0.47}}\ \mathrm{n_a^{0.35}} \tag{C46}$$

D. Treatment of Cylindrically Symmetric Clumps

D.1. Viewed Perpendicularly to the Axis of Symmetry: The Side-on Case

Here the mass density ρ is adopted to be a function of the radius from an axis of symmetry, r, within each cylindrical clump: $\rho = \rho(r)$. This is also true for the number density, $n(r)$. Again, the x-y plane is chosen to be perpendicular to the observer's sightline and z is measured along the sightline. The x-axis is selected to be along the cylinder's symmetry axis and is also perpendicular to the observer's sightline. The y-axis is perpendicular to both the observer's sightline and the symmetry axis; the y is the projected distance from the cylinder's central axis. The radius, r, is then $y^2 + z^2$. The cylinder's length is h. The clump column density as a function of projected distance from the central axis, $N_c(y)$, is given by

$$N_c(y) = \int_{-\infty}^{+\infty} dz\ n(\sqrt{y^2 + z^2}) \quad . \tag{D1}$$

The mass within radius r, $M(r)$, is given by

$$M_c(r) = 2\pi\ h \int_0^r d\mathcal{R}\ \mathcal{R}\,\rho(\mathcal{R}) \quad . \tag{D2}$$

The half-width-at-half-maximum distance from the symmetry axis, $y_{1/2}$, is defined by $N_c(y_{1/2}) \equiv 0.5\, N_c(y=0)$. The average density, $\bar{\rho}$, is defined analogously to that of expression (C3):

$$\bar{\rho} = \frac{M_c(r = y_{1/2})}{\pi\, y_{1/2}^2\, h} \quad . \tag{D3}$$

The self-potential due to gravity is

$$W = -k_F\, \frac{GM_c^2}{h} \quad , \tag{D4}$$

where $k_F = 1$ in the limit $h/d_{1/2} \gg 1$ (and $d_{1/2} = 2y_{1/2}$). Equation (D4) in this limit is found from solving the Poisson equation in cylindrical coordinates. The parameter k_F is a correction factor for when $h/d_{1/2} \gg 1$ is false; a crude numerical analysis suggests that for $h/d_{1/2} \geq 1$, $k_F < 1.4$. A similar value is found from a very crude analytical approach. If the cylinder is of uniform density with radius, R, and has length, $h = 2R$, then the cylinder very roughly approximates a uniform density sphere of radius, R. From Appendix C.1, we know that $k_W = 0.6$. Placing $h = 2R$ into (D4) and comparing with the uniform sphere, we find that $k_F \simeq 1.2$. In any event, the final dependence of the relevant quantities on k_F will be weak and setting this to unity will be sufficient (see below).

Many parameters have similar or identical expressions to those in Appendix C. The parameter k_N is defined similarly to that in equation (C5), but with $y_{1/2}$ in place of $p_{1/2}$. The k_M is defined in terms of a cylindrical variation of equation (C6):

$$M_c \equiv k_M\, \bar{\rho}\; h\; y_{1/2}^2 \quad . \tag{D5}$$

The parameter k_W does not apply in this case because W is not dependent on r, except for the weak implicit r-dependence of k_F. The expression for $\Delta \mathrm{v_c}$ is the same as (C8) and the expression for k_v is almost the same as (C9):

$$k_v = \left[\frac{1}{12}\; k_F\; k_M\; \mu\, \mathrm{m_{H2}}\, \mathrm{G}\right]^{\frac{1}{2}} \quad . \tag{D6}$$

The equations for τ_0 and X_f are still (C10) and (C11). Given that $X_f \propto k_v^{\epsilon-1}$ and that $k_v \propto k_F^{0.5}$, $X_f \propto k_F^{0.5(\epsilon-1)}$. Even for a value of ϵ as low as that in a hard sphere, the dependence of X_f on k_F is weak: $X_f \propto k_F^{0.43}$. Since k_F is between 1.0 and 1.4, the effect on X_f is less than 16%.

D.1.1. Gaussian Cylinder

The volume density, $\rho(r)$, is given by,

$$\rho(r) = \rho_0\, exp\left(-\frac{r^2}{\sigma_r^2}\right) \quad . \tag{D7}$$

This is apparently identical to (C14), except that the r and σ_r here are defined as distances from the central axis rather than a central point. From (D7), it is easy to show that,

$$N_c(y) = N_c(0)\ exp\left(-\frac{y^2}{\sigma_r^2}\right) \quad , \tag{D8}$$

where,

$$N_c(0) = \sqrt{\pi}\ n_0\ \sigma_r \quad , \tag{D9}$$

and,

$$M_c(r) = M_c(\infty)\left[1\ -\ exp\left(-\frac{r^2}{\sigma_r^2}\right)\right] \quad , \tag{D10}$$

where,

$$M_c(\infty) = \pi\ \rho_0\ h\ \sigma_r^2 \quad . \tag{D11}$$

From the above expressions, we see that $y_{1/2} = \sigma_r\sqrt{ln\,2}$, $\bar{\rho} = \rho_0/(2\ ln\,2)$, $k_N = \sqrt{\pi\ ln\,2}$, $k_M = 2\pi$, yielding,

$$k_v = \left[\frac{\pi}{6}\,k_F\,\mu\,\mathrm{m_{H2}}\,\mathrm{G}\right]^{0.5} \quad , \tag{D12}$$

and adopting $k_F = 1$,

$$= 3.899 \times 10^{-16} cgs \quad .$$

The above results give the central sightline optical depth:

$$\tau_0 = 1.10 \times 10^2\,\bar{\mathrm{n}}^{0.5}\,\mathrm{T_K^{-1.75}} \quad , \tag{D13}$$

for $\mathrm{T_K} = 10$ to 20 K. These results along with the k_A and ϵ values given in Subsection 3.1.4 give

$$X_f(X_{20}) = 0.309\,C_T\,\mathrm{T_K^{-0.56}}\,\bar{\mathrm{n}}^{0.37} \quad . \tag{D14}$$

The numerical results of the above calculations are listed in Tables 1 through 5.

D.2. Viewed Along the Axis of Symmetry: The End-on Case

The mass density is again of the form $\rho = \rho(r)$, but with the sightline along the axis of symmetry. The x-y plane is still chosen to be perpendicular to the observer's sightline and z is measured along the sightline and along the cylinder's symmetry axis. The radius, r, is again the distance from the central axis, but this is now $x^2 + y^2$. The cylinder's length again

is h. The clump column density as a function of projected distance from the central axis, $N_c(r)$, is given by

$$N_c(r) = n_c(r)\ h \quad , \tag{D15}$$

which is because $n_c(r)$ has no z-dependence. The HWHM radius, $r_{1/2}$, is then found from

$$n_c(r_{1/2}) \equiv 0.5\ n_c(0) \quad . \tag{D16}$$

The expressions for $M_c(r)$, $k_M, \bar{\rho}$, and k_N are analogous to those for the side-on case — i.e., (D2), (D5), (D3), and (C5) — but with $r_{1/2}$ in place of $y_{1/2}$ or $p_{1/2}$. Combining this last with (D15) yields,

$$k_N = \frac{h}{d_{1/2}} \frac{n_c(0)}{\bar{\mathrm{n}}} \quad , \tag{D17}$$

where $d_{1/2} \equiv 2\, r_{1/2}$. The above states that $k_N \propto h/d_{1/2}$; i.e., k_N is proportional to the cylinder aspect ratio.

Other expressions are identical to those mentioned previously: k_v is still given by (D6), $\Delta \mathrm{v_c}$ by (C8), τ_0 by (C10), and X_f by (C11). The dependence of X_f on k_F is the same as in the side-on case. The dependence of X_f on k_N implies there is now a dependence on the cylinder aspect ratio: $X_f \propto (h/d_{1/2})^{(1-\epsilon)}$.

D.2.1. Gaussian Cylinder

The Gaussian cylinder has been treated in the side-on case, so there are similarities in this end-on case. The relationship between $r_{1/2}$ and σ_r is the same as that between $y_{1/2}$ and σ_r. The relationship between $\bar{\rho}$ and ρ_0 is unchanged. k_M and k_v are also unchanged. One important change is the expression for k_N:

$$k_N = 2(ln\, 2) \frac{h}{d_{1/2}} \quad . \tag{D18}$$

These results give τ_0:

$$\tau_0 = 1.04 \times 10^2\, \bar{\mathrm{n}}^{0.5}\, \mathrm{T_K^{-1.75}} \left(\frac{\mathrm{h}}{\mathrm{d_{1/2}}} \right) \quad , \tag{D19}$$

for $\mathrm{T_K} = 10$ to 20 K. Another difference is that the end-on Gaussian cylinder looks like the Gaussian sphere. Using the k_A and ϵ for the Gaussian sphere results in,

$$X_f(X_{20}) = 0.171\, C_T\, \mathrm{T_K^{-0.38}}\, \bar{\mathrm{n}}^{0.32} \left(\frac{h}{d_{1/2}} \right)^{0.64} \quad . \tag{D20}$$

The numerical results of the above calculations are listed in Tables 1 through 5.

D.3. Collapsing, Magnetized Filament

Tilley & Pudritz (2003) examined the case of a constant toroidal flux-to-mass ratio in a collapsing cylindrical cloud. Here we estimate X_f for the side-on case only. Their equation (35) can be rearranged to give the velocity width:

$$\Delta \mathrm{v_c} = 2.89 \times 10^{-16}\ n_0^{0.5}\ \lambda_{frag}\ k_{max}\ \ cgs \quad , \tag{D21}$$

where λ_{frag} is the fragmentation wavelength and k_{max} is a dimensionless wavenumber (see Tilley & Pudritz 2003). They find that the density goes like r^{-2} for a strong magnetic field and r^{-4} for a weak magnetic field. So, assuming a roughly constant density inside radius, r_0,

$$\rho(r) = \rho_0 \qquad for\ r \le r_0 \tag{D22}$$

$$= \rho_0 \left(\frac{r_0}{r}\right)^{\alpha} \qquad for\ r \ge r_0, \tag{D23}$$

where $\alpha = 2$ or 4. Combining equation (D1) with the number density analogs of (D22) and (D23),

$$N_c(y) = 2\ n_0 \sqrt{r_0^2 - y^2}\ +\ 2\ n_0\, r_0^{\alpha} \int\limits_{\sqrt{r_0^2-y^2}}^{\infty} dz \left(z^2 + y^2\right)^{-\alpha/2} \qquad for\ y \le r_0 \tag{D24}$$

$$= 2\ n_0\, r_0^{\alpha} \int\limits_{0}^{\infty} dz \left(z^2 + y^2\right)^{-\alpha/2} \qquad for\ y \ge r_0. \tag{D25}$$

Combining equation (D2) with (D24) and (D25) results in

$$M_c(r) = \pi\, h\, r_0^2\, \rho_0\ +\ 2\,\pi\, h\, \rho_0\, r_0^{\alpha} \int_{r_0}^{r} d\mathcal{R}\ \mathcal{R}^{(1-\alpha)} \quad . \tag{D26}$$

Now we will examine the $\alpha = 2$ and $\alpha = 4$ cases separately.

D.3.1. $\alpha = 2$

For $\alpha = 2$ the mass diverges when $r \to \infty$, so we must specify an outer radius, r_1. The upper limits in equations (D24) and (D25) are r_1 instead of ∞. But, for simplicity, we will assume that $r_1 \gg r_0$. Equations (D24) and (D25) become

$$N_c(y) = 2n_0 \sqrt{r_0^2 - y^2}\ +\ \frac{2\ n_0\, r_0^2}{y} \left[arccos\left(\frac{y}{r_1}\right) - arccos\left(\frac{y}{r_0}\right)\right]\ for\ y \le r_0 \tag{D27}$$

$$= \pi\ \ n_0\, r_0^2\, y^{-1}\, arccos\left(\frac{y}{r_1}\right) \qquad for\ r_0 \le y \le r_1. \tag{D28}$$

It is easy to show that $N_c(0) = 4\,n_0\,r_0$ and, accordingly, that $y_{1/2} = \frac{\pi}{2}\,r_0$, where it is assumed that $r_1 \gg y_{1/2}$. Equation (D26) becomes

$$M_c(r) = \pi\,h\,r_0^2\,\rho_0\ \left[1\ +\ 2\ ln\left(\frac{r}{r_0}\right)\right] \quad . \tag{D29}$$

The maximum radius, r_1, must be specified and the total mass, $M_c(r_1)$, is dependent on the ratio of the outer-to-inner radii of the r^{-2} region, r_1/r_0. Expression (D3) now gives us $\bar{\rho}$:

$$\begin{aligned} \bar{\rho} &= \left(\frac{2}{\pi}\right)^2\ \left[1\ +\ 2\ ln\left(\frac{\pi}{2}\right)\right]\ \rho_0 \quad , \\ &= 0.771\rho_0 \end{aligned} \tag{D30}$$

With this information in hand (and assuming r_0/r_1 to be small) it is easy to demonstrate that

$$\begin{aligned} k_N &= \frac{\pi}{1\ +\ 2\ ln\left(\frac{\pi}{2}\right)} \\ &= 1.651 \quad . \end{aligned} \tag{D31}$$

We can also determine k_M, but it is only useful for estimating $\Delta \mathrm{v_c}$ for virialized gas. Also, it is normally defined in terms of $M_c(\infty)$. Nevertheless, for completeness, it is given here for $M_c(r_1)$:

$$k_M = \pi\ \frac{1\ +\ 2\ ln\left(\frac{r_1}{r_0}\right)}{1\ +\ 2\ ln\left(\frac{\pi}{2}\right)} \tag{D32}$$

Expression (D21) is rewritten as

$$\Delta \mathrm{v_c} = k_v\ \bar{\mathrm{n}}^{0.5}\ \lambda_{frag}\ k_{max} \quad , \tag{D33}$$

where,

$$k_v = 3.294 \times 10^{-16}\ cgs$$

Starting with equation (21) and plugging in (D33) and $N_c(0)$ expressed in terms of k_N yields,

$$\tau_0 = \frac{k_\tau\,k_N}{k_v\,k_{max}\,\sqrt{2\pi}}\ \bar{\mathrm{n}}^{0.5}\,\mathrm{T_K}^{-\gamma}\ \left(\frac{\mathrm{d_{1/2}}}{\lambda_{\mathrm{frag}}}\right) \quad , \tag{D34}$$

where, again, $d_{1/2} = 2y_{1/2}$.

Now we can combine the expressions developed here with (25), (26), and (10) to obtain,

$$X_f = (2\pi)^{\frac{1}{2}(\epsilon-1)}\,C_T\,k_A^{-1}\,k_\tau^{-\epsilon}\,k_v^{\epsilon-1}\,k_N^{1-\epsilon}\,\mathrm{T_K}^{\gamma\epsilon-1}\,\bar{\mathrm{n}}^{\frac{1}{2}(1-\epsilon)}\ \left(\frac{d_{1/2}}{\lambda_{frag}\ k_{max}}\right)^{1-\epsilon} \quad . \tag{D35}$$

Except for the extra factor of $[d_{1/2}/(\lambda_{frag}\ k_{max})]^{1-\epsilon}$, this is identical to the more-or-less general expression for X_f, i.e., equation (C11). Evaluating (D35) numerically depends on the values of k_A and ϵ, which depend on r_1/r_0. Here we try two values for this ratio: $r_1/r_0 = 10$ and $r_1/r_0 = 1000$. For $r_1/r_0 = 10$, $k_A = 1.74$ and $\epsilon = 0.27$ and,

$$X_f(X_{20}) \ = \ 0.97\ C_T\ \mathrm{T_K^{-0.53}}\ \bar{\mathrm{n}}^{0.37}\ \left(\frac{d_{1/2}}{\lambda_{frag}}\right)^{0.74} \quad . \tag{D36}$$

For $r_1/r_0 = 1000$, $k_A = 1.46$, $\epsilon = 0.69$ and,

$$X_f(X_{20}) \ = \ 0.0729\ C_T\ \mathrm{T_K^{+0.21}}\ \bar{\mathrm{n}}^{0.16}\ \left(\frac{d_{1/2}}{\lambda_{frag}}\right)^{0.31} \quad , \tag{D37}$$

in which $k_{max} = 0.2$ was adopted for both cases (see Tilley & Pudritz 2003).

D.3.2. $\alpha = 4$

Equations (D24) and (D25) become

$$N_c(y) \ = \ 2\ n_0 \sqrt{r_0^2 - y^2}\ +\ ... \\ + \ n_0\, r_0^4\, y^{-3} \left[arcsin\left(\frac{y}{r_0}\right)\ -\ \left(\frac{y}{r_0}\right)\left(1\ -\ \frac{y^2}{r_0^2}\right)^{\frac{1}{2}} \right] \quad for\ y \le r_0 \tag{D38}$$

$$= \ \frac{\pi}{2}\ n_0\, r_0^4\, y^{-3} \quad for\ y \ge r_0. \tag{D39}$$

It is easy to show that $N_c(0) = \frac{8}{3}\, n_0\, r_0$ and, accordingly, that $y_{1/2} = (\frac{3\pi}{8})^{\frac{1}{3}}\, r_0$. Equation (D26) becomes

$$M_c(r) \ = \ M_c(\infty) \left(1\ -\ \frac{r^2}{2\, r_0^2}\right) \quad , \tag{D40}$$

where,

$$M_c(\infty) \ = \ 2\,\pi\ h\ r_0^2\ \rho_0 \quad . \tag{D41}$$

Unlike the $\alpha = 2$ case, the $\alpha = 4$ case has finite mass, even for $r/r_0 \to \infty$. Expression (D3) gives us $\bar{\rho}$:

$$\bar{\rho} \ = \ \left(\frac{8}{3\,\pi}\right)^{\frac{2}{3}} \left[1\ -\ \frac{1}{2}\ \left(\frac{8}{3\,\pi}\right)^{\frac{2}{3}}\right]\ \rho_0 \quad , \tag{D42}$$

$$= \ 0.495 \rho_0$$

It is now easy to demonstrate that

$$k_N = \frac{2\,\pi}{(3\,\pi)^{\frac{2}{3}} - 2} \tag{D43}$$

$$= 2.552$$

For completeness, k_M is also given:

$$k_M = \frac{2\,\pi}{1 - \frac{1}{2}\left(\frac{8}{3\,\pi}\right)^{\frac{2}{3}}} \tag{D44}$$

With k_N known, we have $\Delta \mathrm{v_c}$ given by (D33) and

$$k_v = 4.114 \times 10^{-16}\ cgs \quad . \tag{D45}$$

The equation for X_f is (D35). Numerically integrating (2) and (3) gives $k_A = 1.15$ and $\epsilon = 0.37$. Adopting $k_{max} = 0.2$ and substituting the values for k_A and ϵ into (D35) results in

$$X_f(X_{20}) = 0.900\ C_T\ \mathrm{T_K^{-0.36}}\ \bar{\mathrm{n}}^{0.32}\ \left(\frac{d_{1/2}}{\lambda_{frag}}\right)^{0.64} \quad . \tag{D46}$$

REFERENCES

Adler, D. S., Lo, K. Y., Wright, M. C. H., Rydbeck, G., Plante, R. L., and Allen, R. J. 1992, ApJ, 392, 497

Alloin, D., Barvainis, R., and Guilloteau, S. 2000, ApJ, 528, L81

Alves, J., Lada, C. J., Lada, E. A., Kenyon, S. J., Phelps, R. 1998, ApJ, 506, 292

Ballesteros-Paredes, J. and Mac Low, M.-M. 2002 ApJ, 570, 734

Bally, J., Langer, W. D., Stark, A. A., and Wilson, R. W. 1987, ApJ, 312, L45

Bally, J., Stark, A. A., Wilson, R. W., and Henkel, C. 1987, ApJS, 65, 13

Bally, J., Stark, A. A., Wilson, R. W., and Henkel, C. 1988, ApJ, 324, 223

Barvainis, R., Maloney, P. R., Antonucci, R., and Alloin, D. 1997, ApJ, 484, 695

Barvainis, R., Alloin, D., Guilloteau, S., and Antonucci, R. 1998, ApJ, 492, L13

Bertoldi, F. and McKee, C. F. 1992, ApJ, 395, 140

Borkowski, K. J., Hendrick, S. P., Reynolds, S. P. 2006, AJ, 652, 1259

Boselli, A., Lequeux, J., and Gavazzi, G. 2002, A&A, 384, 33

Brouillet, N., Kaufman, M., Combes, F., Baudry, A. and Bash, F. 1998, A&A, 333, 92

Brown, R. L. and Vanden Bout, P. A. 1992, ApJ, 397, L19

Carilli, C. L., Cox, P., Bertoldi, F., Menten, K. M., Omont, A., Djorkovski, S. G., Petric, A., Beelen, A., Isaak, K. G., and McMahon, R. G. 2002, ApJ, 575, 145

Carilli, C. L., Kohno, K., Kawabe, R., Ohta, K., Henkel, C., Menten, K., Yun, M. S., Petric, A., and Tutui, Y. 2002, AJ, 123, 1838

Carpenter, J. M., Snell, R. L., and Schloerb, F. P. 1990, ApJ, 362, 147

Clark, P. C. and Bonnell, I. A. 2004, MNRAS, 347, L36

COBE Diffuse Infrared Background Experiment (*DIRBE*) Explanatory Supplement 1998, version 2.3, ed. M. G. Hauser, T. Kelsall, D. Leisawitz, and J. Weiland, *COBE* Ref. Pub. 98-A (Greenbelt, MD: NASA/GSFC), available in electronic form from the NSSDC.

Dame, T. M., Hartmann, D., and Thaddeus, P. 2001, ApJ, 547, 792

Dahmen, G., Hüttemeister, S., Wilson, T. L., Mauersberger, R., Linhart, A., Bronfman, L., Tieftrunk, A. R., Meyer, K., Wiedenhöver, W., Dame, T. M., Palmer, E. S., May, J., Aparici, J., and Mac-Auliffe, F. 1997, A&AS, 126, 197

Dahmen, G., Hüttemeister, S., Wilson, T. L., and Mauersberger, R. 1998, A&A331, 959.

Dettmar, R.-J. and Heithausen, A. 1989, ApJ, 344, L61

Dickman, R. L., Snell, R. L., and Schloerb, F. P. 1986, ApJ, 309, 326 (DSS86)

Evans, N. J. 1980, IAU Symp. 87, Interstellar Molecules, (Dordrect: D. Reidel), p 1.

Evans, N. J. 1999, ARA&A, 37, 311

Fiege, J. D. and Pudritz, R. E. 2000, MNRAS, 311, 85

Fukui, Y., Mizuno, N., Yamaguchi, R., Mizuno, A., Onishi, T., Ogawa, H., Yonekura, Y., Kawamura, A., Tachihara, K., Xiao, K., Yamaguchi, N., Hara, A., Hayakawa, T., Kato, S., Abe, R., Saito, H., Mano, S., Matsunaga, K., Mine, Y., Moriguchi, Y., Aoyama, H., Asayama, S., Yoshikawa, N., and Rubio, M. 1999, PASJ, 51, 745

Frerking, M. A., Langer, W. D., and Wilson, R. W. 1982, ApJ, 262, 590

Garg, A. et al. 2007, ApJ, 133, 419

Guélin, M., Zylka, R., Mezger, P. G., Haslam, C. G. T., and Kreysa, E. 1995, A&A, 298, L29

Güsten, R., Walmsley, C. M., Ungerechts, H., and Churchwell, E. 1985, A&A, 142, 381

Hamuy, M., Phillips, M. M., Suntzef, N. B., Schommer, R. A., Maza, J., and Aviles, R. 1996, AJ, 112, 2391

Hamuy, M., Phillips, M. M., Suntzef, N. B., Schommer, R. A., Maza, J., Smith, R. C., Lira, P., and Aviles, R. 1996, AJ, 112, 2438

Harris, A. I., Jaffe, D. T., Silber, M., and Genzel, R. 1985, ApJ, 294, L93

Harvey, D. W. A., Wilner, D. J., Lada, C. J., Myers, P. C., Alves, J. F., and Chen, H. ApJ, 563, 903

Helfer, T. T. and Blitz, L. 1997, ApJ, 478, 233

Henriksen, R., André, P., and Bontemps, S. 1997, A&A, 323, 549

Heyer, M. H., Carpenter, J. M., and Ladd, E. F. 1996, ApJ, 463, 630

Heyer, M. H., Carpenter, J. M., and Snell, R. L. 2001, ApJ, 551, 852

Howell, D. A. et al. 2006, Nature, 443, 308

1997, IAU Symp. 170, CO: Twenty-five Years of Millimeter-Wave Spectroscopy, eds. W. B. Latter, S. J. E. Radford, P. R. Jewell, J. G. Mangum & J. Bally (Dordrecht: Kluwer)

Hüttemeister, S., Dahmen, G., Mauersberger, R., Henkel, C., Wilson, T. L., and Martín-Pintado, J. 1998, A&A, 334, 646

Hüttemeister, S., Wilson, T. L., Bania, T. M., and Martín-Pintado, J. 1993, A&A, 280, 255

Israel, F. P. 1988, Millimetre and Submillimetre Astronomy, Summer School, Stirling, Scotland, (Dordrecht: Kluwer), p. 281

Israel, F. P. 1997, A&A, 317, 65

Israel, F. P. 1997, A&A, 328, 471

Israel, F. P. 2000, Molecular Hydrogen in Space, eds. F. Combes and G. Pineau des Forets, Cambridge University Press, p. 293-296

James, J. B., Davis, T. M., Schmidt, B. P., and Kim, A. G. 2006, MNRAS, 370, 933

Kawamura, A., Onishi, T., Yonekura, Y., Dobashi, K., Mizuno, A., Ogawa, H., and Fukui, Y. 1998, ApJS, 117, 387

Kutner, M. L. 1984, Fundamentals of Cosmic Physics, 9, 233

Kutner, M. L. and Leung, C. M. 1985, ApJ, 291, 188

Lada, C. J., Alves, J., and Lada, E. A. 1999, ApJ, 512, 250

Langer, W. D. and Penzias, A. A. 1990, ApJ357, 477

Loinard, L. and Allen, R. J. 1998, ApJ, 499, 227

Maddalena, R. J., Morris, M., Moscowitz, J., and Thaddeus, P. 1986, ApJ, 303, 375

Madden, S. C., Poglitsch, A., Geis, N., Stacey, G. J., and Townes, C. H. 1997, ApJ, 483, 200

Magnani, L., Onello, J. S., Adams, N. G., Hartmann, D., and Thaddeus, P. 1998, ApJ, 504, 209

Maloney, P. R. 1990, ApJ, 462, 215

Maloney, P. R. and Black, J. H. 1988, ApJ, 325, 389

Martin, C. L., Walsh, W. M., Xiao, K., Lane, A. P., Walker, C. K., and Stark, A. A. 2004, ApJS, 150, 239

Martin, H. M., Sanders, D. B., and Hill, R. E. 1984, MNRAS, 208, 35 (MSH84)

Meier, D. S., and Turner, J. L. 2001, ApJ, 551, 687

Meier, D. S., Turner, J. L., and Hurt, R. L. 2000, ApJ, 513, 200

Nagahama, T., Mizuno, A., Ogawa, H., and Fukui, Y. 1998, AJ, 116, 336

Nakai, N. and Kuno, N. 1995, PASJ, 47, 761

Neill, J. D. et al. 2006, AJ, 132, 1126

Oka, T., Hasegawa, T., Hayashi, M., Handa, T., and Sakamoto, S. 1998, ApJ, 493, 730

Onishi, T., Mizuno, A., Kawamura, A., Ogawa, H., and Fukui, Y. 1996, ApJ, 465, 815

Ostriker, J. 1964, ApJ, 140, 1056

Ostriker, E. C., Gamme, C. F., and Stone, J. M. 1999, ApJ, 513, 259

Ostriker, E. C., Stone, J. M., and Gammie, C. F. 2001, ApJ, 546, 980

Paglione, T. A. D., Jackson, J. M., Bolatto, A. D., and Heyer, M. H. 1998, ApJ, 493, 680

Paglione, T. A. D., Wall, W. F., Young, J. S., Heyer, M. H., Richard, M., Goldstein, M., Kaufman, Z., Nantais, J., and Perry, G. 2001, ApJS, 135, 183

Perlmutter, S. et al. 1999, ApJ, 517, 565

Phillips, M. M. 1993, ApJ, 413, L105

Pichardo, B., Vázquez-Semadeni, E., Gazol, A., Passot, T., Ballesteros-Paredes, J. 2000, ApJ, 532, 353

Plume, R., Bensch, F., Howe, J. E., Ashby, M. L. N., Bergin, E. A., Chin, G., Erickson, E. R., Goldsmith, P. F., Harwit, M., Kleiner, S., Koch, D. G., Neufeld, D. A., Patten, B. M., Scheider, R., Snell, R. L., Stauffer, J. R., Tolls, V., Wang, Z., Winnewisser, G., Zhang, Y. F., Reynolds, K., Joyce, R., Tavoletti, C., Jack, G., Rodkey, C. J., and Melnick, G. J. 2000, ApJ, 539, L133

Pringle, J. E., Allen, R. J., and Lubow, S. H. 2001, MNRAS, 327, 663

Rand, R. J., Lord, S. D., and Higdon, J. L. 1999, ApJ, 513, 720

Regan, M. W. 2000, ApJ, 541, 142

Reiss, A. G., Press, W. H., and Kirschner, R. P. 1995, ApJ, 438, L17

Reiss, A. G., Press, W. H., and Kirschner, R. P. 1996, ApJ, 473, 88

Reiss, A. G., 1998, AJ, 116, 1009

Reiss, A. G. and Livio, M. 2006, ApJ, 648, 884

Rickard, L. J. and Blitz, L. 1985, ApJ, 292, L57

Rodríguez-Fernández, N. J., Martín-Pintado, J., Fuente, A., de Vicente, P., Wilson, T. L., and Hüttemeister, S. 2001, A&A, 365, 174

Rosolowski, E., Engargiola, G., Plambeck, R., Blitz, L. 2003, ApJ, 599, 258

Sakamoto, S. 1996, ApJ, 462, 215

Sakamoto, S., Hayashi, M., Hasegawa, T., Handa, T., and Oka, T. 1994, ApJ, 425, 641

Sanders, D. B., Scoville, N. Z., and Solomon, P. M. 1985, ApJ, 289, 373

Sauer, D. N., Hoffman, T. L., and Pauldrach, A. W. A. 2006, A&A, 459, 229

Shu, F. H. 1991, *Radiation* (Mill Valley: University Science Books)

Simon, R. S., Jackson, J. M., Clemens, D. P., Bania, T. M., and Heyer, M. H. 2001, ApJ, 551, 747

Sodroski, T. J., Bennett, C., Boggess, N., Dwek, E., Franz, B. A., Hauser, M. G., Kelsall, T., Moseley, S. H., Odegard, N., Silverberg, R. F., and Weiland, J. L. 1994, ApJ, 428, 638

Sodroski, T. J., Odegard, N., Dwek, E., Hauser, M. G., Franz, B. A., Freedman, I., Kelsall, T., Wall, W. F., Berriman, G. B., Odenwald, S. F., Bennett, C., Reach, W. T., and Weiland, J. L. 1995, ApJ, 452, 262

Sofue, Y. and Yoshida, S. 1993, ApJ, 417, L63

Stark, A. A., Bally, J., Wilson, R. W., and Pound, M. W. 1989, in IAU Symp. 136: The Center of the Galaxy, ed. M. Morris (Dordrecht: Kluwer), 129

Strong, A. W., Bloemen, J. B. G. M., Dame, T. M., Grenier, I. A., Hermsen, W., Lebrun, F., Nyman, L.-Å., Pollock, A. M. T., and Thaddeus, P. 1988, A&A, 207, 1

Strong, A. W., Moskalenko, I. V., Reimer, O., Digel, S., and Diehl, R. 2004, A&A, 422, L47

Tachihara, K., Mizuno, A., and Fukui, Y. 2000, ApJ, 528, 817

Tilley, D. A. and Pudritz, R. E. 2003, ApJ, 593, 426

Vázquez-Semadeni, E., Gómez, C. C., Jappsen, A. K., Ballasteros-Paredes, J., Gonzalez, R. F., and Klessen, R. S. 2007, ApJ, 657, XXX

Wall, W. F., Reach, W. T., Hauser, M. G., Arendt, R. G., Weiland, J. L., Berriman, G. B., Bennett, C. L., Dwek, E., Leisawitz, D., Mitra, P. M., Odenwald, S. F., Sodroski, T. J., and Toller, G. N. 1996, ApJ, 456, 566

Wall, W. F. 2006, astro-ph/0601529

Wall, W. F. 2006a, astro-ph/0601548

Wall, W. F. 2006b, astro-ph/0601549

Wall, W. F. 2006c, RMAA, 42, 117

Wall, W. F., Jaffe, D. T., Bash, F. N., Israel, F. P., Maloney, P. R., and Baas, F. 1993, ApJ, 414, 98

Wang, Y. 2007, ApJ, 654, L123

Warin, S., Benayoun, J. J., and Viala, Y. P. 1996, A&A, 308, 535

Weiss, A., Neininger, N., Hüttemeister, S., and Klein, U. 2001, A&A, 365, 571

Williams, J. P., Blitz, L., and Stark, A. A. 1995, ApJ, 451, 252

Williams, J. P., de Geus, E. J., and Blitz, L. 1994, ApJ, 428, 693

Yao L., Seaquist, E. R., Kuno, K., and Dunne, L. 2003, ApJ, 588, 771

Young, J. S. and Scoville, N. Z. 1982, ApJ, 258, 467

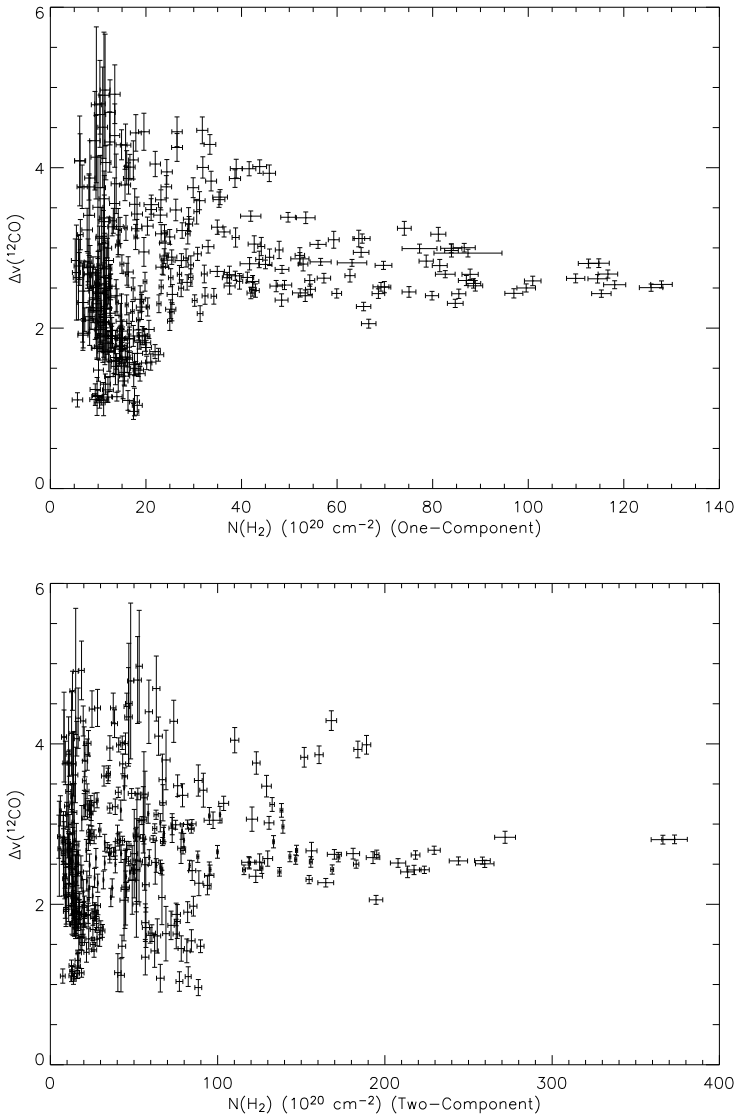

Fig. 1.— The panels above show the velocity widths, $\Delta v(^{12}\mathrm{CO})$, of the ^{12}CO J = 1 → 0 line for the Orion A and B molecular clouds versus the molecular hydrogen column densities, $N(H_2)$. The velocity widths are effective velocity widths given by the ratio of the velocity-integrated radiation temperature, I(CO), divided by the peak radiation temperature of the line. The $N(H_2)$ values for the upper panel are those determined from the one-component, non-LTE models of Wall (2006). The $N(H_2)$ values for the lower panel are the two-component, two-subsample, non-LTE models of Wall (2006). The sample of points are those for which the intensities are 5-σ or more for the 140 μm and 240 μm continuum, the ^{12}CO J = 1 → 0 line, and ^{13}CO J = 1 → 0 line. All these maps were convolved to 1-degree resolution (see Wall 2006, for details).

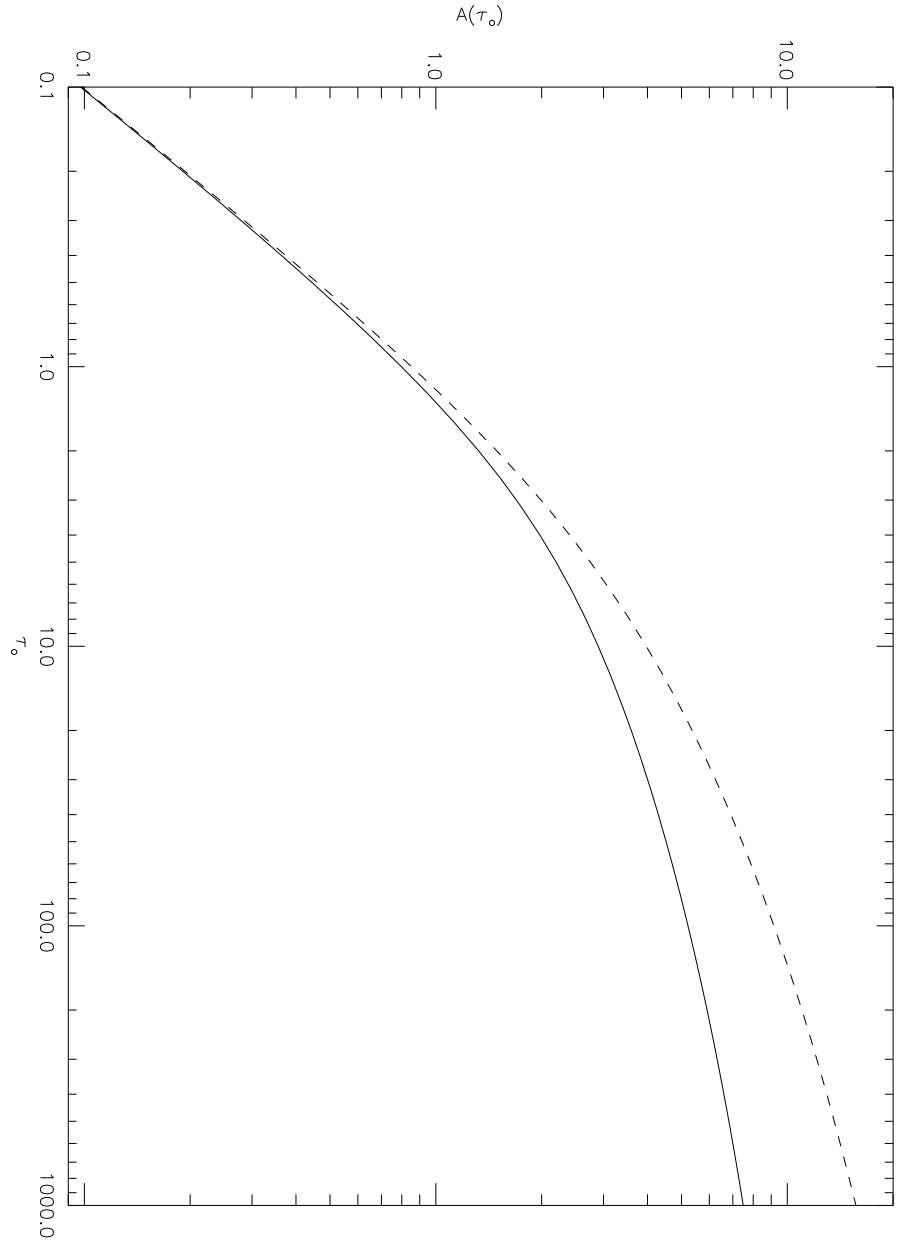

Fig. 2.— The effective optical depth of a clump, $A(\tau_0)$, after averaging over its projected area is plotted against the optical depth through the clump center, τ_0. The solid curve shows $A(\tau_0)$ versus τ_0 for a cylindrical clump viewed perpendicularly to the symmetry axis. The optical depth profile across the cylinder, from the central axis towards the edges, is Gaussian. The dashed curve shows the corresponding curve for a spherical clump. The optical depth profile from the sphere center towards the edges is also Gaussian. The Gaussian spherical clump case was also treated and plotted in MSH84.

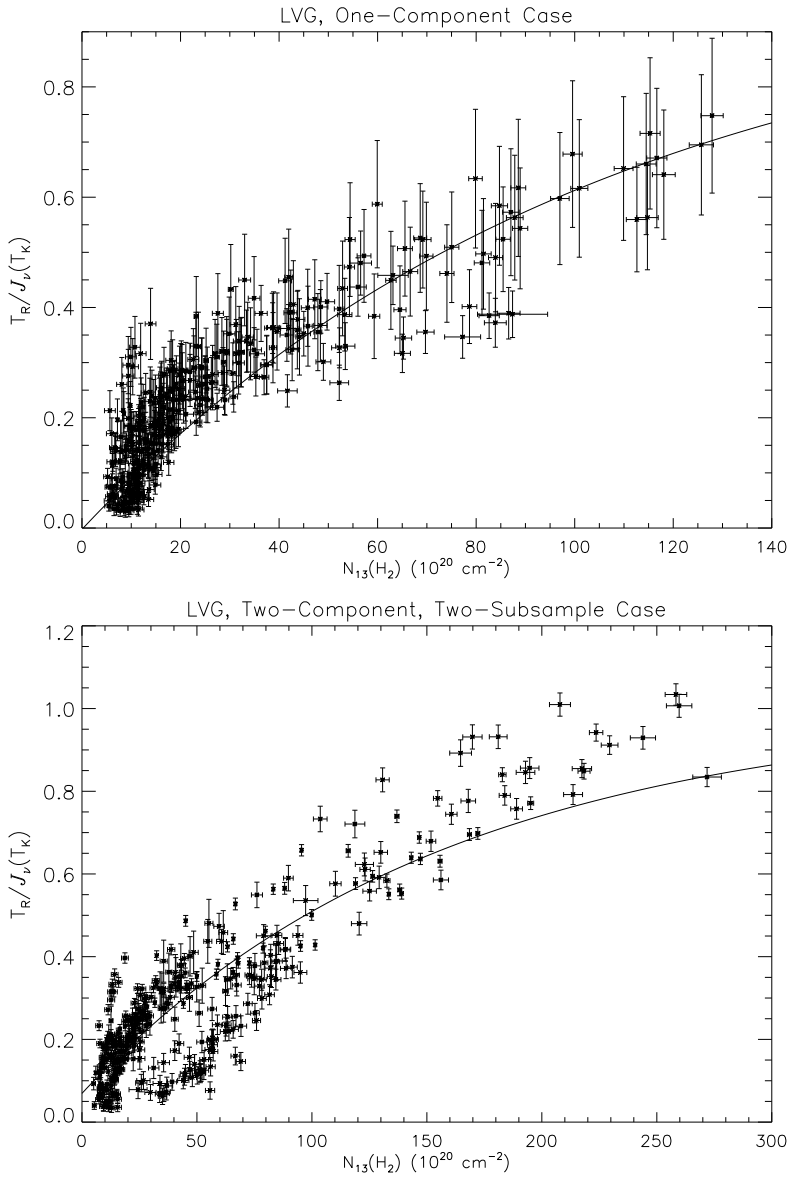

Fig. 3.— Plots of the CO J = 1 → 0 line radiation temperature, T_R, normalized to its source function, $\mathcal{J}_\nu(T_K)$, versus the ^{13}CO J = 1 → 0 derived H_2 column density. Both plots are reproduced from Wall (2006). The curves are of the form $y = 1 - exp(-a\,x - b)$, where, in the ideal case, $b = 0$. The upper plot is for the LVG, one-component models of Wall (2006) and the lower plot is for the LVG, two-component, two-subsample models of that paper. (The source function for the two-component models is the effective source function as defined in Wall (2006).) Given that x is in units of $10^{20}\,H_2\,\mathrm{cm}^{-2}$, $a = (9.5 \pm 0.4) \times 10^{-3}$ and $b = (2.4 \pm 5.5) \times 10^{-3}$ for the upper plot and $a = (6.4 \pm 0.2) \times 10^{-3}$ and $b = (7.2 \pm 0.8) \times 10^{-2}$ for the lower plot.

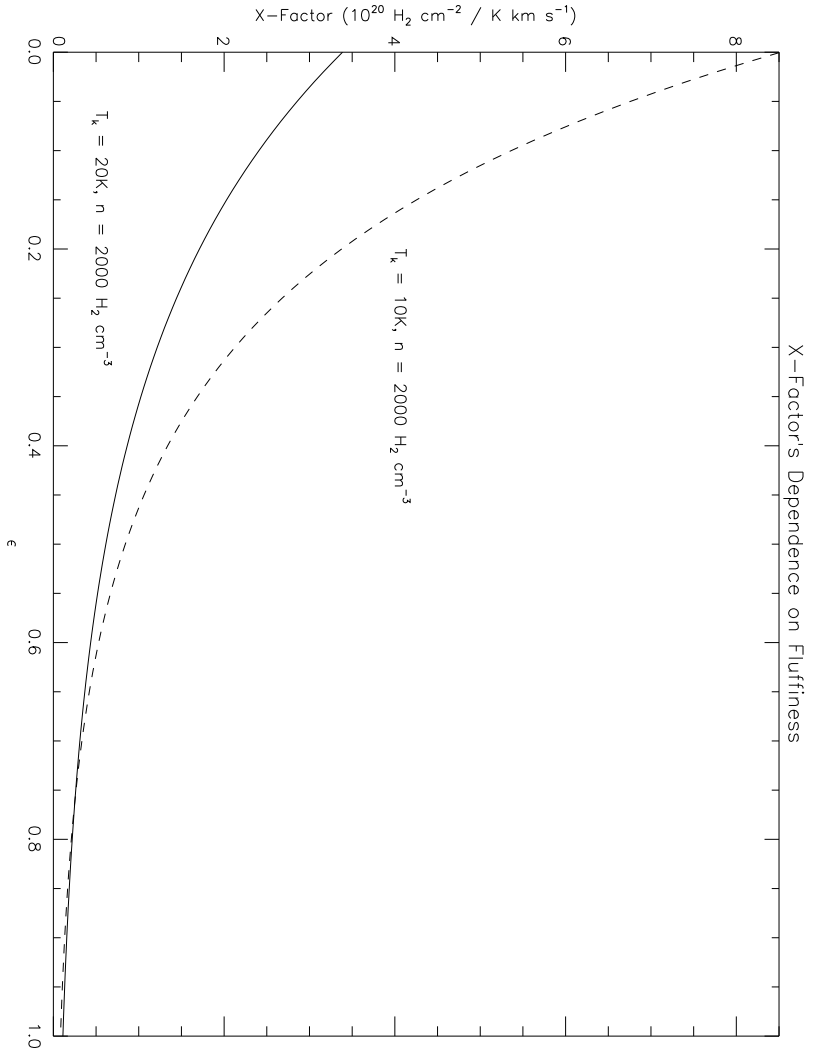

Fig. 4.— Curves that crudely represent the X-factor's dependence on the fluffiness parameter, ϵ, are depicted. The kinetic temperature, T_K, and the average densities, represented simply by n, corresponding to the curves are shown. Note that the values of the X-factor for $\epsilon = 0$ and 1 are too low by about 30%. See Section 3.2.1 for details. It must be emphasized that these curves are dependent on how the "average" density is defined (see Section 4.7.1).

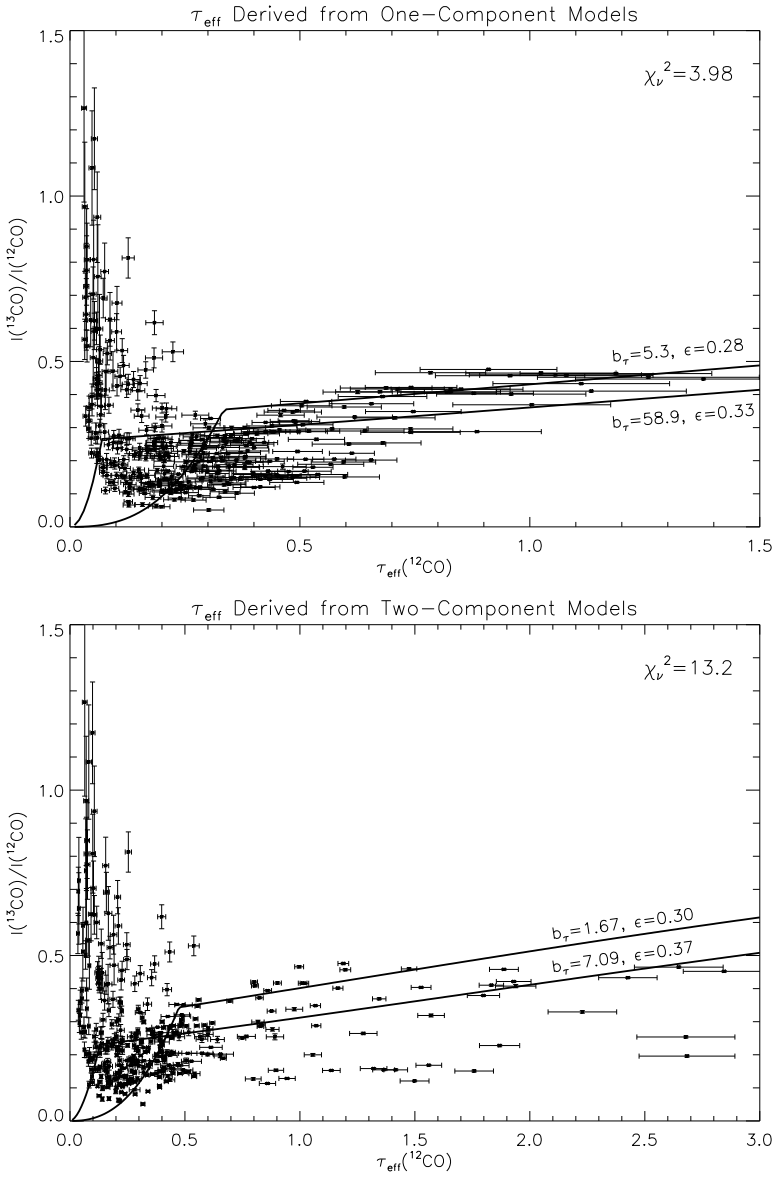

Fig. 5.— The ^{13}CO J = 1 → 0/^{12}CO J = 1 → 0 line ratio is plotted against the τ_{ef} of ^{12}CO J = 1 → 0. The points represent positions in the Orion A and B molecular clouds where the peak $T_R(^{12}\mathrm{CO\ J} = 1 \rightarrow 0) > 3\,\sigma$, and $I_\nu(140\,\mu\mathrm{m})$, $I_\nu(240\,\mu\mathrm{m})$, and $I(^{13}\mathrm{CO})$ are all $> 5\,\sigma$ (see Wall 2006). The solid curves represent model fits that are described in Section 3.3. The reduced chi-square of these two-curve fits are given in the upper-right corner of each panel. The error bars are $0.5\,\sigma$ for a better view of the distribution of points and of the model curves. The upper panel has the τ_{ef} values derived from one-component models and the lower panel has the τ_{ef} derived from two-component models (Wall 2006).

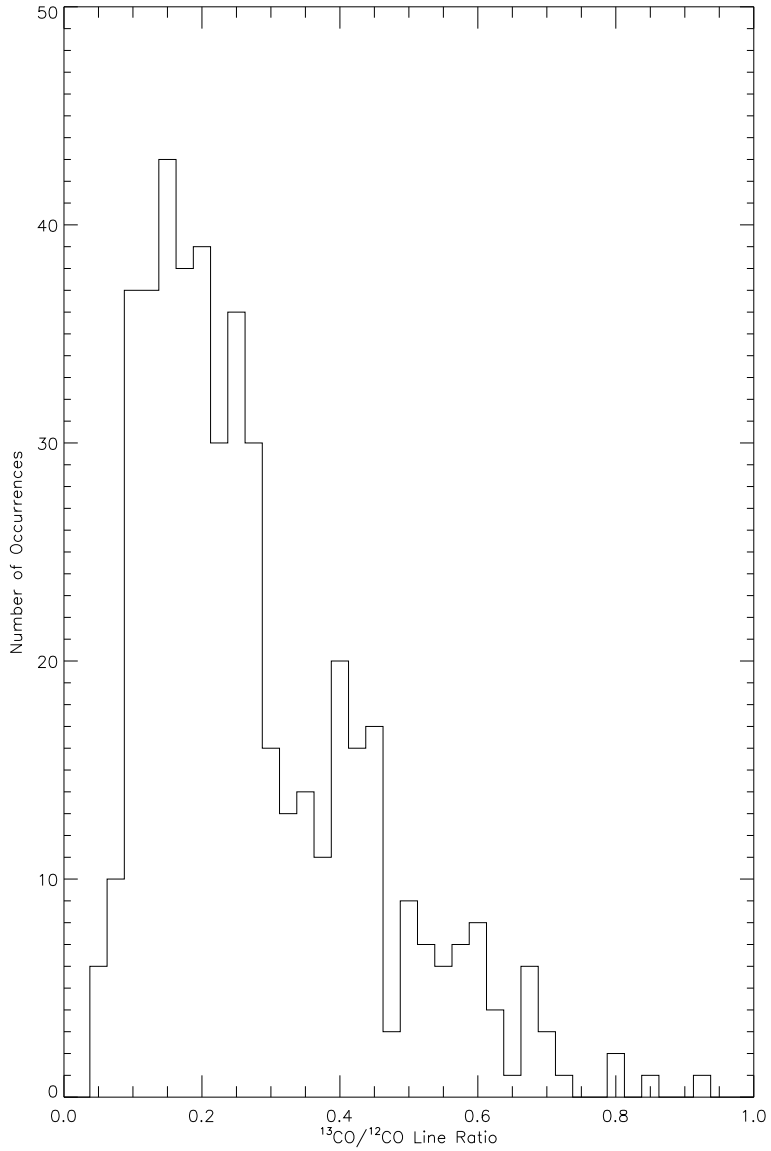

Fig. 6.— The frequencies of values of the ^{13}CO J = 1 → 0/^{12}CO J = 1 → 0 line ratio in the Orion clouds is plotted here as a histogram (solid line). This histogram only includes data where ^{12}CO and ^{13}CO observed line strengths are at or above 5-σ.

Table 1. X-Factor Values for Different Model Clump Types

Type of Clump[a]	k_A	ϵ	X_f ($10^{20} H_2 \cdot \mathrm{cm}^{-2}/\mathrm{K} \cdot \mathrm{km} \cdot \mathrm{s}^{-1}$)					
			$\mathrm{T_K} = 10\,\mathrm{K}$			$\mathrm{T_K} = 20\,\mathrm{K}$		
			$\bar{\mathrm{n}}$[b]$= 2 \times 10^2$	2×10^3	2×10^4	$\bar{\mathrm{n}}$[b]$= 2 \times 10^2$	2×10^3	2×10^4
$\tau \gg 1$[c]	1	0	3.5	11	35	1.4	4.4	14
$\tau \ll 1$	1	1	0.12	0.12	0.12	0.16	0.16	0.16
Hard S.	1.7	0.14	1.3	3.4	9.1	0.59	1.6	4.3
Gaussian S.	1.6	0.36	0.70	1.5	3.1	0.44	0.91	1.9
Sq. Lor. S.	1.5	0.57	0.36	0.58	0.95	0.28	0.47	0.76
G. F. (side-on)	1.5	0.25	0.93	2.2	5.2	0.51	1.2	2.8
G. F. (end-on)[d]	1.6	0.36	1.3	2.8	5.8	0.82	1.7	3.6

[a]These are the types of model clumps as described in Section 3: Completely Optically Thick, Optically Thin, Hard Sphere, Gaussian Sphere, Squared Lorentzian Sphere, Gaussian Filament (side-on and end-on).

[b]Clump average density as defined in Section 3 and in the appendices in units of H_2 *molecules* $\cdot$ cm^{-3}.

[c]For simplicity, a spherical geometry is adopted for computing X_f.

[d]Assuming a length-to-diameter ratio of 3.4.

Table 2. Full-Width-at-Half-Maximum Velocity Widths of Individual Model Clumps

Type of Clump[a]	Δv_c (FWHM)[b] ($km \cdot s^{-1}$)		
	$\bar{n}$[c] $= 2 \times 10^2$	2×10^3	2×10^4
Hard S.[d]	0.46	1.4	4.6
Gaussian S.[d]	0.63	2.0	6.3
Sq. Lor. S.[d]	0.64	2.0	6.4
G. Filament[e]	0.72	2.3	7.2

[a]These are some types of model clumps as described in Section 3: Hard Sphere, Gaussian Sphere, Squared Lorentzian Sphere, Gaussian Filament.

[b]The earlier computed values have been multiplied by $\sqrt{8\,ln2}$ to convert from rms to $FWHM$.

[c]Clump average density as defined in Section 3 and in the appendices in units of $H_2\ molecules \cdot cm^{-3}$.

[d]FWHM diameter of 1.8 pc was adopted.

[e]Length of 6.2 pc and FWHM diameter of 1.8 pc were adopted.

Table 3. Central Sightline Optical Depths, τ_0, of Individual Model Clumps

Type of Clump[a]	τ_0					
	$T_K = 10\,K$			$T_K = 20\,K$		
	$\bar{n}$[b]$= 2 \times 10^2$	2×10^3	2×10^4	$\bar{n}$[b]$= 2 \times 10^2$	2×10^3	2×10^4
Hard S.	30	94	300	8.8	28	88
Gaussian S.	34	109	344	10	32	100
Sq. Lor. S.	37	120	370	11	35	110
G. F. (side-on)	28	88	280	8.2	26	82
G. F. (end-on)[c]	90	280	900	27	84	270

[a]These are some types of model clumps as described in Section 3: Hard Sphere, Gaussian Sphere, Squared Lorentzian Sphere, Gaussian Filament (side-on and end-on).

[b]Clump average density as defined in Section 3 and in the appendices in units of $H_2\ molecules \cdot \mathrm{cm}^{-3}$.

[c]Assuming a length-to-diameter ratio of 3.4.

Table 4. Effective Optical Depths, $A(\tau_0)$, of Individual Model Clumps

Type of Clump[a]	k_A	ϵ	$A(\tau_0)$					
			$T_K = 10\,K$			$T_K = 20\,K$		
			$\bar{n}$[b]$= 2 \times 10^2$	2×10^3	2×10^4	$\bar{n}$[b]$= 2 \times 10^2$	2×10^3	2×10^4
Hard S.	1.7	0.14	2.7	3.2	3.8	2.3	2.7	3.2
Gaussian S.	1.6	0.36	5.7	8.6	13	3.7	5.6	8.4
Sq. Lor. S.	1.5	0.57	12	23	44	6.0	12	22
G. F. (side-on)	1.5	0.25	3.4	4.6	6.1	2.5	3.4	4.5
G. F. (end-on)[c]	1.6	0.36	8.0	12	18	5.2	7.9	12

[a]These are some types of model clumps as described in Section 3: Hard Sphere, Gaussian Sphere, Squared Lorentzian Sphere, Gaussian Filament (side-on and end-on).

[b]Clump average density as defined in Section 3 and in the appendices in units of H_2 *molecules* $\cdot$ cm^{-3}.

[c]Assuming a length-to-diameter ratio of 3.4.

Table 5. Masses, M_c, of Individual Model Clumps

Type of Clump[a]	M_c ($M_\odot$)		
	$\bar{n}$[b]$= 2 \times 10^2$	2×10^3	2×10^4
Hard S.[c]	3.9×10^1	3.9×10^2	3.9×10^3
Gaussian S.[c]	1.4×10^2	1.4×10^3	1.4×10^4
Sq. Lor. S.[c]	2.5×10^2	2.5×10^3	2.5×10^4
G. Filament[d]	4.1×10^2	4.1×10^3	4.1×10^4

[a]These are some types of model clumps as described in Section 3: Hard Sphere, Gaussian Sphere, Squared Lorentzian Sphere, Gaussian Filament.

[b]Clump average density as defined in Section 3 and in the appendices in units of $H_2\ molecules \cdot \mathrm{cm}^{-3}$.

[c]FWHM diameter of 1.8 pc was adopted.

[d]Length of 6.2 pc and FWHM diameter of 1.8 pc were adopted.